UNIVERSITY OF CALIFORNIA SAN DIEGO

Micromagnetic Modeling and Analysis of Magnetic Tunnel Junctions for Spintronics Applications

A dissertation submitted in partial satisfaction of the requirements

for the degree

Doctor of Philosophy

in

Materials Science and Engineering

by

Iana Volvach

Committee in charge:

Professor Vitaliy Lomakin, Chair
Professor Prabhakar R. Bandaru
Professor Eric E. Fullerton
Professor Zhawei Liu
Professor Vlado A. Lubarda

2021

Copyright
Iana Volvach, 2021
All rights reserved.

The Dissertation of Iana Volvach is approved, and it is acceptable in quality and form for publication on microfilm and electronically.

University of California San Diego

2021

DEDICATION

To my family and friends.

EPIGRAPH

A method is more important than a discovery since the right method will lead to new and even more important discoveries.

Lev Landau

TABLE OF CONTENTS

Dissertation Approval Page iii

Dedication iv

Epigraph v

Table of Contents vi

List of Figures viii

Acknowledgements xi

Vita xiv

Abstract of the Dissertation xvii

Part I Introduction 1

Chapter 1 Introduction 2

Chapter 2 Basic concepts of micromagnetism 6
- 2.1 Micromagnetic model representation 7
- 2.2 Landau-Lifshitz-Gilbert equation 8
- 2.3 Landau-Lifshitz-Gilbert-Slonczewski equation 10
- 2.4 Main interations in micromagnetism 11
  - 2.4.1 Effective magnetic field 11
  - 2.4.2 Zeeman interaction 12
  - 2.4.3 Magnetostatic interaction 13
  - 2.4.4 Magnetocrystalline anisotropy 19
  - 2.4.5 Exchange interaction 21
  - 2.4.6 Spin-transfer torque and interaction with spin current 24
- 2.5 Nudged Elastic Band method for thermal stability calculation 26
- 2.6 Thermal effects and the stochastic Landau-Lifshits-Gilbert equation 28

Chapter 3 Spin-tranfer torque driven devices 32
- 3.1 Magnetic memory 33
- 3.2 Spintronic devices 34
- 3.3 Magnetoresistance phenomena 35
  - 3.3.1 Giant magnetoresistance 35
  - 3.3.2 Tunnel magnetoresistance 37
  - 3.3.3 Magnetic nanopillar switching 39
- 3.4 Magnetic tunnel junction 41
  - 3.4.1 In-plane and perpendicular free layer orientation 42

3.4.2 Thermal stability factor of in-plane and perpendicular MTJs 44
3.4.3 Critical switching current and efficiency 46
3.5 Magnetic tunnel junction-based spintronic devices 51
3.5.1 Spin-transfer torque MRAM 52
3.5.2 Spin-orbit torque MRAM 53
3.6 Spin-transfer-torque oscillators (STOs) 55
3.6.1 Operation principle and device configuration 56
3.6.2 STO with perpendicular polarizer 58
3.6.3 STO based on antiferromagnets 64

Part II Micromagnetic modeling and analysis **68**

Chapter 4 Micromagnetic modeling of magnetic tunnel junctions 69
4.1 Micromagnetic modeling of spin-transfer torque 70
4.1.1 All-metallic spin-valve 70
4.1.2 Magnetic tunnel junction 73
4.2 Perpendicular magnetic tunnel junction 74
4.2.1 Minimal energy path and thermal stability 76
4.2.2 Current-induced magnetization switching and efficiency 80

Chapter 5 Perpendicular magnetic tunnel junction with composite free layer 87
5.1 Operation of the exchange-coupled-composite free layer (ECC FL) 88
5.2 Characterization of p-MTJ with ECC FL 90
5.2.1 Thermal stability 92
5.2.2 Current-induced switching properties 94
5.3 Advantages of using of p-MTJ with ECC FL 95

Chapter 6 Perpendicular magnetic tunnel junction with defects and properties distribution 97
6.1 p-MTJ with edge roughness 98
6.2 p-MTJ with surface roughness 101
6.3 Granular free layer in p-MTJ 102
6.3.1 Granular free layer at zero temperature 103
6.3.2 Granular free layer at room temperature 105

Chapter 7 Magnetic spin-torque oscillator 110
7.1 Antiferromagnetically coupled composite STO 110
7.2 Theoretical model of AF-ECC STO 113
7.3 Study of AF-ECC STO operation 115
7.3.1 Operation at zero temperature 116
7.3.2 Operation at room temperature 123

Chapter 8 Conclusion 128

Bibliography 130

LIST OF FIGURES

Figure 2.1: Micromagnetic model representation with tetrahedral discretization for different geometry types. 7

Figure 2.2: Illustration of the magnetization precession 9

Figure 2.3: Illustration of the Landau-Lifshitz-Gilbert-Slonczewski equation 11

Figure 2.4: Magnetic field calculation approximations 13

Figure 2.5: Illustration of the dipolar coupling between magnetic nanoislands 14

Figure 2.6: Examples of the effects of the magnetostatic interaction 15

Figure 2.7: Demagnetization factor as a function of aspect ratio for right circular cylinder for the averaged magnetic field along the cylinder axis 17

Figure 2.8: Illustration of the magnetic moment's orientation 22

Figure 2.9: Illustration of spin-transfer torque 25

Figure 2.10: Minimal energy path for a single magnetic layer 28

Figure 2.11: Illustration of the behavior of the magnetic moments above and under the Curie temperature 29

Figure 3.1: Illustration of the first magnetic memory 33

Figure 3.2: Schematic illustration of a magnetic pillar in a high resistance anti-parallel state and low resistance parallel state 34

Figure 3.3: Illustration of giant magnetoresistance effect in its simplest interpretation 36

Figure 3.4: Illustration of tunnel magnetoresistance effect 39

Figure 3.5: Schematic illustration of magnetic pillar switching 40

Figure 3.6: Schematic representation of magnetic tunnel junction (MTJ) 41

Figure 3.7: MTJ with in-plane and perpendicular anisotropy 43

Figure 3.8: Illustration of all-perpendicular and in-plane MTJ MRAM memory cell 44

Figure 3.9: Illustration of p-MTJ MRAM switching by uniform rotation 47

Figure 3.10: Numerical calculation of the critical switching current density for MTJ 48

Figure 3.11: Illustration of write error rate (WER) 51

Figure 3.12: Magnetic tunnel junction-based spintronic devices..... 53

Figure 3.13: Illustration of spin-orbit-torque 54

Figure 3.14: Geometry of a spin-transfer oscillator 56

Figure 3.15: Different configurations of spin-transfer oscillator 57

Figure 3.16: Micromagnetic simulations of perpendicular spin-transfer oscillator..... 59

Figure 3.17: Easy-plane and easy-axis spin-transfer oscillator..... 61

Figure 3.18: Micromagnetic modeling of easy-plane STO..... 62

Figure 3.19: Micromagnetic modeling of easy-axis STO 63

Figure 3.20: Simulations with thermal field for the easy-plane and easy-axis STO..... 64

Figure 3.21: Illustration of spin-transfer oscillator based on antiferromagnets 66

Figure 4.1: Finite element model representation of a spin valve 70

Figure 4.2: Perpendicular magnetic tunnel junction (p-MTJ) stack 75

Figure 4.3: Thermal stability, critical switching current and efficiency of p-MTJ stack... 77

Figure 4.4: Minimal energy path..... 79

Figure 4.5: Magnetostatic field profile in p-MTJ's free layer 81

Figure 4.6: Current-induced magnetization switching of p-MTJ..... 83

Figure 5.1: p-MTJ stack, including ECC free layer and reference layers..... 89

Figure 5.2: Thermal stability, critical switching current density and efficiency of p-MTJ with ECC free layer 91

Figure 5.3: Minimal energy path of p-MTJ with ECC free layer 93

Figure 5.4: Current-induced magnetization switching of p-MTJ with ECC free layer 95

Figure 6.1: p-MTJ's FL with edge roughness 99

Figure 6.2: Minimal energy path of p-MTJ edge roughness 99

Figure 6.3: Current-induced switching of p-MTJ's FL with edge roughness 100

Figure 6.4: Stability and critical switching current of p-MTJ's FL with edge roughness . 101

Figure 6.5: p-MTJ's FL with surface roughness 101

Figure 6.6: Characteristics of p-MTJ's FL with surface roughness 102

Figure 6.7: Illustration of granular p-MTJ's FL 103

Figure 6.8: Thermal stability of granular p-MTJ's FL 103

Figure 6.9: Switching current of granular p-MTJ's FL 104

Figure 6.10: Effect of intergranular coupling in p-MTJ's FL 105

Figure 6.11: Stochastic simulations of granular p-MTJ's FL 106

Figure 6.12: Material parameters distribution in p-MTJ's FL 107

Figure 6.13: Stochastic simulations of p-MTJ's FL with material distribution 108

Figure 7.1: Spin-torque oscillator subjected to applied current and magnetic field 111

Figure 7.2: AF-ECC STO structure. 117

Figure 7.3: Operation of AF-ECC STO 118

Figure 7.4: Elevation and azimuth torques of AF-ECC STO 119

Figure 7.5: Equilibrium state of AF-ECC STO 120

Figure 7.6: Micromagnetic simulations of AF-ECC STO 121

Figure 7.7: Current induced magnetization precession of AF-ECC STO 122

Figure 7.8: Magnetization precession time dependence of AF-ECC STO 123

Figure 7.9: AF-ECC STO operation at room temperature 124

Figure 7.10: Fourier transform for AF-ECC STO at room temperature 125

ACKNOWLEDGEMENTS

I would like to acknowledge my advisor, Professor Vitaliy Lomakin, for his endless support and advice during my doctoral studies at UCSD. This work would not have been possible without his invaluable help, guidance, and mentorship. He has deep knowledge in diverse areas related to electromagnetism and micromagnetism, and I was always impressed by his ability to be so dedicated, optimistic, and at the same time excited about the research of his group. I really enjoyed working with our research group and have a lot of great memories about the traveling to the conferences, hiking, doing April Fools' Day jokes, playing paintball, and enjoying the BBQ events. I was always motivated to do research and truly enjoyed all my years of doctoral study.

From my multiple internships at Samsung's New Memory Technology (NMT) group, I am grateful to my manager Dmytro Apalkov, Sue Wang, Vladimir Nikitin and all my other NMT colleagues. I was always happy and excited to be a part of the team by doing a lot of interesting projects and gaining valuable experience.

I would like to thank Professor Alexandr Dumin from V.N. Karazin Kharkiv National University in Ukraine for being my advisor during my undergraduate years and giving me an opportunity to go for my first internship at UCSD back in 2012. I appreciate all the support through all my years of doctoral study.

I would like to thank David. L. Kenke from Intel Corporation for support and collaboration during my doctoral study at UCSD.

From Professor Lomakin's group I would like to thank Marko Lubarda, who helped me to learn micromagnetism thought fruitful discussions. I want to thank Ruinan Chang,

Sidi Fu and Simon Couture for their advice on programming and theoretical electromagnetism. I am grateful to Majd Kuteifan for his help with MRAM and DMI modeling. I want to thank Marco Menarini for his constant technical support and collaboration. I further acknowledge Zhuonan Lin for his valuable help with the eigen value solver. I want to thank Fangzhou Ai and Xueyang Wang for their advice on computational aspects of magnetism. I thank all the members of my thesis committee for reading this manuscript and providing valuable feedback.

Chapter 4, in part, is a reprint of material as appeared in I. Volvach, J. G. Alzate, Y. J. Chen, A. J. Smith, D. L. Kencke, and V. Lomakin, "Thermal stability and magnetization switching in perpendicular magnetic tunnel junctions," Applied Physics Letters 116, 19 (2020). This work was supported by Semiconductor Research Corporation. The dissertation author was the primary investigator and author of the text used in this chapter.

Chapter 5, in part, is a reprint of material as appeared in I. Volvach, E. E. Fullerton, and V. Lomakin, "Thermal stability and magnetization switching of composite free layer with perpendicular magnetic anisotropy," AIP Advances 11, 1 (2021). This work was supported as part of the Quantum-Materials for Energy Efficient Neuromorphic-Computing (Q-MEEN-C), an Energy Frontier Research Center funded by the U.S. Department of Energy, Office of Science, Basic Energy Sciences under Award #DE-SC0019273 and Extreme Science and Engineering Discovery Environment (XSEDE) supported by NSF Grant #ACI-1548562. The dissertation author was the primary investigator and author of the text used in this chapter.

Chapter 6, in part, is a reprint of material as appeared in I. Volvach, Z. Lin and V. Lomakin, “Perpendicular magnetic tunnel junction with edge and surface roughness and material distribution” currently being prepared for submission. The dissertation author was the primary investigator and author of this material.

Chapter 7, in part, is a reprint of material as appeared in I. Volvach, A. D. Kent, E. E. Fullerton, and V. Lomakin, “Spin-transfer torque oscillator with an antiferromagnetic exchange coupled composite free layer”. Submitted to Physical Review Applied and currently is under review. This work was supported as part of the Quantum-Materials for Energy Efficient Neuromorphic-Computing (Q-MEEN-C), an Energy Frontier Research Center funded by the U.S. Department of Energy, Office of Science, Basic Energy Sciences under Award #DE-SC0019273 and Extreme Science and Engineering Discovery Environment (XSEDE) supported by NSF Grant #ACI-1548562. The dissertation author was the primary investigator and author of this material.

Finally, my deep and sincere gratitude to my family for their continuous and unparalleled love, help and support.

VITA

2021 Ph. D. in Materials Science and Engineering, University of California San Diego

2013 M. S. in Applied Physics and Electrodynamics, V. N. Karazin Kharkiv National University, Ukraine

2008 B. S. in Radiophysics and Electronics, V. N. Karazin Kharkiv National University, Ukraine

PUBLICATIONS

I. Volvach and V. Lomakin, "Coupled micromagnetic SPICE solver for perpendicular magnetic tunnel junctions," *IEEE Transactions on Magnetics*, forthcoming.

I. Volvach, Z. Lin and V. Lomakin, "Perpendicular magnetic tunnel junction with edge and surface roughness," *J. Magn. Magn. Mater.*, forthcoming.

I. Volvach, A. D. Kent, E. E. Fullerton and V. Lomakin, "Spin-transfer torque oscillator with an antiferromagnetic exchange coupled composite free layer," *Phys. Rev. Appl.*, submitted.

I. Volvach, E. E. Fullerton and V. Lomakin, "Thermal stability and magnetization switching of composite free layer with perpendicular magnetic anisotropy," *AIP Advances*, 11, 1 (2021).

I. Volvach, J. G. Alzate, Y. J. Chen, A. J. Smith, D. L. Kencke, and V. Lomakin, "Thermal stability and magnetization switching in perpendicular magnetic tunnel junctions," *Appl. Phys. Lett.*, 116, 19 (2020).

Z. Lin, I. Volvach and V. Lomakin, "Non-uniform current density for switching current reduction in magnetic tunnel junctions," *Appl. Phys. Lett.*, under revision.

Z. Lin, I. Volvach and V. Lomakin, "Eigenvalue-based micromagnetic analysis of switching in spin torque driven structures," *Phys. Rev. Appl.*, under revision.

P. Salev, I. Volvach, D. Sasaki, P. Lapa, Y. Takamura, V. Lomakin, I. K. Schuller, "Voltage-controlled magnetism enabled by resistive switching," *arXiv:2108.06445*, submitted.

S. Fu, R. Chang, I. Volvach, M. Kuteifan, M. Menarini, and V. Lomakin, "Block inverse preconditioner for implicit time integration in finite element micromagnetic solvers," *IEEE Transactions on Magnetics* 55 (12), 1-11 (2019).

V. Lomakin, X. Wang, M. Kuteifan, I. Volvach and M. Menarini, "Fast codes for modeling the magnetization dynamics in magnetic nanostructures," *2018 International Conference on Electromagnetics in Advanced Applications (ICEAA)*, 702-703 (2018).

S. Couture, R. Chang, I. Volvach, A. Goncharov and V. Lomakin, "Coupled Finite-Element Micromagnetic-Integral Equation Electromagnetic Simulator for Modeling Magnetization-Eddy Currents Dynamics," *IEEE Transactions on Magnetics* 53, 12 (2017).

J. K. Byun, I. Volvach, and V. Lomakin, "Fast optimal design of micromagnetic devices using FastMag and distributed evolutionary algorithm," *IEEE Transactions on Magnetics* 52, 9 (2016).

CONFRENCE PRESENTATIONS

I. Volvach and V. Lomakin, "Spin-transfer torque oscillator based on composite synthetic antiferromagnets," *65th Annual Conference on Magnetism and Magnetic materials*, virtual conference, Nov. 2 – Nov. 6, 2020.

I. Volvach and V. Lomakin, "Thermal stability and magnetization switching of exchanged coupled composite free layer of perpendicular magnetic tunnel junction," *65th Annual Conference on Magnetism and Magnetic materials*, virtual conference, Nov. 2 – Nov. 6, 2020.

I. Volvach and V. Lomakin, "Magnetization switching and thermal stability in Perpendicular Magnetic Tunnel Junctions with surface defects," *Special joint poster session on MRAM, IEEE 65th International Electron Devices Meeting IEDM*, San Francisco, CA, USA, Dec. 8 – Dec. 12, 2019.

I. Volvach and V. Lomakin, "Micromagnetic modeling of non-uniformities in magnetic tunnel junctions for MRAM devices," *14th Joint Magnetism and Magnetic Materials-Intermag Conference*, Washington, D. C., USA, Jan. 14 – Jan. 18, 2019.

I. Volvach, M. V. Lubarda and V. Lomakin, "Micromagnetic modeling of non-uniformities in magnetic tunnel junctions for MRAM Devices," *64th International Electron Devices Meeting IEDM*, San Francisco, CA, USA, Dec. 2 – Dec. 9, 2018.

Volvach I, M. Kuteifan, Marko V. Lubarda and V. Lomakin, "Circuit-Integrated Micromagnetic Modeling of MRAM Devices," *62nd Annual Conference on Magnetism and Magnetic Materials*, Pittsburgh, PA, USA, Nov 6. – Nov. 10, 2017.

Volvach I, M. Kuteifan, Marko V. Lubarda and Vitaliy Lomakin, "MRAM circuit solvers and Landau-Lifshitz-Gilbert Equations," *Special joint poster session on MRAM, IEEE 63rd International Electron Devices Meeting IEDM*, San Francisco, CA, USA, Dec. 3 – Dec. 6, 2017.

Volvach I, M. Kuteifan, Marko V. Lubarda and Vitaliy Lomakin, "Coupling MRAM circuit solvers and Landau-Lifshitz-Gilbert equations," *Special joint poster session on MRAM, IEEE 62nd International Electron Devices Meeting IEDM*, San Francisco, CA, USA, Dec. 3 – Dec. 7, 2016.

I. Volvach, M. Kuteifan, M. V. Lubarda and V. Lomakin, "Coupling Landau-Lifshitz-Gilbert equations and circuit solvers," *Nanomaterials 2016*, Nancy, France, Sep. 19 – Sep. 23, 2016.

I. Volvach, M. V. Lubarda and V. Lomakin, "SPICE modeling coupled with LLG equation," *13th Joint MMM – Intermag Conference*, San Diego, CA, USA, Jan. 11 – Jan. 15, 2016.

I. Volvach, M. Escobar, M. Lubarda, and V. Lomakin, "Synchronization in chains of spin transfer torque oscillators," *58th Annual Conference on Magnetism and Magnetic Materials*, Denver, CO, USA, Nov. 4 – Nov. 8, 2013.

I. Volvach, M. Escobar, M. Lubarda, and V. Lomakin, "Synchronization in chains of spin transfer torque oscillators," *Proceedings of the French-US Workshop Toward lower power spintronic devices*, Center for Magnetic Recording Research, University of California, San Diego, CA, USA, Jul. 8 – Jul. 12, 2013.

ABSTRACT OF THE DISSERTATION

MICROMAGNETIC MODELING AND ANALYSIS OF MAGNETIC TUNNEL JUNCTIONS FOR SPINTRONICS APPLICATIONS

by

Iana Volvach

Doctor of Philosophy in Materials Science and Engineering

University of California San Diego, 2021

Professor Vitaliy Lomakin, Chair

Nanomagnetic materials and devices remain at the center of data storage technologies ranging from modern magnetic hard drives to future spintronic devices, such as magnetoresistive or racetrack memory technologies. Because of the continuously increasing demand for more storage density and performance the focus has shifted from magnetic field based applications to spin current based applications. Spintronic devices take advantage of interactions between magnetic materials and electric currents. Spin transfer torque magnetic random access memory devices utilizing perpendicular magnetic tunnel

junctions currently are the most promising candidates for future memory applications. This dissertation present a theoretical and numerical study of challenges faced when considering interactions between electrical spin polarized currents and magnetic tunnel junctions for spintronics device applications. It starts with a short introduction to micromagnetics and a description of main magnetic interactions. It then focuses on the study of properties of perpendicular magnetic tunnel junctions, such as size dependence, thermal stability, critical switching current density, and device efficiency. The following chapters are dedicated to optimal designs of magnetic tunnel junctions, including a study of composite free-layers, surface defects and roughness effects, granularity, and parameters distributions. The study of switching probability or write error rates under non-zero temperatures is also presented. The work also includes a study of antiferromagnetically coupled composite spin-transfer torque nano oscillators. All these chapters contain numerical results and simulations performed by using the FastMag finite element micromagnetic simulation software, developed at UCSD. Some general ideas and details on the computational methods are provided with the intention of assisting in understanding of engineering and analytical aspects of the spintronic devices based on magnetic tunnel junctions.

Part I

Introduction

Chapter 1

Introduction

Technologies based on magnetic materials have a prominent role in our daily life. With the increased use of computers and other electronic devices, demand for information storage using magnetic hard drives is increasing. With the increasing demand for storage capacity driven by the modern data consumption habits, such as high-definition video and extensive use of social networks, new technologies are constantly challenging the market and offering better performances.

Spintronic devices exploiting the spin of the electron are envisioned to revolutionize the electronics industry. The significance of this new generation device is faster memory and lower power consumption at a low electron density. The late 20th century was considered an era of microelectronics. However, the growth of microelectronics is at a major threat to Moore's law, and spintronics may be a solution. Most electronic devices employ circuits that express data as binary digits, or bits (1 and 0) represented by the existence or absence of electric charge. Unlike microelectronics, spintronics exploits spin

up and spin down of the electron to carry information between devices. The discovery of Giant Magnetoresistance (GMR) by Nobel Prize winners A. Fert and P. Grünberg led to the birth of the field of spintronics. This triggered an extensive research effort on spin transport in nanoscale MTJs and other interesting phenomena were realized.

Perpendicular magnetic anisotropy (PMA) materials have unique advantages when used in magnetic tunnel junctions (MTJ), which are the most critical part of spin-torque transfer random access memory devices (STT-RAMs) that are being researched intensively as a future non-volatile memory technology. They have high magnetoresistance which improves their sensitivity. The STT-RAM has several advantages over competing technologies, including a low power consumption, non-volatility, ultra-fast read and write speed and high endurance. In personal computers, it can replace SRAM for high-speed applications, Flash for non-volatility, and PSRAM and DRAM for high-speed program execution.

This dissertation presents research of the spintronic nanodevices based on perpendicular MTJ. This work also covers the main micromagnetic modeling aspects of the magnetization behavior of the spintronic devices under the effect of applied current or external magnetic field. Simulation is an essential tool for research and development especially when it comes to exploring the possibilities offered by spintronic technologies. The interactions between electrical currents and the magnetization is handled by the micromagentic simulatoe FastMag, which was developed at UCSD. By taking advantage of high-performance Graphics Processing Units (GPUs) and latest algorithms, the FastMag micromagnetic solver can compute the dynamics of magnetization within nanoscale to microscale magnetic materials and devices efficiently. It is a flexible software that offers a

wide range of possibilities, from simulating current interactions to complex write head modeling, and allows for time-domain simulations as well as other algorithms used to compute energy barriers or thermal stability. Through different devices and designs, advantages, and drawbacks of some of the previously mentioned technologies are evaluated and studied.

This dissertation has two main parts. Part I (chapter 1 and 2) introduces the general concepts of micromagnetism for the spintronic nanodevices that are used for micromagnetic numerical simulations in Part II. Part I (chapter 3) introduces the concept of magnetic memory, describes the current magnetoresistive memory technology, and focuses on the basic principles of operation and the nature of the phenomena of magnetoresistance changes (GMR and TMR). Furthermore, the basic architecture of the magnetoresistance memory cells is presented, and the major problems are identified. Chapter 3 also provides an overview of known types of p-MTJ-based magnetic nano-oscillators and their operation characteristics.

Part II (chapter 4,5,6 and 7) is devoted to micromagnetic modeling and analysis of spintronic devices.

Chapter 4 introduces the typical design and the main characteristic of the perpendicular magnetic tunnel junction. Thermal stability, current induced magnetization switching, magnetization dynamics and the device efficiency are studied.

Chapter 5 studies the perpendicular magnetic tunnel junction with composite free layer. Thermal stability, current induced magnetization switching, magnetization dynamics and the device efficiency are studied as a function of the material composition and the geometrical sizes of the composite sublayers.

Chapter 6 discusses effects of the edge and surface roughness in the perpendicular magnetic tunnel junction. It also discusses effects of granularity of the free layer of the magnetic tunnel junction as well as presents the device's operation and current-induced switching at zero and room temperatures.

Chapter 7 studies a spin transfer nano-oscillator based on antiferromagnetically exchange coupled composite free layer. The operational modes and characteristics at high and low frequencies are discussed. The chapter also provides the discussion about comparisons of the different types of known nano-oscillators and their operation at zero and room temperatures.

Finally, Chapter 8 contains concluding remarks and an outlook for future research.

Chapter 2

Basic concepts of micromagnetism

Several methods and approaches are used to describe and predict the behavior of a magnetic system. The processing capability of modern computers is rapidly increasing and brings a surge of interest in the field of computer-based simulations. Micromagnetics is a discipline of physics that studies and predicts the interaction between magnetic particles at the micrometer scale. William F. Brown developed a continuum theory of ferromagnetism, a fundamental theory of micromagnetics that found its applications in engineering and physics. His mathematical equations were used to predict equilibrium magnetization configurations based on a set of continuous material parameters [1]. An important differential equation, referred to as Landau-Lifshitz-Gilbert (LLG) equation, describes the precessional motion of the magnetization vector in magnetic systems [2] by considering the energies related to different interactions. Additional terms in the LLG equation may include exchange or interfacial interaction, and interaction with spin currents [3]. This chapter discusses and provides analytical expressions for main micromagnetic interactions.

2.1 Micromagnetic model representation

We use an FEM based micromagnetic approach. For any finite element micromagnetic model, it is important, first, to generate a model to be studied. The size of the models is typically varying from a few nanometers to a hundred of microns. Proper meshing scheme are important to improve the accuracy of the results. Figure 2.1 shows different examples of structures discretized into a mesh of tetrahedrons and connections between its nodes. The connections between the nodes provide the essential information about interaction proximity for simulation components calculations, such as Laplace and gradient matrices.

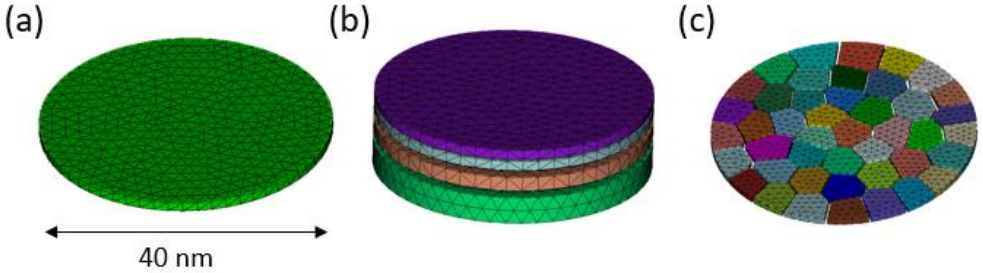

Figure 2.1: Micromagnetic model representation with tetrahedral discretization for different geometry types. (a) standalone thin cylinder. (b) set of the thin interacting cylinders. (c) granular media representation.

Each color encodes a different material present in the considered model. From the micromagnetic point of view each node of the tetrahedron is considered as a separate effective magnetic moment, which interacts with other moments. The mesh element edge length should be small enough to resolve the physical length scales. The total number of the nodes in a numerical model is often limited by the computer memory and computational

capabilities. As an example, micromagnetic models of magnetic write heads or granular recording media can have millions of nodes and it requires high-performance simulation techniques and computational resources.

2.2 Landau-Lifshitz-Gilbert equation

The Landau-Lifshitz-Gilbert (LLG) differential equation is a fundamental equation that describes the magnetization dynamics and interactions in magnetic systems. The LLG equation can be written in the following implicit form [2,4]:

The Landau-Lifshitz-Gilbert (LLG) differential equation is a fundamental equation that describes the magnetization dynamics and interactions in magnetic systems. The LLG equation could be represented as in [2,4]:

$$\frac{d\mathbf{M}}{dt} = -\gamma \mathbf{M} \times \mathbf{H}_{eff} + \frac{\alpha}{M_s} \mathbf{M} \times \frac{d\mathbf{M}}{dt}, \tag{2.1}$$

where $\mathbf{M}$ is the magnetization vector, M_s is saturation magnetization, $\mathbf{H}_{eff}$ is the effective magnetic field, and α is damping constant. The parameter γ represents a gyromagnetic ratio and could be expressed as a ratio of the electron magnetic moment μ and its angular momentum L:

$$\gamma = \frac{\mu}{L} = \frac{g|e|}{2m_e}, \tag{2.2}$$

where g is the g-factor for free electrons, e and m_e are the electron charge and mass, respectively.

The LLG equation is a non-linear differential equation and the effective field $\mathbf{H}_{eff}$ depends on the state of the magnetization. The Equation 2.1 is in implicit form and

inconvenient to use, because it has the time derivative of the magnetization $\frac{d\mathbf{M}}{dt}$ on both sides. To solve (2.1) numerically with a simple time solver the explicit form of the equation (2.1) could be derived from its implicit form (2.1) as:

$$\frac{d\mathbf{M}}{dt} = -\gamma \mathbf{M} \times \mathbf{H}_{eff} + \frac{\alpha}{M_s} \mathbf{M} \times \left(-\gamma \mathbf{M} \times \mathbf{H}_{eff} + \frac{\alpha}{M_s} \mathbf{M} \times \frac{d\mathbf{M}}{dt} \right), \tag{2.3}$$

Using the identity $\mathbf{M} \times \mathbf{M} \times \frac{d\mathbf{M}}{dt} = -\frac{d\mathbf{M}}{dt}$ and since $\frac{d\mathbf{M}}{dt}$ and $\mathbf{M}$ are perpendicular to each other the equation (2.3) could be written as:

$$\frac{d\mathbf{M}}{dt} = -\frac{\gamma}{1+\alpha^2} \mathbf{M} \times \mathbf{H}_{eff} - \frac{\gamma\alpha}{1+\alpha^2} \mathbf{M} \times \mathbf{M} \times \mathbf{H}_{eff} \,. \tag{2.4}$$

The equation (2.4) represents the explicit form of the LLG equation. Here, $\mathbf{M}$ is normalized by M_s.

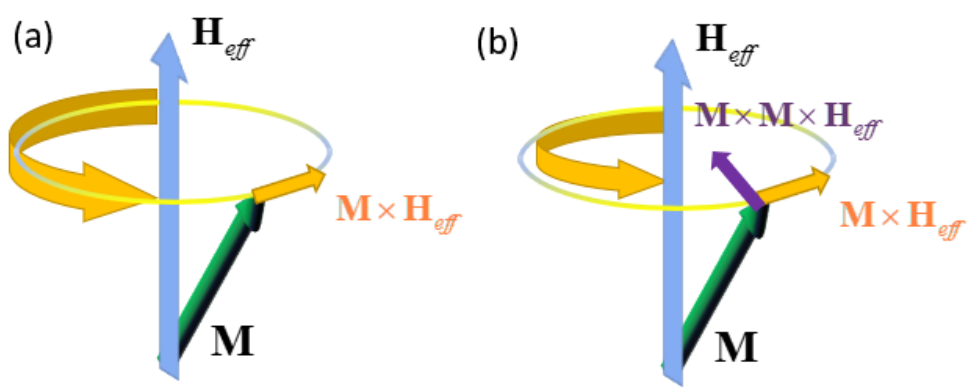

Figure 2.2: Illustration of the magnetization precession. Magnetization precession for (a) without damping, (b) with damping.

The right-hand side of the equation (2.4) consists of two terms. The first term has $\mathbf{M} \times \mathbf{H}_{eff}$ and describes the precession of magnetic moment $\mathbf{M}$ about the vector of effective magnetic

field $\mathbf{H}_{eff}$ as shown on the Figure 2.2 (a). The second term has $\mathbf{M}\times\mathbf{M}\times\mathbf{H}_{eff}$ and represents the damping in the system. The damping process leads the magnetization $\mathbf{M}$ to align with the effective magnetic field $\mathbf{H}_{eff}$ and at the same time the magnetization magnitude $\mathbf{M}$ should remain constant (Fig. 2.2 (b)).

2.3 Landau-Lifshitz-Gilbert-Slonczewski equation

The interactions in the magnetic system that are considered as a part of the effective field $\mathbf{H}_{eff}$ vary depending on the considered model. For example, the LLG equation (2.4) could be used to describe the switching in magnetic random-access memory (MRAM) by magnetic field. To describe a current induced switching in spin transfer torque (STT) MRAM the LLG equation (2.1) must be updated with an additional spin transfer torque term $\boldsymbol{\tau}$ as follows [5]:

$$\frac{d\mathbf{M}}{dt} = -\gamma\mathbf{M}\times\mathbf{H}_{eff} + \alpha\mathbf{M}\times\frac{d\mathbf{M}}{dt} + \boldsymbol{\tau}\,, \tag{2.5}$$

Equation (2.5) gives a general form of Landau-Lifshitz-Gilbert-Slonczewski (LLGS) equation. The Slonczewski's spin transfer torque term is defined as [6]:

$$\boldsymbol{\tau} = a(j)\mathbf{M}\times\mathbf{M}\times\mathbf{p} + b(j)\mathbf{M}\times\mathbf{p}\,. \tag{2.6}$$

Here, $\mathbf{p}$ is normalized magnetization vector of the polarizing (fixed) layer for which the magnetization is considered constant, $a(j)$ and $b(j)$ are the spin-current-depending functions for in-plane and perpendicular spin transfer torque.

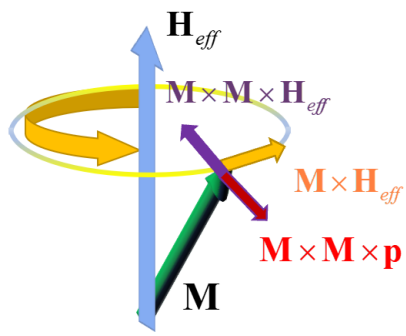

Figure 2.3: Illustration of the Landau-Lifshitz-Gilbert-Slonczewski equation.

The LLGS equation and its application for the study of different spintronic devices are considered in Chapters 4, 5, 6, 7.

2.4 Main interactions in micromagnetics

2.4.1 Effective magnetic field

This section describes the fundamental interactions that are usually considered in micromagnetics. There is a number of interactions that can be included in the micromagnetic model. Most of them are often have negligible contribution and should be considered if needed to save the computational resources. The effective magnetic field $\mathbf{H}_{eff}$ in the LLG equation (2.1) represents the sum of the fields originating from different interactions. In general, $\mathbf{H}_{eff}$ can be expressed in terms of the functional derivative of the potential magnetic energy density E, with respect to the magnetization $\mathbf{M}$ [7]:

$$\mathbf{H}_{eff} = -\frac{dE}{d\mathbf{M}}, \tag{2.7}$$

The effective magnetic field contains the following contributions:

$$\mathbf{H}_{eff} = \mathbf{H}_{Zee} + \mathbf{H}_{ms} + \mathbf{H}_{anis} + \mathbf{H}^{s}_{anis} + \mathbf{H}_{ex} + \mathbf{H}_{iex} . \tag{2.8}$$

Here, $\mathbf{H}_{Zee}$ is the external magnetic or Zeeman field, $\mathbf{H}_{ms}$ is the magnetostatic field, $\mathbf{H}_{anis}$ and is the magnetocrystalline bulk anisotropy field, $\mathbf{H}^{s}_{anis}$ surface anisotropy field, $\mathbf{H}_{ex}$ and $\mathbf{H}_{iex}$ is the bulk and interlayer exchange magnetic field, respectively. Next sections briefly explain each field in (2.8) resulting from the different interactions. It is convenient to do it by using equation (2.7) and sum all the fields up to get the total effective field $\mathbf{H}_{eff}$ as it shown in equation (2.8).

2.4.2 Zeeman interaction

The Zeeman interaction is the interaction between an external applied magnetic field $\mathbf{H}_{Zee}$ and the magnetization of the system $\mathbf{M}$. The Zeeman field is the magnetic field $\mathbf{H}_{Zee}$ that is applied externally on a sample. The potential energy of the magnetic system under the presence of an external applied field $\mathbf{H}_{Zee}$ could be written as:

$$E = -\int_{V} \mathbf{M} \cdot \mathbf{H}_{Zee} dV . \tag{2.9}$$

It should be noted that when $\mathbf{M}$ and $\mathbf{H}_{Zee}$ have the same direction the potential energy E is minimized, i.e. the magnetic moments are aligned with the direction of the external magnetic field. The external magnetic field $\mathbf{H}_{Zee}$ value is typically known in advance and directly added into the total effective field $\mathbf{H}_{eff}$, as in equation (2.8).

2.4.3 Magnetostatic interaction

Let us start by considering a system of several magnetic moments. We can consider that each of the magnetic moments produces its own magnetic field. That means that magnetic moments are interacting with each other via dipolar magnetic fields, which are also referred to as magnetostatic or demagnetization magnetic fields. The magnetic field produced by a dipole is calculated based on either a pair of charges or a loop with a current as shown in Figure 2.4. The two models for a dipole (current loop and magnetic poles), give the same result for the magnetic field far from the source.

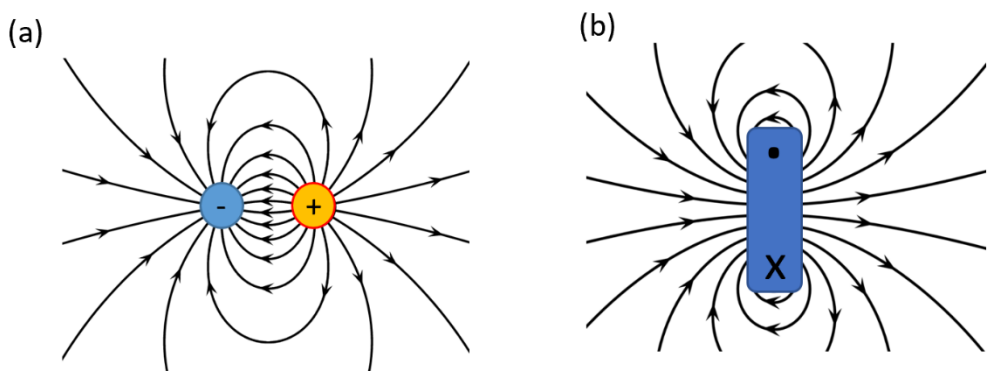

Figure 2.4: Magnetic field calculation approximations. (a) Magnetic moment representation with two opposing charges separated by a finite distance. The arrows represent the direction of the magnetic field, (b) The magnetic field of a current loop.

For a current loop representation the magnetic field is calculated based on vector potential as shown in [8]. The magnetic field generated by a small magnetic dipole could be represented as [8]:

$$\mathbf{H}_{dip}(\mathbf{r}) = \frac{1}{4\pi}\left[\frac{3\mathbf{r}(\mathbf{M}\cdot\mathbf{r})}{r^5} - \frac{\mathbf{M}}{r^3}\right], \tag{2.10}$$

where $\mathbf{M}$ is the magnetic moment of the dipole and $\mathbf{r}$ is a vector which represents the distance between the source and the observation point. The magnetostatic energy of the whole system could be represented as:

$$E_{ms} = -\frac{1}{2}\int_V \mathbf{M}\cdot\mathbf{H}_{dip}dV\ , \tag{2.11}$$

And for the system of N magnetic moments the magnetostatic energy could be rewritten as:

$$E_{ms} = -\frac{1}{2}\sum_{m=0}^{N}\sum_{\substack{n=0\\ n\neq 0}}^{N} V_m \mathbf{M}_m \cdot \mathbf{H}_{n,demag|m}\ . \tag{2.12}$$

The magnetostatic interaction is very important in understanding the static and dynamic nature of magnetization behavior. Consider a uniform array of magnetic nanoislands, as illustrated in Figure 2.5. Assume that each nanoisland could be considered as a separate magnetic dipole moment at sub-exchange length dimensions. The effect of exchange interaction detailed in section 2.4.5 results in neighboring magnetic nanoislands tending to stay parallel to each other. The magnetostatic energy in this case is minimized when neighbor nanoislands have opposite moment directions because such a configuration maximizes the magnetic flux closure.

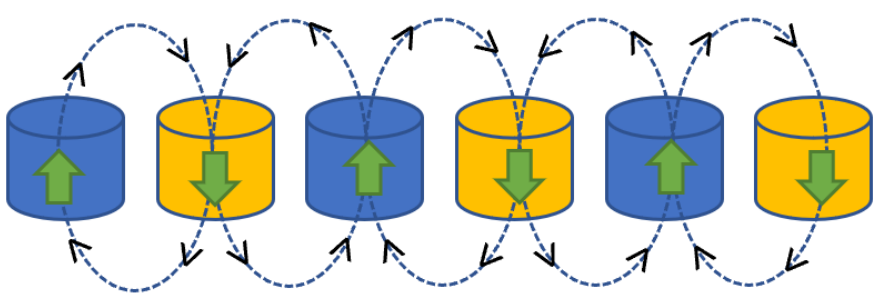

Figure 2.5: Illustration of the dipolar coupling between magnetic nanoislands.

Figure 2.6 shows the examples of the effect of the magnetostatic interaction that occurs in various samples. One of the examples of magnetostatic interactions is prevention of the existence of the magnetic charges in multidomain magnetic structure (Figure 2.6 (a)). Figure 2.6 (b) shows that due to strong external magnetic field the magnetization orientation of the magnetic bar aligns with the direction of the external magnetic field. Another example is the minimal energy state that resulted in magnetization points along the long axis of the continuous magnetic nanowire, as shown in Figure 2.6 (c).

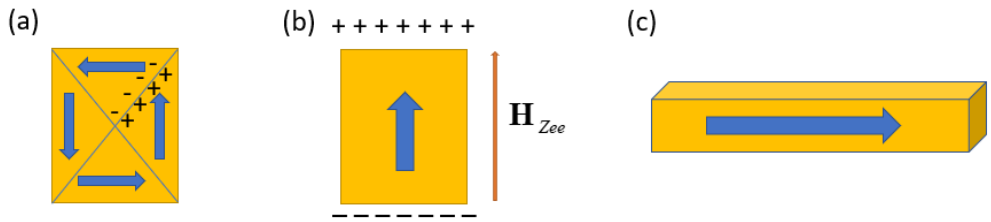

Figure 2.6: Examples of the effects of the magnetostatic interaction: (a) The illustration of a magnet with four magnetic closure domains. The charges of the spins within the multidomain structure are compensated because of dominant demagnetization field in the structure. (b) The magnetization orientation of the single domain magnetic bar due to the strong external field. The magnetic charges are concentrated at on both edges of the magnetic bar. (c) Effect of shape anisotropy in continuous magnetic nanowire.

From the computational point of view, calculating the demagnetization magnetic field sometimes could be very costly. This is because for a system of interacting magnetic moments, the complexity of computation scales quadratically with the number of the magnetic moments in the system. As a result, it can significantly slow down simulation time, especially in the case of large magnetic systems. One of the possible ways to get around this problem is to consider uniform magnetization within a volume. The magnetic charges that appear at the surfaces of the volume generate the demagnetization field. To simplify the calculation of the demagnetization field it is common to use the

demagnetization factor. The demagnetization factor depends on the geometrical sizes and shape of the considered magnetic volume. The matrix that describes the demagnetization factors called the demagnetization tensor. The demagnetization magnetic field could be represented in terms of demagnetization tensor as [9]:

$$\mathbf{H}_{demag} = -\begin{bmatrix} N_{xx} & N_{xy} & N_{xz} \\ N_{yx} & N_{yy} & N_{yz} \\ N_{zx} & N_{zy} & N_{zz} \end{bmatrix}\mathbf{M}, \tag{2.13}$$

where the elements N_{mn} of the matrix are the demagnetization factors. The diagonal elements of the matrix (2.13) are positive, and its trace is equal 1. In the magnetic structures that have single or several planes of symmetry it can be found that $N_{mn,m\neq n} = 0$. For example, in case of the magnetic sphere any axis that goes through the center of the sphere is the axis of its symmetry and the only non-zero elements of the matrix (2.13) will be the diagonal elements. The demagnetization tensor of the sphere could be represented as $N_{xx} + N_{yy} + N_{zz} = 1/3$. This means that within the magnetic sphere there is no preferred direction of the magnetization $\mathbf{M}$, i.e. the direction of the demagnetization magnetic field $\mathbf{H}_{demag}$ will be always opposite to the direction of the magnetization $\mathbf{M}$. For the perpendicularly magnetized in z-direction infinite (in xy-plane) magnetic thin film the demagnetization factor would be $N_{zz} = 1$. In this case the demagnetization field will try to push the magnetization in xy-plane. However, if the same thin film is magnetized in x or y-direction the demagnetization field does not exist. The magnetization vector $\mathbf{M}$ will stay in the plane of the magnetic thin film. Using equation (2.11) the magnetostatic energy per unit volume of a perpendicularly magnetized thin film could be written as:

$$E_{ms} = 2\pi M_s^2 . \tag{2.14}$$

Another example of the most common shape in magnetic memory technology is a cylinder. For a magnetic circular cylinder the demagnetization factors are represented as [10]:

$$\begin{aligned} N_z &= \frac{1}{L}\left(L + R - \sqrt{L^2 + R^2}\right), \\ N_x + N_y + N_z &= 1, \\ N_x = N_y &= \frac{1}{2}\left(1 - N_z\right) = \frac{1}{2L}\left(\sqrt{L^2 + R^2} - R\right). \end{aligned} \tag{2.15}$$

where L and R are the thickness and the radius of the circular cylinder as it shown in Figure 2.7.

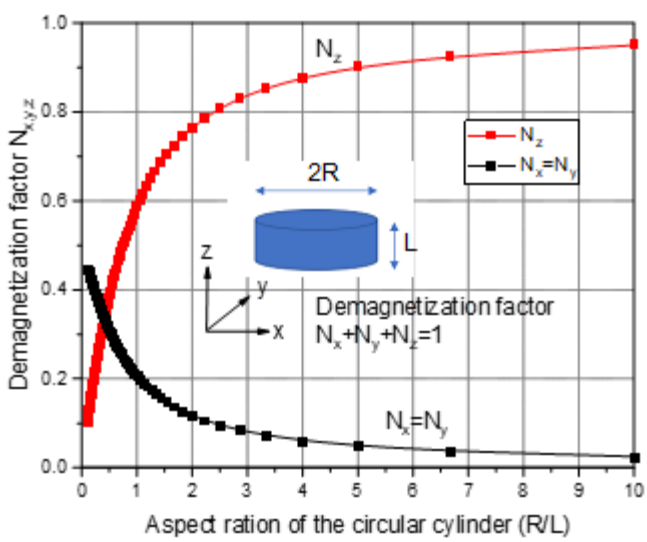

Figure 2.7: Demagnetization factor as a function of aspect ratio for right circular cylinder for the averaged magnetic field along the cylinder axis.

Figure 2.6 shows the behavior of the demagnetization factors as a function of aspect ratio for right circular cylinders, based on Equations (2.15). We assume that the magnetic

field is averaged along the cylinder axis. magnetic field. The point where $N_x + N_y + N_z = 1/3$ is close to the radius such that $2R = L$. For very skinny cylinders with $R \ll L$, the longitudinal demagnetization factor is $N_z \to 0$ while the transverse factors are $N_x = N_y \to 1/2$. At the other limit, for a very flat cylinder, $R \gg L$, we have $N_z \to 1$ and $N_x = N_y \to 0$. The flat cylinder has no demagnetization effect within the xy-plane. The greatest demagnetization effects will always take place through the shortest dimension of the object [10]. The demagnetization effects play an important role in micromagnetic modeling and simulations of the magnetic system.

Sometimes the demagnetization factors can not accurately represent the dipolar field in the simulation due to non-uniform magnetization profile in the system. In micromagnetic simulations, the position of all nodes is known in advance so the demagnetization tensor should be computed for each node using (2.10) as it shown in [11]:

$$D_{mn} = \frac{1}{4\pi \left\| \mathbf{r}_{mn} \right\|^3} \begin{bmatrix} 3r_{mn,x}^2 - 1 & 3r_{mn,x} r_{mn,y} & 3r_{mn,x} r_{mn,z} \\ 3r_{mn,y} r_{mn,x} & 3r_{mn,y}^2 - 1 & 3r_{mn,y} r_{mn,z} \\ 3r_{mn,z} r_{mn,x} & 3r_{mn,z} r_{mn,y} & 3r_{mn,z}^2 - 1 \end{bmatrix}, \tag{2.16}$$

where m, n are the couple of corresponding nodes and $\mathbf{r}_{mn}$ is the distance between the nodes. The corresponding demagnetization field could be represented as [11]:

$$\mathbf{H}_{demag,m} = \sum_{\substack{n=0 \\ n \neq m}}^{N} D_{mn} \mathbf{M}_n . \tag{2.17}$$

The general formulas to compute the demagnetizing factors are given in [10]. This will be useful for chapter 3, where the demagnetization factors of the cylindrical perpendicular magnetic tunnel junction will be discussed in detail.

2.4.4 Magnetocrystalline anisotropy

The magnetic anisotropy characterizes the ferromagnetic material and describes the fact that the properties of the magnetic material are unequal in different directions.

In general, the magnetic anisotropy could have several possible sources: the properties related to the lattice structure of the magnetic material (magnetocrystalline anisotropy), the properties of the interface between two magnetic films (interface anisotropy), and the shape of the magnetic sample (shape anisotropy). The interface anisotropy is important for description of structures with perpendicular magnetization. The shape anisotropy is defined by the energy of demagnetization.

Bulk anisotropy

The magnetocrystalline anisotropy can have the form of a uniaxial or a cubic anisotropy. The uniaxial anisotropy is characterized by an existence of a single easy axis corresponding to two antiparallel preferential directions of the magnetization orientation in magnetic material. This property is used for data storage, where the detection of these states can correspond to reading a 1 or a 0, the elementary components of binary data [11]. The potential energy for a uniaxial anisotropy is represented as [7,11]:

$$E_{anis} = K_1 V \sin^2(\theta) + K_2 V \sin^4(\theta), \tag{2.18}$$

where K_1 and K_2 are the first and the second order anisotropy coefficients in CGS units of $\mathrm{erg/cm^3}$, V is the volume of magnetic moment and θ is the angle between the easy axis and the magnetic moment. The energy is minimized when $\theta = 0, \pi$, i.e. when the magnetization is oriented along the easy axis. The general expressions for the uniaxial

anisotropy energy over a volume and the correspondent magnetic anisotropy field could be written as in [11] using (2.7) and (2.18):

$$\begin{aligned} E_{anis} &= \int_V \left(K_1 \left(1 - \left(\mathbf{M} \cdot \mathbf{k} \right)^2 \right) + K_2 \left(1 - \left(\mathbf{M} \cdot \mathbf{k} \right)^2 \right)^2 \right) dV, \\ \mathbf{H}_{anis} &= \frac{2K_1}{M_s} \left(\mathbf{M} \cdot \mathbf{k} \right) \mathbf{k} + \frac{4K_2}{M_s} \left(1 - \left(\mathbf{M} \cdot \mathbf{k} \right)^2 \right) \left(\mathbf{M} \cdot \mathbf{k} \right) \mathbf{k}. \end{aligned} \tag{2.19}$$

Here, $\mathbf{k}$ is the uniform anisotropy axis vector and $\mathbf{M}$ is the magnetic moment. In various cases the second order anisotropy term K_2 is set to 0 which simplifies the expressions for magnetic anisotropy (2.19).

In the case of cubic anisotropy the equation for the anisotropy energy could be written as [7,11]:

$$\begin{aligned} E_{anis} &= K_1 \left(M_1^2 M_2^2 + M_1^2 M_3^2 + M_2^2 M_3^2 \right) + K_2 M_1^2 M_2^2 M_3^2, \\ M_n &= \mathbf{M} \cdot \mathbf{k}_{c,n}, \end{aligned} \tag{2.20}$$

where $\mathbf{k}_{c,n}$, $n = 1, 2, 3$ are the three different anisotropy easy axes associated with crystallographic directions and K_1, K_2 are the anisotropy constants in CGS units. The correspondent magnetic anisotropy field for cubic anisotropy could be expressed using (2.7) and (2.20):

$$\mathbf{H}_{anis} = -\frac{1}{M_s} \begin{bmatrix} 2K_1 M_1 \left(M_2^2 + M_3^2 \right) + 2K_2 M_1 M_2^2 M_3^2 \\ 2K_1 M_2 \left(M_1^2 + M_3^2 \right) + 2K_2 M_1^2 M_2 M_3^2 \\ 2K_1 M_3 \left(M_1^2 + M_2^2 \right) + 2K_2 M_1^2 M_2^2 M_3 \end{bmatrix}. \tag{2.21}$$

Surface anisotropy

The surface or interface anisotropy energy density and the corresponding surface anisotropy field in general form can be represented as:

$$E_{anis}^{s} = -\int_{S} K_s \left(\mathbf{M}\cdot\mathbf{k}^s\right)^2 dS$$
$$\mathbf{H}_{anis}^{s} = \frac{2K_s}{tM_s}\left(\mathbf{M}\cdot\mathbf{k}^s\right)\mathbf{k}^s \quad . \tag{2.22}$$

where K_s $\left(\mathrm{erg}/\mathrm{cm}^2\right)$ is the anisotropy energy density per unit surface area and t is the thickness of the magnetic layer.

When considering the micromagnetic finite element analysis the anisotropy field at one node does depend on magnetization states of the other nodes which is different for the exchange or magnetostatic interactions.

2.4.5 Exchange interaction

Bulk exchange interaction

In magnetic materials the magnetic moments of the neighboring spins are arranged themselves into certain order due to the exchange interaction. The Pauli's exclusion principle is a quantum mechanical principle that states that two or more identical electrons cannot occupy the same quantum state. The exchange energy for two spins $\mathbf{S}_1$ and $\mathbf{S}_2$ could be written as:

$$E_{ex} = -J_{ex}\mathbf{S}_1\cdot\mathbf{S}_2 . \tag{2.23}$$

where J_{ex} is an exchange constant. The sign of J_{ex} is important since it defines the type of the exchange.

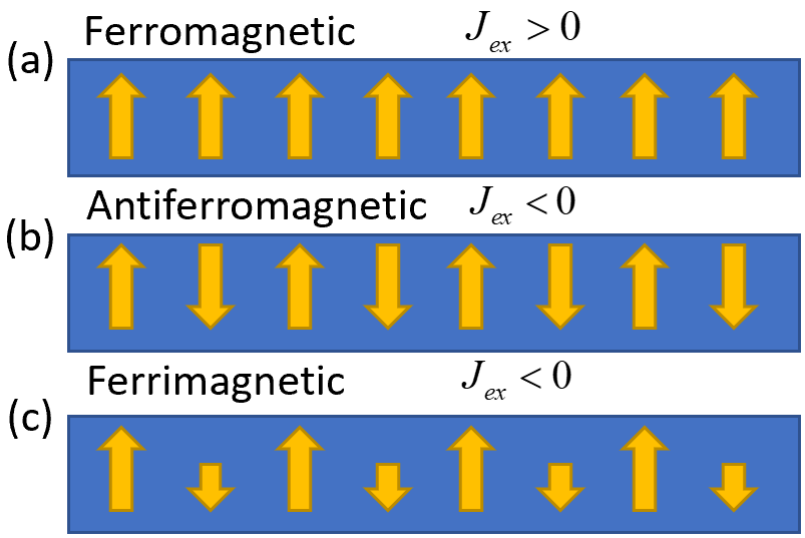

Figure 2.8: Illustration of the magnetic moments orientation: (a) ferromagnetic material, (b) antiferromagnetic material, (c) ferrimagnetic material.

When $J_{ex} > 0$ the material is considered ferromagnetic which has the minimum energy E_{ex} when the neighboring magnetic moments are aligned in the same direction. When $J_{ex} < 0$ the material is ferrimagnetic. The orientation of the neighboring magnetic moments of the ferrimagnetic material have antiparallel orientation but the magnetic moments do not cancel each other. For antiferromagnetic materials $J_{ex} < 0$ and the neighboring magnetic moments are antiparallel and cancel each other.

The equation (2.22) describes the exchange interaction between two spins. Micromagnetic models does not allow you to simulate the atoms because they typically integrate the continuous energies over the shape discretized with finite elements. The continuous representation of the exchange interaction is derived from Heisenberg Hamiltonian and could be written as [12]:

$$E_{ex} = \int_V A\left(\nabla \mathbf{M}\right)^2 dV \,, \tag{2.24}$$

where A is the exchange energy density in $\mathrm{erg/cm}$ that depends on J_{ex}.

The bulk exchange field could be written using (2.7) and (2.23) [7]:

$$\mathbf{H}_{ex} = \frac{2A}{M_s}\nabla^2\mathbf{M}. \tag{2.25}$$

It should be mentioned that the micromagnetic modeling of the exchange interaction in the ferrimagnetic materials as in equation (2.24) is complicated. This is because the micromagnetic simulator does not simulate the interaction between the atoms.

Interface exchange interaction

Interface exchange interaction occurs when two magnetic materials are coupled via a thin $(t \approx 1.0\,\mathrm{nm})$ interlayer layer. This exchange interaction are called Ruderman-Kittel-Kasuya-Yosida (RKKY) interaction [13]. The magnitude of the interface exchange interactions and their signs can be changed by tunning the material and thickness of the interlayer [14-16]. This gives the ability to obtain both ferromagnetic and antiferromagnetic coupling configurations. The general expression for the potential energy of RKKY interaction can be written as:

$$E_{RKKY} = -\int_S J_C \mathbf{M}_1 \cdot \mathbf{M}_2 dS, \tag{2.26}$$

where J_C is the interface exchange energy density in $\mathrm{erg/cm^2}$ (CGS units), $\mathbf{M}_1$ and $\mathbf{M}_2$ are the normalized magnetization vectors for both sides of the interface. The micromagnetic implementation of the interface exchange coupling requires specific methods. The material at the interface that separates the magnetic materials is non-magnetic, and in micromagnetic simulations does not need to be discretized. The modeling of the interlayer exchange

coupling is done through the mirroring scheme of the surfaces on the interfaces of the magnetic materials. The coupled surfaces on the interfaces have the same discretization so that nodes on one surface can find their neighbor on the opposite surface. The corresponding interface exchange field exerted by the magnetic moment $\mathbf{M}_1$ on its neighbor interface magnetic moment $\mathbf{M}_2$ and vice versa, can be represented using (2.7) and (2.26) as:

$$\begin{aligned} \mathbf{H}_{iex,1} &= \frac{J_C}{M_{s1}t_1}\mathbf{M}_2, \\ \mathbf{H}_{iex,2} &= \frac{J_C}{M_{s2}t_2}\mathbf{M}_1. \end{aligned} \tag{2.27}$$

where t_1 and t_2 are the corresponding effective thicknesses at the nodes representing $\mathbf{M}_1$ and $\mathbf{M}_2$. The effective thickness can be found as a ratio between the effective volume and the effective surface. The effective volume is defined as one fourth of the sum of the volumes of all tetrahedrons containing it. Similarly, the effective surface is defined as one third of the sum of all surface triangles containing it.

2.4.6 Spin-transfer torque and interaction with spin currents

The ability of an unpolarized current of electrons to become spin polarized when passing through a ferromagnet implies that angular momentum can be transferred between the incident electrons and the ferromagnetic lattice. As it mentioned in [17] this means that the lattice must be capable of absorbing the angular momentum from the itinerant electrons. This effect is known as the spin transfer torque (STT) effect and was originated by [18,19].

The STT effect offers the usage of currents to locally manipulate magnetization states of magnets.

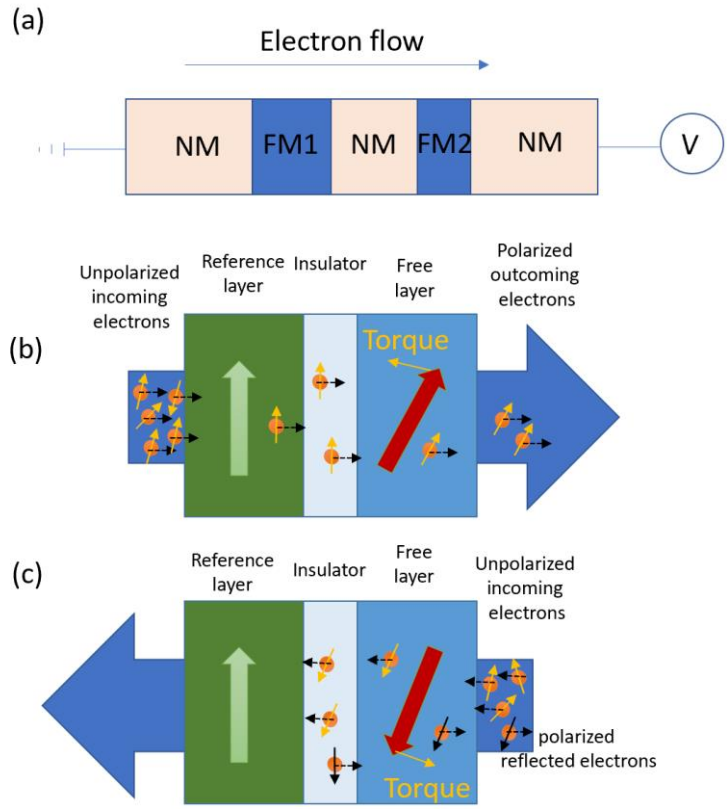

Figure 2.9: Illustration of spin-transfer torque. (a) Spin valve representation: ferromagnetic/non-magnetic metal/ferromagnetic junction connected to nonmagnetic leads. (b) Magnetic tunnel junction with positive currents. The first ferromagnetic layer crossed by the incoming electrons is the reference layer and acts as a polarizer. After tunneling, the electrons realign their magnetic moment along the magnetization of the free layer, which results in applying a spin-transfer torque (STT), (c) when the current is reversed, the spin-transfer torque acting on the free layer is due to electrons reflected from the reference layer.

Figure 2.9 represents the NM/FM1/NM/FM2/NM junction through which the electric current is passing. Both ferromagnets FM1 and FM2 are considered soft magnetic materials and have uniform magnetization with the vertical easy axis established by the shape anisotropy. The first magnetic layer FM1 is thick and serves as a polarizer for the current. FM1 is thick enough and its magnetic moment is large enough to be noticeably

affected by the transfer of angular momentum from the itinerant electrons. The second layer FM2 has a lower magnetic moment, which can be affected by STT. The STT effect can be used for a current-induced magnetization switching of FM2. An alternative application of STT is to drive FM2 into steady precession, which is achieved when the rate of angular momentum pumped into the magnet equals the rate of angular momentum dissipation due to damping. Also, it is possible to have a simultaneous precession of both FM1 and FM2 when they are thin [18,20]. A one-dimensional model originally employed to demonstrate quantum mechanically the transfer of angular momentum between a ferromagnet and itinerant spins is presented in [18,19,21].

2.5 Nudged elastic band method

Magnetization switching and dynamics are one of the most studied topics in micromagnetics due to the importance in controlling of the device behavior. Several methods have been developed and implemented to predict the critical magnetization properties, including minimum energy paths between two energy states or the calculation of thermal stability factor for the magnetic tunnel junctions [22-24]. The nudged elastic band (NEB) is a method for finding saddle points and minimum energy paths between two equilibrium states. The method is based on defining several intermediate states, referred to as images, along the reaction path and minimizing the energy along the path determined by these images [25-27]. The energy barrier is directly related to the thermal stability factor since it corresponds to the energy that must be overcome for thermal switching.

The stability (life) time for at a given temperature is related to the energy barrier via:

$$\tau = \tau_0 e^{\frac{\Delta E}{k_B T}}, \tag{2.28}$$

where τ_0 is the inverse of the attempt frequency, ΔE is the energy barrier, k_B is the Boltzmann constant and T is the temperature. The typical energy barrier aimed in magnetic recording or memories is about $80 k_B T$. In the NEB method, each image represents certain magnetization state $\mathbf{M}_n$. The initial images are guessed either analytically, e.g., assuming uniform rotation, or by LLG simulations of a switching path. The path finding procedure is by an energy gradient descent scheme as [11]:

$$\begin{aligned} \frac{d\mathbf{M}_n}{d\xi} &= -\left[\nabla E_n - \left(\nabla E_n \cdot \mathbf{t}_n\right)\mathbf{t}_n\right], \\ \mathbf{t}_n &= \frac{\mathbf{M}_{n+1} - \mathbf{M}_{n-1}}{\left\|\mathbf{M}_{n+1} - \mathbf{M}_{n-1}\right\|}. \end{aligned}, \tag{2.29}$$

where ∇E_n is the gradient of energy for image n associated with magnetization state $\mathbf{M}_n$, ξ is an integration parameter and $\mathbf{t}_n$ is the unit tangent vector to the energy path.

Figure 2.10 shows an example of the minimal energy path for perpendicular magnetic tunnel junction (p-MTJ). The initial energy path shows the uniform switching of the magnetization.

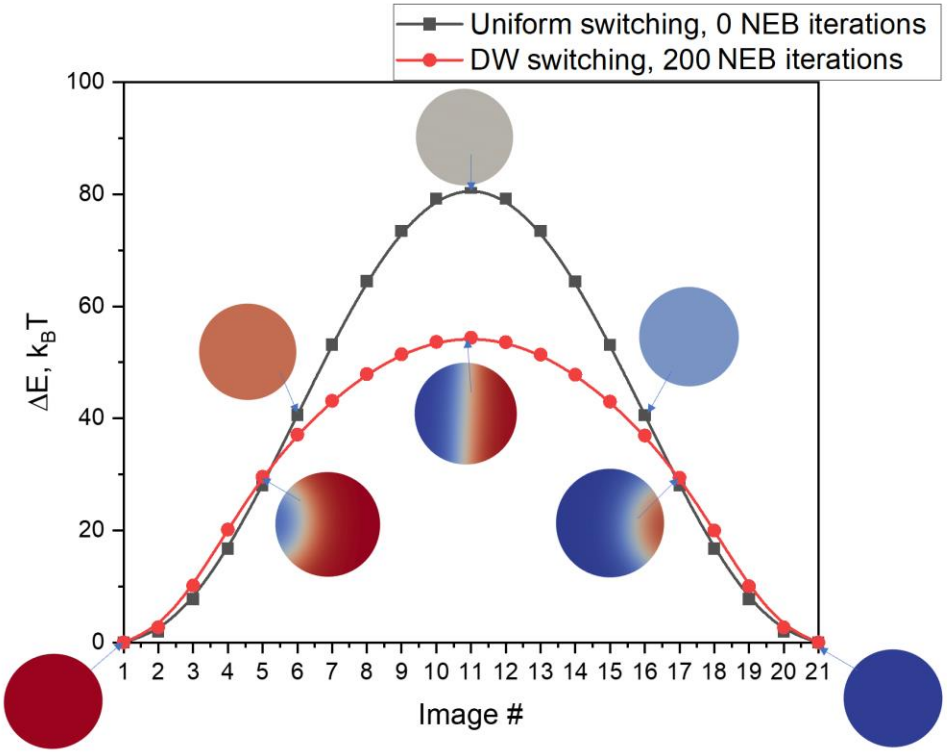

Figure 2.10: Minimal energy path of a single magnetic layer with diameter $D = 40\,\text{nm}$ and thickness $t = 1.2\,\text{nm}$, $M_s = 1200\,\text{emu/cm}^3$, $K_u = 9.06\,\text{Merg/cm}^3$, $A_{ex} = 10^{-6}$ erg/cm, $\alpha = 0.008$. The initial energy path is a uniform switching and the minimal energy path found using NEB method is a domain wall.

The insets of Figure 2.10 show the images of the magnetic configurations along the switching trajectory. After 200 NEB iterations, the minimum energy path was found. The energy barrier is almost twice as smaller than the uniform magnetization switching. In this case, the domain wall (DW) switching is more energy-efficient than uniform switching.

2.6 Thermal effects and the stochastic LLG equation

In real-world the magnetic devices typically operate at a room or specific chip temperature. The thermal excitation introduces a certain amount of disorder in the lattice of

magnetic structure. It means that the simulations of the magnetic devices must consider the thermal effects to be able to accurately evaluate the performance and reliability of the devices.

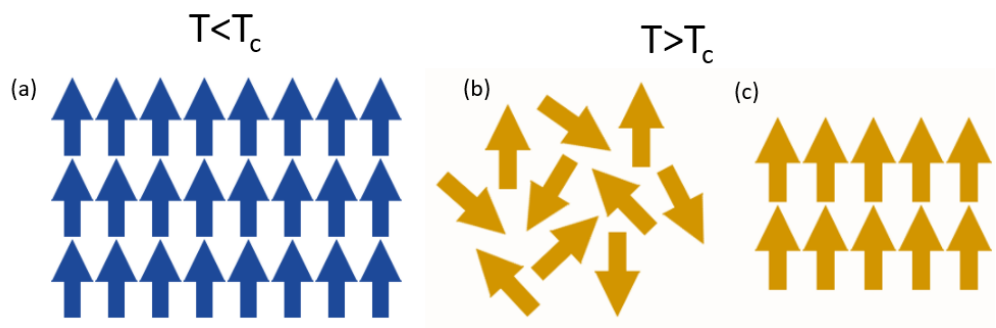

Figure 2.11: Illustration of the behavior of the magnetic moments above and under the Curie temperature: (a) below the Curie temperature the magnetic moments align parallel to each other in ferromagnet in the absence of an external magnetic field, (b) above the Curie temperature the magnetic moments are randomly oriented in a paramagnet unless (c) a magnetic field is applied.

When an external field is applied to a magnetic system, the magnetic moments tend to align with its direction to minimize their energy. The thermal excitation induces a distribution of the magnetic moments around this energy minimum and that distribution increases with the temperature. When the magnetic disorder is high, the moments are oriented in random directions to some degree and compensating each other, reducing the total macroscopic moment. The temperature at which certain materials lose their magnetic propertiesn due to this disorder is referred to as Curie temperature, T_C. For $T < T_C$ we can write:

$$M \sim \left(T - T_C\right)^{\beta}, \tag{2.30}$$

where M is the spontaneous magnetization, T is the temperature and β is the parameter that depends on the type of the material. The magnetic susceptibility χ of a material is a

measure of how much a material become magnetized per an applied magnetic field $\mathbf{H}$ and it is defined as:

$$\mathbf{M} = \chi \mathbf{H} . \tag{2.31}$$

The magnetic susceptibility for $T < T_C$ is described by the Curie-Weiss law as:

$$\chi = \frac{C}{T - T_C}, \tag{2.32}$$

where C is the Curie constant. The Curie temperature imposes some restriction on the material that can be used for data storage purposes. The considered materials must have a reasonably high Curie temperature to prevent their demagnetization and be stable at a room thermally at a room temperature.

The LLG equation (2.1) is fully deterministic, i.e., the magnetization dynamics calculated by it only depends on the magnetic fields described in previous sections 2.1 and 2.2 of this chapter. The LLG equation (2.1) describes the behavior of the system without any temperature, i.e., for $T = 0\text{K}$. For many devices this kind of modeling is not satisfying since some processes related to the magnetization dynamics strongly depend on the temperature, such as the magnetization reversal in magnetic random-access memories. To accurately represent the influence of the temperature it is necessary to adapt (2.1) and add the stochastic thermal field $\mathbf{H}_{thermal}$. The purpose of $\mathbf{H}_{thermal}$ is to account for stochastic (thermal) excitations. In micromagnetic modeling, the thermal field typically is represented in the form of a Gaussian noise that has a random value at each mesh node. The amplitude of the thermal noise must be adapted to the time-step used by the solver and is calculated using the fluctuation-dissipation theorem [28]. The thermal field at each node can be expressed as [11,29]:

$$\mathbf{H}_{thermal} = \sqrt{\frac{2\alpha k_B T}{\gamma M_s \left(1+\alpha^2\right) V dt}} \mathbf{\Gamma}, \tag{2.33}$$

where $\mathbf{\Gamma}$ is the random Gaussian noise vector, α is the damping constant, k_B is the Boltzmann constant and T is the temperature, γ is the gyromagnetic ratio, M_s is the saturation magnetization, V is the effective volume of the node and dt is a time step.

where $\mathbf{\Gamma}$ is the random Gaussian noise vector, α is the damping constant, k_B is the Boltzmann constant and T is the temperature, γ is the gyromagnetic ratio, M_s is the saturation magnetization, V is the effective volume of the node, and dt is the time step.

The LLG equation (2.4) is then updated with an additional thermal field as $\mathbf{H}_{thermal}$ as:The LLG equation (2.4) could be rewritten with an additional thermal field as $\mathbf{H}_{thermal}$ as:

$$\frac{d\mathbf{M}}{dt} = -\frac{\gamma}{1+\alpha^2}\mathbf{M}\times\left(\mathbf{H}_{eff}+\mathbf{H}_{thermal}\right) - \frac{\gamma\alpha}{1+\alpha^2}\mathbf{M}\times\mathbf{M}\times\left(\mathbf{H}_{eff}+\mathbf{H}_{thermal}\right). \tag{2.34}$$

Equation (2.31) can be used to simulate the behavior of systems at temperatures significantly lower than the Curie temperature. Closer to the Curie temperature, the reduction of the total spontaneous magnetization becomes significant, and the model is not able to accurately take this effect into account because we assume that the magnitudes of all magnetic moments are constant. The Landau-Lifshitz-Bloch (LLB) equation can be used instead of the LLG equation [30].

Chapter 3

Spin-transfer torque driven devices

Spin-transfer torque (STT) driven devices that use the spin of the electron are considered a promising candidate to revolutionize the electronics industry [31-33]. The main advantage and key significance of the spintronics devices is fast memory and a low power consumption at low electron density. The end of the last century was considered as an era of microelectronics. The rapid growth of microelectronics became a major threat to Moore's law making the spintronics devices as a possible solution. Most electronic devices have employed circuits that express data represented by the existence or absence of electric charge. Unlike microelectronics, spintronics exploits spin up and spin down of the electron to carry information. In 2007 A. Fert and P. Grünberg received Nobel Prize in Physics for discovery of the Giant Magnetoresistance (GMR) effect which led to the development of the spintronics devices [34,35]. Nowadays, the most promising spintronic devices are based on magnetic tunnel junction based on effect of tunnel magnetoresistance (TMR). This chapter discusses the magnetic memory and spintronic devices that utilize STT.

3.1 Magnetic memory

The first idea of magnetic memory was proposed in the 1950. Magnetic core memory was widely used for almost 20 years until the advent of the semiconductor memory. One of the first magnetic core memory was using small ferrimagnetic rings connected with wires for the information reading and writing (Figure 3.1 (a)). Ferrimagnetic rings were magnetized either clockwise or anti-clockwise regarding the axis of rotation going through them. The magnetic core can take two magnetization states associated with 0 or 1. The magnetic material for a magnetic core memory is highly magnetized and has low coercivity so that less energy is required to change the magnetization direction. This type of memory was one of the first non-volatile methods for information storage. In 1969, a magnetic bubble-memory was proposed by A. Bobeck [36].

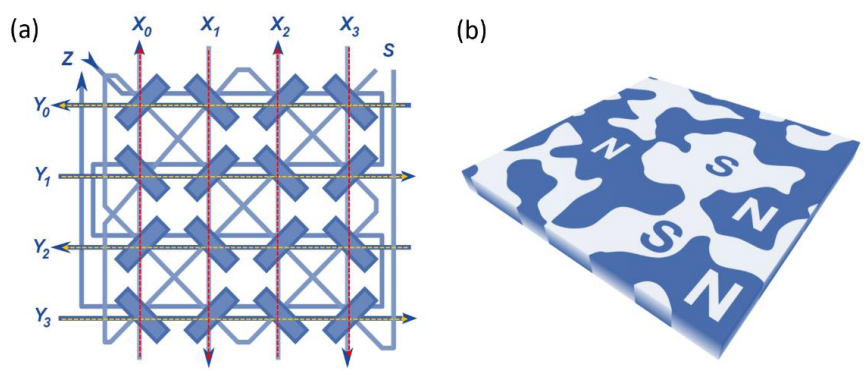

Figure 3.1: Illustration of the first magnetic memory: (a) magnetic core memory represented by an array of 4x4 toroids with X, Y as the drive lines, S is the sense and Z is the inhibit, (b) magnetic bubble-memory.

Magnetic bubble memory is a non-volatile type of memory that uses a thin film of the magnetic material to hold small magnetized areas (Figure 3.1. (b)), known as magnetic memory-bubbles, and it stores one bit of data per each area. The bubbles formed by a

generator were pushed through the film by an external applied magnetic field and detected by a magnetic sensor [37]. However, the introduction of dramatically faster metal–oxide–semiconductor memory chips made the magnetic bubble memories non-compatitive.

Nowadays, magnetic memory technology is represented by magnetoresistive random access memory (MRAM), spin transfer torque MRAM (STT-MRAM), and spin-orbit torque MRAM (SOT-MRAM).

3.2 Spintronic devices

Currently, most of the existing spintronic devices [38] are based on metallic systems called magnetic tunnel junctions (MTJs) and single electron transistor [39]. The working principle of a spintronic device follows the following steps: information is stored into spins-up or spins-down, spin information is carried by mobile electrons along a path or wire and, finally, the information is read at a final point. Figure 3.2 shows the basic representation of a spintronic device.

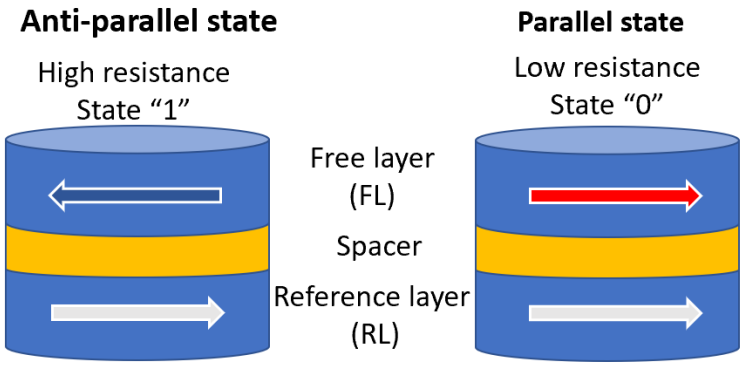

Figure 3.2: Schematic illustration of a magnetic pillar in a high resistance anti-parallel state and low resistance parallel state.

The basic element of a spintronic device is a sandwich of two magnetic layers separated by a non-magnetic conducting spacer layer or a thin insulating layer. While the magnetization of the reference layer (RL) is mostly fixed, the magnetization direction of the free layer (FL) can be switched between the two states parallel and anti-parallel to the fixed magnetization direction. Anti-parallel and parallel states possess different magnetoresistances which are mapped to 0 and 1 as shown in Figure 3.2. The most basic method of creating a spin-polarized current is to transport current through a ferromagnetic material and to transmit the electron spin carrying the information to the receiver point. Spin current is therefore an important tool to detect spin in spintronic devices. The development of spintronics devices can be divided in three main parts: the fabrication of nanoscale nanostructures and research of magnetic materials, the research of spin injection, spin transport and detection and, finally, the demonstration of spintronic devices including GMR, tunnel magnetoresistance (TMR) in magnetic tunnel junctions (MTJs).

3.3 Magnetoresistance phenomenon

The two most important magnetoresistance phenomena are the giant magnetic resistance (GMR) and the tunnel magnetoresistance (TMR) effects.

3.3.1 Giant magnetoresistance

In late 1980s M. Baibich and G. Binasch independently observed GMR effect in Fe/Cr superlattices [35,40]. GMR is a quantum mechanical effect detected in a pillar consisting of two ferromagnetic layers separated by a non-magnetic conducting spacer

layer. The low or high resistance state of the pillar depends on the layer's magnetization direction relative to each other.

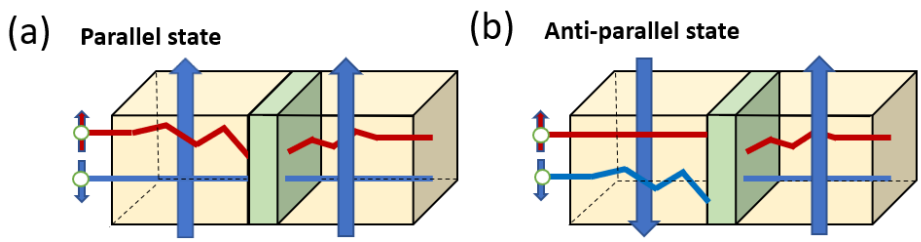

Figure 3.3: Illustration of giant magnetoresistance effect in its simplest interpretation.

GMR effect can be quantified with the following ratio [41]:

$$GMR = \frac{R_{AP} - R_P}{R_P} = \frac{\rho_{AP} - \rho_P}{\rho_P} = \frac{\sigma_P}{\sigma_{AP}} - 1, \tag{3.1}$$

where R_{AP} and R_P are the resistances, ρ_{AP} and ρ_P are the resistivities, σ_P and σ_{AP} are the conductivities for the parallel (low resistance) and anti-parallel (high resistance) states. Equation 3.1 shows that $GMR > 1$ if $\rho_{AP} > \rho_P$. An alternative equation for $GMR < 1$ can be written as:

$$GMR = \frac{R_{AP} - R_P}{R_{AP}} = \frac{\rho_{AP} - \rho_P}{\rho_{AP}} = 1 - \frac{\sigma_{AP}}{\sigma_P}. \tag{3.2}$$

To explain the effect of the GMR the model of two independent channels of conductivity for electrons with "spin-up" and "spin-down" orientations [42] was developed.

The total current is the sum of the current carriers with “spin-up” and the current carriers with “spin-down”. If both currents are flowing through the ferromagnetic layer with a fixed direction of magnetization (“up” or “down”), the resistance of the first and second groups of electrons differs. The GMR can be explained in terms of the unequal scattering of the two groups of electrons with different spin orientations with respect to the magnetization direction of the ferromagnetic layer (Figure 3.3). If the magnetization directions of the ferromagnetic layers are parallel to each other the “spin-down” electrons can propagate through the structure nearly unscaterred (Figure 3.3 (a)). This results in high electron conductivity and hence a low resistance. In contrast, in the anti-parallel state both “spin-up” and “spin-down” electrons undergo collisions in ferromagnetic layers, leading to a high resistance [43] (Figure 3.3 (b)). The GMR technology was adopted for hard disk drive read heads and stimulated the new phase of research in magnetic memories, such as GMR-based magnetic random-access memory [44].

3.3.2 Tunnel magnetoresistance

The phenomena of the tunnel magnetoresistance (TMR) was discovered in Fe/Ge/Co junction in 1975 [45]. TMR can be detected in a pillar consisting of two ferromagnetic layers separated by a thin insulating layer, i.e. magnetic tunnel junction (MTJ). Similarly, to the GMR effect, the resistance of the magnetic pillar depends on the magnetization direction layers with respect to each other. To quantify the TMR effect the following ratio can be used [46]:

$$TMR = \frac{R_{AP} - R_P}{R_P} . \tag{3.3}$$

Here, R_{AP} and R_P are resistances in the high resistance state and the low resistance state, respectively. In [45] the TMR effect was explained in terms of the polarization of the ferromagnetic electrodes and the spin polarization P calculated from the spin dependent density of states D at the Fermi energy:

$$P = \frac{D_{\uparrow}\left(E_F\right) - D_{\downarrow}\left(E_F\right)}{D_{\uparrow}\left(E_F\right) + D_{\downarrow}\left(E_F\right)}, \tag{3.4}$$

The spin-up electrons have spin orientation parallel to the external magnetic field, whereas the spin-down electrons have anti-parallel alignment with the external field. The relative resistance change can be written as:

$$TMR = \frac{2P_1P_2}{1 - P_1P_2}. \tag{3.5}$$

The simplest interpretation of the TMR effect can be done as shown in Figure 3.4. The spin-up or spin-down electrons can tunnel from one ferromagnetic layer to another ferromagnetic layer through a non-conductive thin insulating layer if there are available free states with the same spin orientation. In case of the parallel state, the majority spin-up electrons and minority spin-down electrons can easily tunnel to the second ferromagnetic layer and fill majority “up” and minority “down” states, respectively. This results in the large conductance and corresponds to the low resistive state as show on Figure 3.4 (a). In case of the anti-parallel state (Figure 3.4 (b)), the majority spin-down electrons and minority spin spin-up electrons from first ferromagnetic layer fill the minority “down” and majority “up” states in the second ferromagnetic layer, respectively. This results in the low conductance and corresponds to the high resistive state.

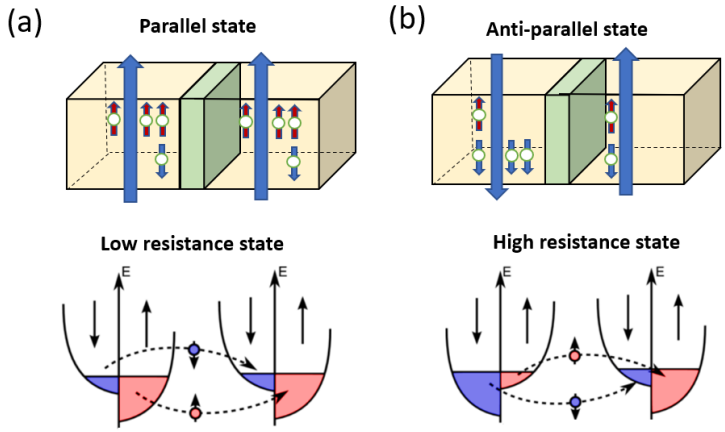

Figure 3.4: Illustration of tunnel magnetoresistance effect. (a) Parallel low resistance state, (b) Anti-parallel high resistance state.

Even though the TMR effect was demonstrated earlier than GMR effect, its usage in memory technology was not possible because of initially low TMR ratio. The development of the structures with Al_2O_3 tunnel barriers led to the development of TMR-based magnetic memory [47,48]. The next breakthrough in the development of magnetic memory was the discovery of a giant TMR in an epitaxially grown MTJ with MgO barrier. In 2001 a giant TMR in an MTJ with MgO barrier was independently predicted by [49,50]. The first experimental observation of TMR in Fe/MgO/FeCo single-crystal epitaxial junctions was made by [51]. In 2004 [52] and [53] demonstrated TMR in single-crystal Fe/MgO/Fe MTJs up to 220% and 180% at room temperature, respectively. In 2006 the giant TMR effects were observed junctions of Ta/$Co_{20}Fe_{60}B_{20}$/MgO/$Co_{20}Fe_{60}B_{20}$/Ta by [54].

3.3.3 Magnetic nanopillar switching

In conventional field-driven MRAM the free layer magnetization switching is done by applying an external magnetic field (Figure 3.5 (a)). The writing process is carried out by the current flowing through the wires and generating the magnetic fields around the

wires. Switching of the nanopillar only occurs when the magnetic fields from both currents are present at the magnetic nanopillar. This protects the magnetic cells disposed along one of the wires from spontaneous switching. Because the current required for generating the magnetic field for the switching increases when the wire cross-section decreases, it leads to the problem of scaling of the MRAM cells. Therefore, field-driven MRAM cells exhibit a scalability limit of about 90 nm [55].

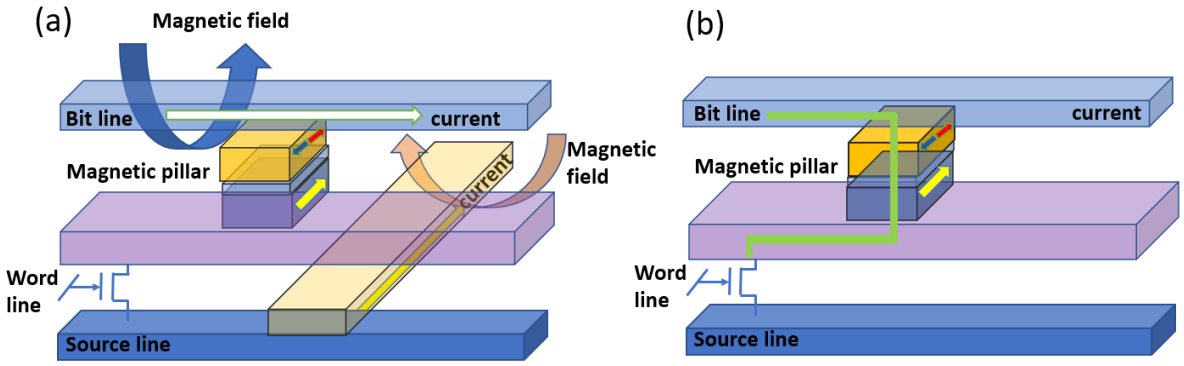

Figure 3.5: Schematic illustration of magnetic pillar switching: (a) field-driven MRAM switching, (b) STT-MRAM switching.

In conventional spin-transfer torque MRAM (STT-MRAM) switching between the two states occurs due to the spin transfer torque produced by the spin-polarized current flowing through the pillar (Figure 3.5 (b)). In contrast to field-induced MRAM the STT-MRAM does not require an external magnetic field for the switching. The theoretical prediction of the spin transfer torque effect was made independently by Slonczewski [18] and Berger [19] as discussed in Chapter 2. When electrons pass through the thick fixed magnetic layer, the spins of the electrons become aligned with the magnetization of this layer. When these spin-polarized electrons enter the free layer, their spin orientations get aligned with the magnetization of the free layer within a transition layer. Because of the

spin orientation change in the free layer the spins exert torque on the magnetization of the free layer. The magnetization of the free layer can switch if the torque is large enough to overcome the magnetic damping. For relatively smaller torques the magnetization vector of the free layer can precess around the vector of the effective magnetic field. The variation of the current polarity can lead to switching of the magnetization of the free layer from the anti-parallel to the parallel state and back with respect to the reference layer. In contrast to field-induced MRAM the scalability is not a major issue for the STT-MRAM cell because the reduction of the size of the cell leads to a decrease of the critical switching current [55].

3.4 Magnetic tunnel junction

Most of the existing spintronic devices are based on metallic systems such as magnetic tunnel junctions (MTJs). A magnetic tunnel junction (MTJ) can be considered as a spintronic device since it is composed of two ferromagnetic materials, such as Ni, Co or Fe, separated by an ultrathin layer of insulator with a thickness of the order of nanometres. The schematic of a magnetic tunnel junction (MTJ) is given in Figure 3.6.

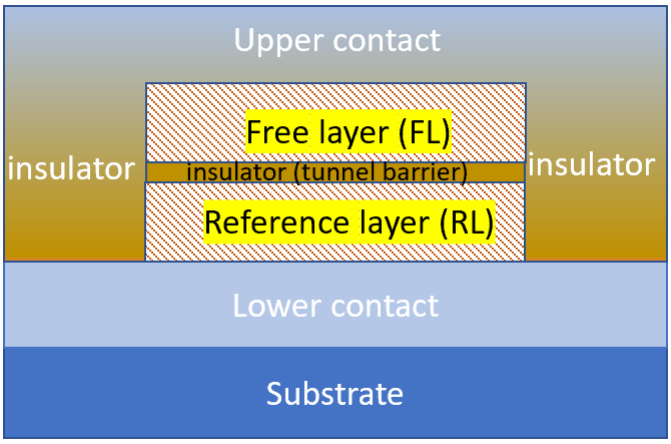

Figure 3.6: Schematic representation of magnetic tunnel junction (MTJ).

The MTJ stores the binary memory values as the magnetization direction of the free layer. The magnetization of the reference layer mostly is fixed. The MTJ is a TMR-based spintronic device, i.e., its electric resistance is larger when the magnetizations of the two ferromagnetic layers are antiparallel (state “0”) and lower when the two magnetizations are parallel (state “1”). An important factor in MTJ’s TMR is the interaction between the electron spin and angular momentum know as spin orbit coupling. An example of spin orbit coupling is splitting of hydrogen spectrum. The spin orbit coupling deforms the electron shell as the direction of the magnetization rotates. This deformation also changes the amount of scattering undergone by the conduction electrons when traversing the lattice. There is the minimal resistance if the magnetizations are in parallel orientation, and it is maximal with opposite orientations. Therefore, this junction can be switched between two states of electrical resistance.

3.4.1 In-plane and perpendicular magnetic anisotropy

The primary mechanism of STT switching can be illustrated with the typical one transistor one MTJ STT-MRAM cell shown in Figure 3.7 (a), where the write operation is performed by changing the polarity of charge current passing through the MTJ selected by bit and word line. The writing current can be spin polarized by the reference layer, transfer its spin angular momentum to free layer magnetic moment, and eventually reorient it by induced torque. Depending on the orientation of the layer magnetizations the magnetic pillars can be divided into two categories (Figure 3.7 (b)): “perpendicular” with out-of-plane magnetization direction and “in-plane” with magnetization lying in the plane of the magnetic layer.

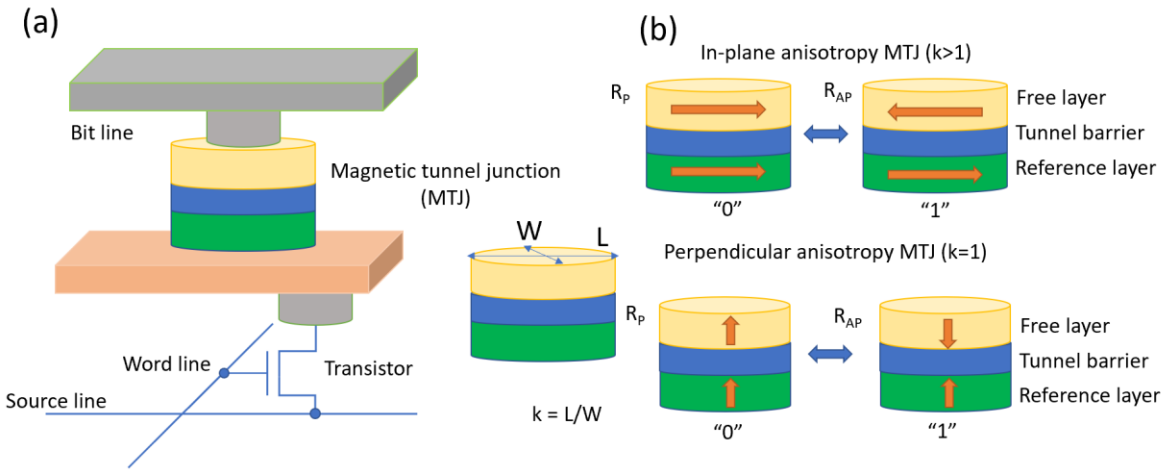

Figure 3.7: MTJ with in-plane and perpendicular anisotropy. (a) One transistor one magnetic tunnel junction (MTJ) cell using mechanism of spin transfer switching, where the MTJ is selected by word line and transistor operated by bit line. (b) Comparison between in-plane and perpendicular anisotropy based MTJ nano-pillar.

Compared with the in-plane magnetic anisotropy based MTJ, whose energy barrier originates from an asymmetric ellipse shape, perpendicular magnetic anisotropy (PMA) based MTJ depends on the interfacial atom arrangement (Figure 3.7 (b)). The switching current density of MTJ with PMA is lower. PMA based MTJ is envisioned as a promising candidate to realize high-density memories. Additionally, the write and read speed of PMA based MTJ should be minimized to further enable the replacement of static random access memory (SRAM) and embedded dynamic RAM (eDRAM) [56]. It is worth noting that the switching speed is determined by the amplitude of writing current rather than the orientation of the magnetization, because the switching mode transits from being precessional to thermal fluctuation assisted by STT along with extended pulse duration, further indicating the importance to pursue lower switching current density.

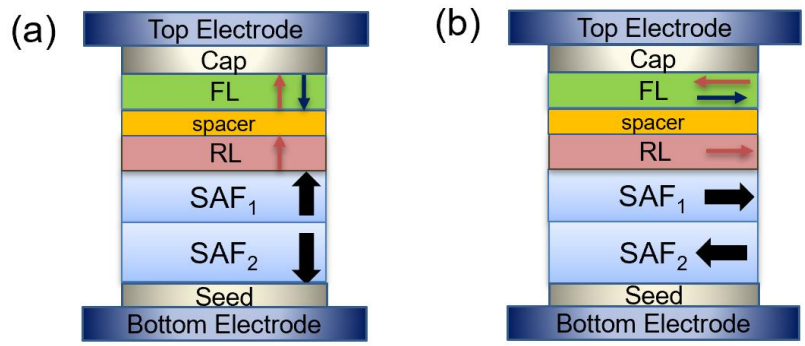

Figure 3.8: (a) All-perpendicular and (b) in-plane MTJ MRAM element consisting of: bottom electrode, seed layer, antiferromagnetic layers, reference layer, tunnel barrier, free layer, capping layer and top electrode.

3.4.2 Thermal stability of in-plane and perpendicular MTJs

Thermal stability is one of the key parameters when designing STT-based devices such as MRAM. The thermal stability factor is defined as the ratio of the thermal stability barrier to the operating temperature [57]:

$$\Delta = \frac{E_b}{k_B T}, \tag{3.6}$$

where E_b is the energy barrier between parallel and antiparallel magnetization alignments, k_B is the Boltzmann constant and T is the temperature. The energy barrier E_b is defined as [57]:

$$E_b = \frac{M_s H_k V}{2}, \tag{3.7}$$

where M_s is the saturation magnetization, H_k is the anisotropy field and V is the volume of the free layer. The thermal stability factor for out-of-plane or perpendicular MTJ MRAM (p-MTJ) (Figure 3.8 (a)) is given by the interface-induced perpendicular anisotropy field H_k^{OOP} [58,59]:

$$H_k = H_k^{OOP} - 4\pi M_s \,, \tag{3.8}$$

and the correspondent thermal stability factor for p-MTJ MRAM could be written as:

$$\Delta^{OOP} = \frac{M_s \left(H_k^{OOP} - 4\pi M_s \right) V}{2k_B T} \,, \tag{3.9}$$

For the case of in-plane MTJ MRAM (Figure 3.8 (b)) the thermal stability factor is determined by the shape anisotropy field $H_k = H_k^{IP}$ and can be represented as [58,59]:

$$\Delta^{IP} = \frac{M_s H_k^{IP} V}{2k_B T} \,. \tag{3.10}$$

To change the thermal stability factor, it is sufficient to change the geometrical sizes of the free layer or modify its material parameters. For example, to increase the thermal stability we can increase the thickness of the free layer and/or the aspect ratio between principal axes defining the elliptical cross-section. The general analytical expression provided in this section will be working well for a single free layer with uniform or domain wall switching. However sometimes it is hard to predict the non-uniform or bubble-like magnetization switching energy path that typically takes place for the MTJ MRAM > 120 nm [60]. As shown in section 2.5, NEB method can be an efficient method to compute energy barriers for p-MTJ. Micromagnetic modeling and analysis of NEB for p-MTJ MRAM will be discussed in detail in the next chapters of this work.

3.4.3 Critical switching current and efficiency

The critical switching current I_{C0} is the current that is needed for switching of the free layer from one of its equilibrium states to the other equilibrium state. Another important parameter is the critical switching current density $J_{C0} = I_{C0}/A$, where A is the cross-section area of the free layer. The spin-polarized current is only a fraction of the total charge current flowing through the device. Therefore, high current densities from 10^7 - 10^8 $\mathrm{A/cm^2}$ are typically required to switch the magnetization direction of the free layer. The reduction of the critical switching current density for magnetization switching is one of the most important challenge for the STT-MRAM devices development. Achieving low switching current densities is not only important to decrease power consumption, but also to ensure device durability, and to maximize efficiency and density. The analytical expression for the critical writing current of the free layer in an in-plane MRAM MTJ memory element in the macrospin approximation at $T = 0\,\mathrm{K}$ is [59]:

$$I_{C0}^{IP} = \frac{2\alpha e}{\hbar \eta(\theta)\, p} M_s V \left(H_k^{IP} + 2\pi M_s \right), \tag{3.11}$$

where H_k^{IP} is the in-plane magnetocrystalline anisotropy field, $\hbar$ is the reduced Planck constant, e is the fundamental charge, α is the damping constant, V is the volume of the free layer, p is current polarization, M_s is the saturation magnetization, $\eta(\theta)$ is the angular dependence of the STT efficiency. From equation 3.11 can see that reducing α and increasing the $\eta(\theta)\, p$ product results in reduced I_{C0}^{IP}, suggesting that materials engineering will play a major role in making STT MRAM a viable storage solution at high bit densities. From equation 3.7 write $E_b = M_s H_k^{IP} V/2$, which, for thermal stability requirements has to

satisfy the condition $E_b \geq 60\,\mathrm{k_B T}$. The shape anisotropy field $2\pi M_s$, be partially balanced by an out-of-plane anisotropy contribution H_k^{OOP}. For p-MTJ MRAM the critical current can be written as [59]:

$$I_{C0}^{OOP} = \frac{2\alpha e}{\hbar \eta(\theta)\, p} M_s V \left(H_k^{IP} + 2\pi M_s - \frac{H_k^{OOP}}{2} \right). \tag{3.12}$$

The equation 3.12 shows that for p-MTJ MRAM the critical switching current $T = 0\,\mathrm{K}$ can be reduced. The closer $2\pi M_s - H_k^{OOP}/2$ the lower I_{C0}^{OOP}. It has been shown in [61] that switching efficiency is better for perpendicular spin-valves. Indeed, when $H_k^{OOP} > 4\pi M_s$ and $H_k^{IP} = 0$ the magnetization goes out-of-plane. In this case the critical switching current can be written directly proportional to energy barrier:

$$I_{C0} = \frac{4\alpha e}{\hbar \eta(\theta)\, p} E_b\,. \tag{3.13}$$

where $E_b = M_s V \left(H_k^{OOP} - 4\pi M_s \right)/2 = M_s V H_k^{eff}/2$. Figure 3.9 shows the current-induced switching for a p-MTJ stack with diameter 20 nm with uniform rotation.

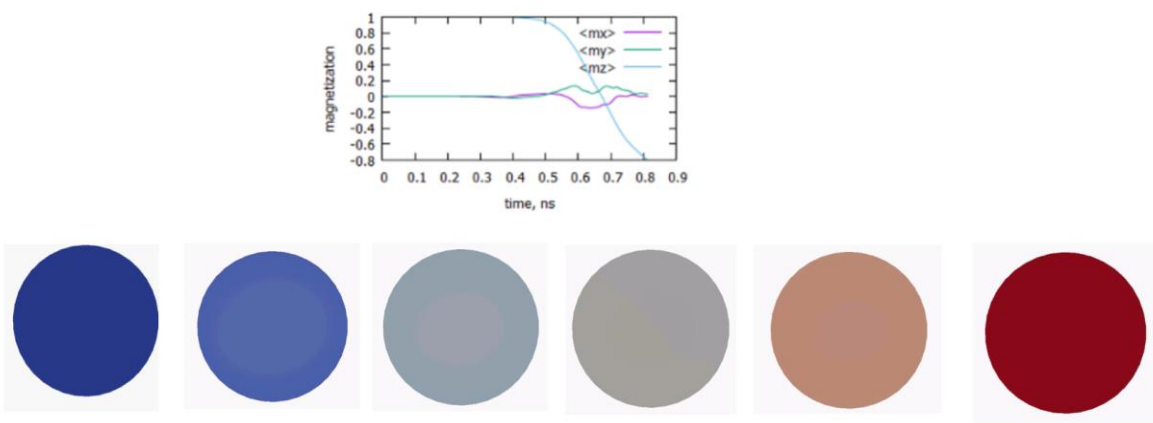

Figure 3.9: Illustration of p-MTJ MRAM switching by uniform rotation.

The equations 3.13 for the critical switching current of MTJs is proportional to the thermal stability factor and works well in macrospin approximation for $T = 0\,\mathrm{K}$. However, the equations 3.13 might not work for the case of the non-uniform magnetization dynamic during current induced switching.

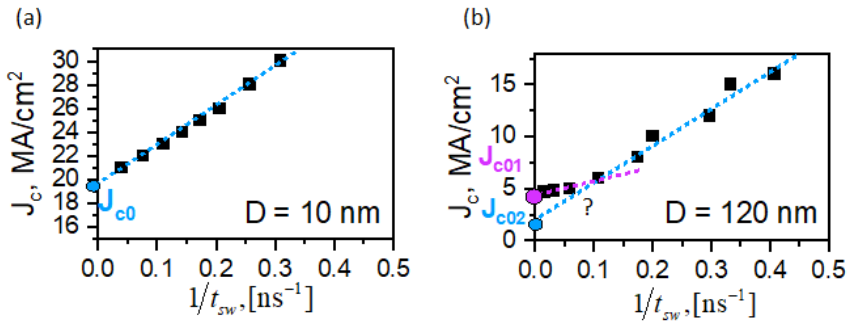

Figure 3.10: Numerical calculation of the critical switching current density for MTJ for infinite current pulse: (a) for the case of coherent magnetization switching and diameter 10 nm the critical switching current density could be easily interpolated (b) for the case of non-uniform magnetization switching and diameter 120 nm the infinite pulse interpolation method does not predict the reliable critical current density.

In order to calculate numerically the critical switching current density, the infinite pulse model is used [46]. Figure 3.10 shows the dependence of the switching current density as a function of the reverse switching time for p-MTJ with diameter 10 nm and 120 nm. For a small sizes, i.e., ~ 10 nm the magnetization switching is uniform, and the switching current density dependence is linear for the long enough switching pulses. However, for the larger sizes of p-MTJ (~ 120 nm) the switching current density has non-linear dependence for a long pulse (low current values) which leads to unreliable calculation of the critical switching current density due to non-uniform behavior. To overcome such a problem several approaches were developed including the eigen value solver or write error rate (WER) simulations (Figure 3.11). The write process in an STT-RAM bit is inherently stochastic due to thermal fluctuations, which give rise to a

distribution of the magnetization of the free layer both before and during switching. As a result, the time taken by the bit to switch has a wide distribution. Therefore, there is a non-zero probability that when a finite duration write pulse is turned off the bit is not written and a so-called write error takes place [62]. The probability that a write error takes place for a given applied current pulse of a given length is called the write error rate (WER). For correct operation of the STT-MRAM array, the WER needs to be less than 10^{-9} if there is an error correction circuit (ECC) in the chip. If there is no ECC the WER needs to be less than 10^{-19} [62] . As a result, accurate modeling of the low probability tail of the WER is critical. As shown in section 2.5, NEB can be an efficient method to compute energy barriers from which the thermal stability can be assessed. However, it is not enough to have the full picture. Indeed, the behavior of a device under the influence of a thermal fields depends not only on the shape of the energy landscape in the magnetic configuration space, but also on the type of reversal process involved. An example is shown in Figure 3.11.

We now consider the relationship between critical current densities, switching rates, switching probability, and temperature to better understand the path to low power consumption, high operating speeds, and reduced bit-error rates. Analytical models and experiments show that the average rate of switching τ_{ave} in perpendicular magnetic anisotropy nanopillars under spin-polarized currents under spin-polarized currents for short times [63,64]:

$$\tau_{ave}^{-1} = A\left(I - I_{C0}\right), \tag{3.14}$$

where I is the current and A is a coefficient. For long timescales, from first principles and Fokker-Planck calculations, the switching rate for thermally-assisted reversal under the influence of spin transfer torque is given by [63,64]:

$$\tau_{ave} = \tau_0 \exp\left[\left(1 - \frac{I}{I_{C0}}\right)\frac{E_b}{k_B T}\right], \tag{3.15}$$

Even if smaller switching times can be afforded for a given application, the switching current distributions due to MTJ nonuniformity and thermal fluctuations may impose a still high current requirement for reliable operation. Models for the probability of switching P in the short time scale regime give [17,63,64]:

$$P = \exp\left[-4\frac{E_b}{k_B T}\exp\left[2\frac{\tau}{\tau_d}\left(1 - \frac{I}{I_{C0}}\right)\right]\right], \tag{3.16}$$

and for long time scale:

$$P = 1 - \exp\left[-\frac{\tau}{\tau_0}\exp\left[-\left(1 - \frac{I}{I_{C0}}\right)\frac{E_b}{k_B T}\right]\right], \tag{3.17}$$

where τ is the current pulse duration, $\tau_d = \left(\alpha\gamma H_k\right)^{-1}$. Equations 3.16 and 3.17 illustrate the tradeoff between the switching probability, switching time, and write-current magnitude. The illustration of the switching probability for p-MTJ stack is shown on Figure 3.11. For 10x10 p-MTJ-stack the WER was calculated at $T = 300\,\mathrm{K}$ for different current pulse width. For longer pulses, the critical switching current density is smaller compared to the short pulses. This is because for very short current pulses much higher current density required to switch the device. For longer pulses the switching current density decreases and the WER curve is steeper compared to short current pulses.

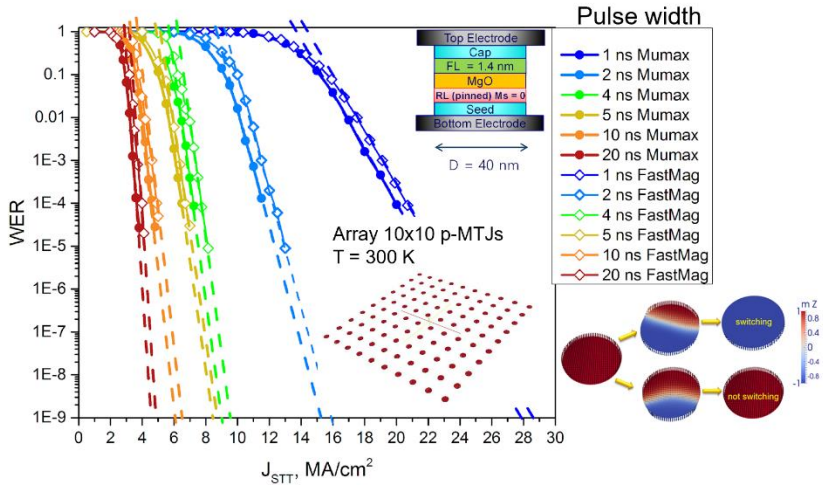

Figure 3.11: Illustration on write error rate (WER) simulations at $T = 300\text{K}$ for 10x10 array of p-MTJ's free layers for different pulse width and micromagnetic simulator software.

Another important parameter for the MTJ scaling is the device efficiency or figure of merit (FOM). FOM is useful for device characterization and its scalability and operation. The device efficiency could be defined as the ration between the energy barrier to the critical current density:

$$FOM = \frac{\Delta}{I_{C0}} \tag{3.18}$$

The detail study of the FOM in p-MTJ is provided in Chapter 4.

3.5 Spintronic devices based on MTJs

As we have already mentioned spin-transfer torque can be used to flip the active elements in magnetic random-access memory. Most of the spintronic devices (STT-MRAM or SOT-MRAM) utilize MTJs. Spin-transfer torque magnetic random-access memory (STT-MRAM) is a non-volatile type of memory with near-zero leakage power consumption, which is a major advantage over charge-based memories such as SRAM and

DRAM. STT-RAM also has advantages of lower power consumption and better scalability than MRAM using magnetic fields to flip the active elements. Spin-transfer torque technology has the potential to make possible MRAM devices combining low current requirements and reduced cost. However, the switching current may be too high for most commercial applications, and the reduction of this current density alone is a subject of active academic research. Recently, spin orbit torque magnetic random-access memory (SOT-MRAM) was proposed. Unlike the STT-MRAM, SOT-MRAM offers unique system-level value thanks to its unique combination of high working speed and endurance. Also, SOT-MRAM switching does not need to rely on thermal activation to initiate the switching, which makes reliable sub-ns switching with no delays. As a result, SOT-MRAM may be used as DRAM-like working memory or SRAM-like cache memory, which was impossible with STT-MRAM.

3.5.1 Spin-transfer torque MRAM

Spin-transfer magnetic random-access memory (STT-MRAM) is a non-volatile memory technology to replace the embedded flash at advanced technology nodes [65,66]. STT-MRAMs appear to be one of the most versatile and promising for a large range of applications, thanks to its combined set of performance. Figure 3.12 (a) shows the typical configuration of the STT-MRAM cell.

STT-MRAM is based on MTJs nanostructure composed of ferromagnetic layers separated by tunnel barrier. STT-MRAM is based on the manipulation of the spin of electrons with a polarizing current to establish the desired magnetic state of the free layer to

write the bits in the memory array. Electrical resistance depends on the magnetization orientations. In standard STT-MRAM the writing of the data is performed by passing a current through the MTJ and the written value depending on the direction of the current.

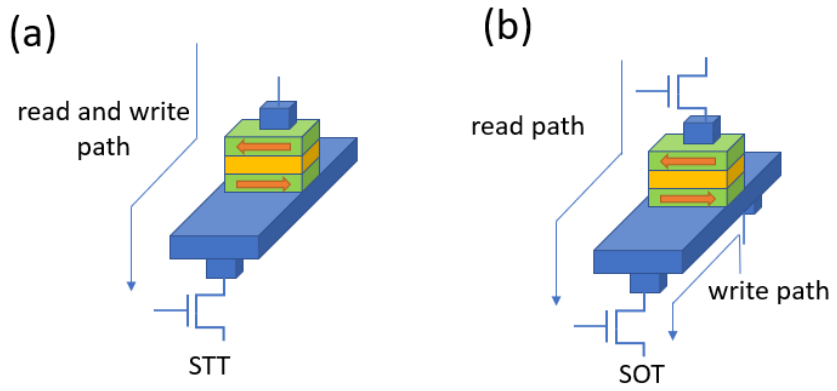

Figure 3.12: Magnetic tunnel junction-based spintronic devices. (a) STT-MRAM, (b) SOT-MRAM.

Non-volatility, zero standby leakage, high endurance, compatibility with fabrication process, scalability and high integration density of STT-MRAM created the path toward a universal memory.

3.5.2 Spin-orbit torque MRAM

Although the performance of STT-MRAM is much better than standard non-volatile technologies like flash, it suffers from limitations for high-speed applications. A new MRAM technology based on Spin-Orbit Torque (SOT) was recently discovered and it may offer better performance in terms of speed and endurance, at the expense of a slightly degraded density [67]. Figure 3.12 (b) shows the schematic representation of the SOT MRAM. SOT is based on spin-transfer effects, but unlike STT-MRAM there is no need for a magnetic layer to spin-polarize the electrical current. The source of spins is simply the

lattice of a SOT layer material via spin-orbit interaction. The SOT uses the same core MTJ as the existing STT and can thus be implemented in the same manufacturing environment as STT. SOT-MRAM does not require passing of a high current through the MTJ during the write operation. Writing is done by a lateral current flowing through an adjacent "SOT" metal line. Two physical phenomena are understood to be at the origin of the spin-orbit torques (SOT) (Figure 3.13): A bulk component, the Spin Hall Effect [68,69], and an interfacial component, commonly known as the Rashba Effect [70,71]. The Spin Hall effect induces a spin current transverse to the charge current flowing in the SOT layer, leading to a spin accumulation at the SOT interfaces, which then diffuses into magnetic materials. The Rashba effect originates from the uncompensated electric field at the interface, resulting in an effective magnetic field directly acting on the nearby magnetization. Both effects lead to magnetic torques, that can control the magnetization direction of an adjacent magnetic "storage" layer, to write a binary "0" or "1" in the MRAM cell.

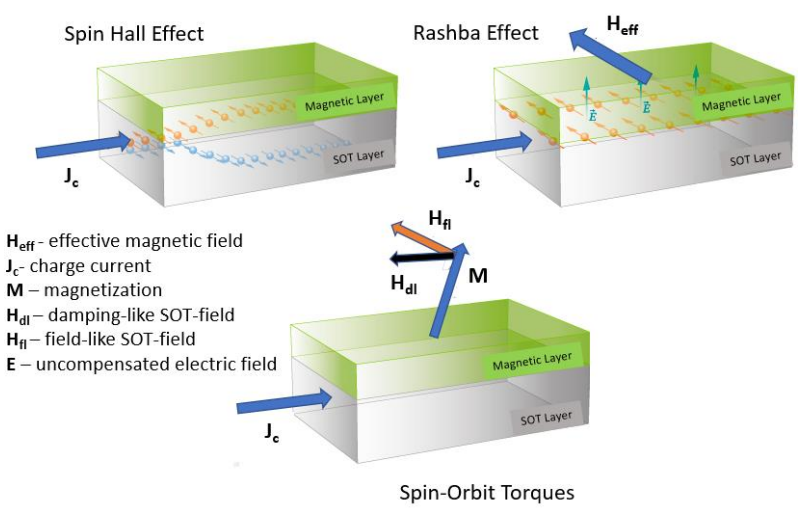

Figure 3.13: Illustration of spin-orbit torque.

3.6 Spin-transfer torque magnetic oscillators

Creating broadly tunable microwave and terahertz sources is an ongoing quest for numerous applications, such as high-resolution imaging, nuclear fusion plasma diagnosis, skin cancer screening, large-scale integrated circuit testing, wireless communication among others. STT can be used to achieve steady-state magnetization precession in nanoscale devices having MTJ-based geometry. Devices operating in such a steady-state regime are referred to as spin-torque oscillators (STO). STOs offer a number of attractive properties, including high-quality high-frequency microwave generation with broad frequency tunability [72-76], and they can be used for neuromorphic computing and GHz communications [77-79]. STOs can be also be used for microwave-assisted magnetic recording (MAMR) to assist the switching of high anisotropy bits [80]. Because the precession angle and amplitude of oscillations can be electrically detected by the GMR or TMR effects (sections 3.3.1 and 3.3.2), STOs can also be used in the response regime as sensor [72]. STOs tailored to operate in steady-state regime are of technological interest because the precessional frequency is in the GHz range and it can be easily tuned by current and field biases. The devices can operate over a wide range of temperatures and small nanoscale dimensions. It should be mentioned that several STOs can be coupled to each other by spin waves [81,82], or coupled to external electric current or microwave signals [72,83,84] to achieve diverse dynamical responses.

This section discusses several STO's types, including conventional STO with an applied field, and easy-axis STO, and antiferromagnetically exchange coupled STO.

3.6.1 Operation principle and device configuration

A simple STO uses a magnetic bilayer consisting of a free magnetic layer and a fixed magnetic layer that are separated by a thin non-magnetic spacer (Figure 3.14). The spin torque causes the magnetization vector of the free layer to precess by compensating the natural magnetic damping. The precession can be in a quasi-uniform mode [74], a spin-wave mode [83], or a magnetic-vortex mode [81]. The resulting microwave signal is detected as oscillations of the resistance across the bilayer, which result either from giant magnetoresistance (GMR) in the case of a metallic spacer, or from tunnelling magnetoresistance (TMR) in the case of an insulator spacer.

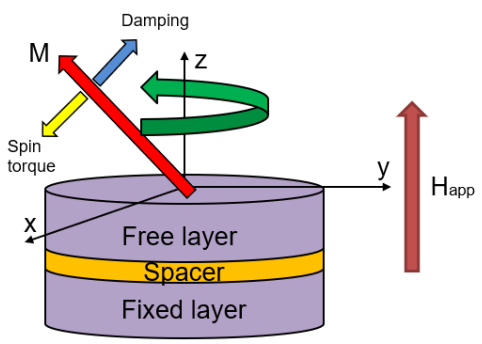

Figure 3.14: Geometry of a spin-torque oscillator consisting of a "fixed" magnetic layer, a nonmagnetic spacer and a "free" magnetic layer. The free layer magnetization, M (red arrow), precesses around the direction of an applied magnetic field (H_{app}) when natural magnetic damping (blue arrow) is compensated by the spin torque (yellow arrow) applied by a spin-polarized current flowing from the fixed layer.

Over the last ten years, numerous theoretical and experimental studies of STOs have been done. To date, several STO configurations have been explored, which can be classified by the type of spacer layer (showed in Figure 3.14), the patterning geometry, and the equilibrium magnetic configurations [85,86]. Two patterning geometries are used, one is to make "nanopillar" devices in which the free layer or both the free and the fixed layers are patterned to a desired cross section (Figure 3.15 (a)). The other geometry is to make

electric "point-contact" to an extended multilayer film (see Figure 3.15 (b)), referred as a nano-contact.

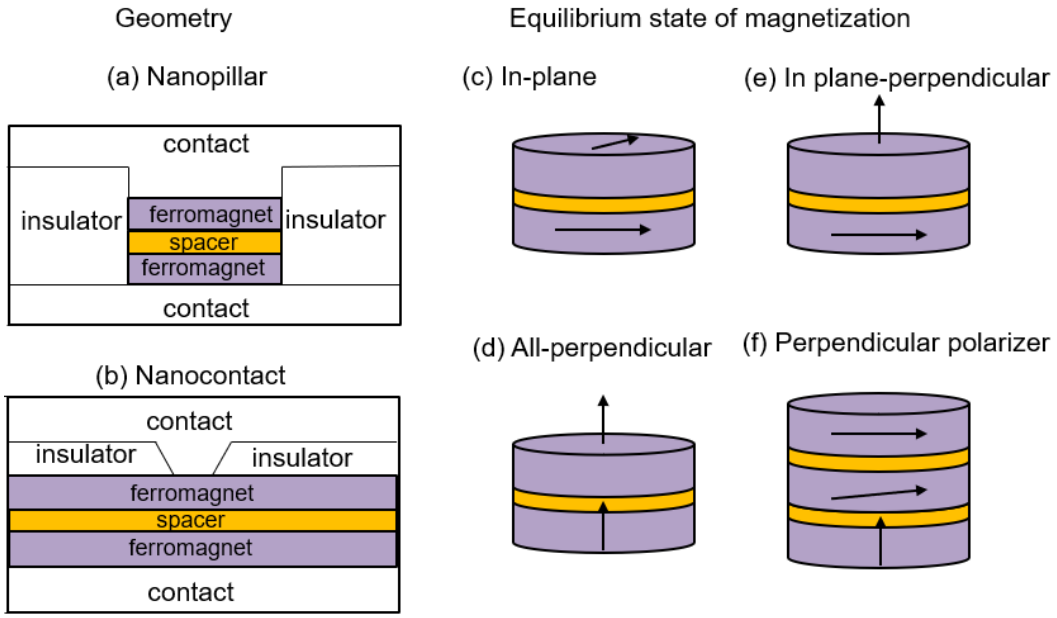

Figure 3.15: Different configurations of the spin-transfer oscillator based on geometry type and equilibrium magnetization state.

Another classification is based on the magnetization configuration. One example is an in-plane configuration, in which the magnetization orientations of the free and fixed layer are designed to have an in-plane configuration (see Figure 3.15 (c)) [87,88]. To produce a microwave signal this structure generally requires a large static magnetic field applied a few degrees away from the magnetically easy axis of the free layer. The second type is to make a "fully perpendicular" device in which both the free layer and polarizer are perpendicular to the sample plane as shown in Figure 3.15 (d). The relative magnetic configuration in this structure is similar to that of the in-plane one, thus also requiring an external bias to produce microwave signal. The third type is to combine the in-plane and out-of-plane magnetic configuration to build an in-plane-perpendicular device as shown in

Figure 3.15 (e). This latter solution is very promising being an efficient configuration to excite large angular free layer precession leading to a large output power, even in the absence of a bias magnetic field. Based on the above configurations, hybrid devices can also be designed, for example, Figure 3.15 (f) presents a structure that utilizes a perpendicular polarizer and a planar free layer combined with a read-out layer.

3.6.2 STOs with perpendicular polarizer

Conventional spin-transfer oscillator

The conventional STO is an MTJ-based memory device showed in Figure 3.14. This type of STO typically operates with an applied external magnetic field and current. The operation of STO under an applied current and external applied magnetic field can greatly vary depending on the current and field bias intensity and direction, size of the device, system geometry, configuration, materials choices, and ambient temperature. The geometry and material parameters determine the magnetic anisotropy direction and energy density of the STO. Those parameters also define the STT efficiency and its angular dependence as discussed in section 4.1.1.

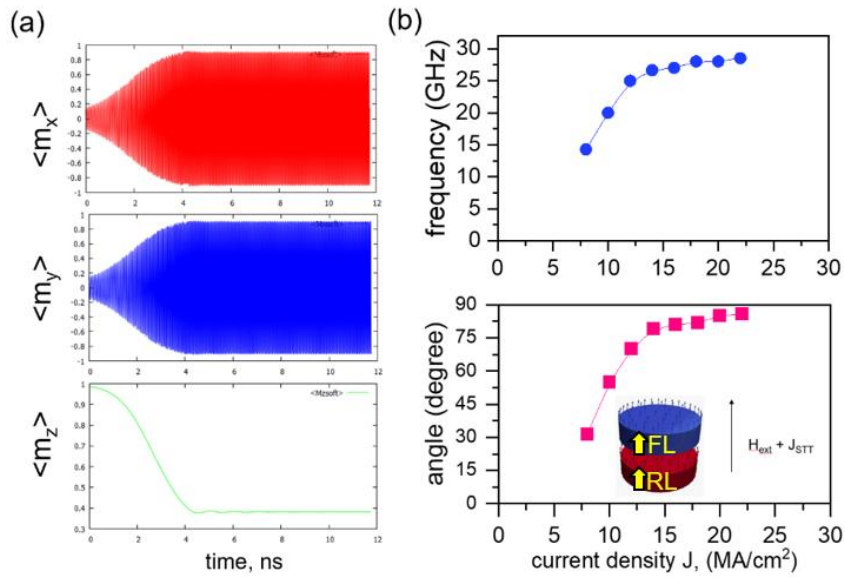

Figure 3.16: Micromagnetic simulations of perpendicular spin-torque oscillator subjected to applied current and external magnetic field: (a) magnetization components (b) precession frequency and angle. The applied magnetic field $H_{app} = 0.5\,\mathrm{T}$ and diameter $D = 40\,\mathrm{nm}$.

An illustration of STO operation is represented in Figure 3.16. We consider a simplified all-perpendicular STO stack consisting of a free layer and fixed perpendicular polarizer, subject to a current and a perpendicular to structure applied magnetic field (Figure 3.14). The reference layer acts as a spin filter that drives the free layer into a steady-state precession [73,76,89-93]. Additional layers are also introduced for fabrication and measurement, and to optimize material properties. Steady-state precession of the described STO is illustrated in Figure 3.16 (a). The precession frequency and corresponding angle are represented in Figure 3.16 (b). Analytically the spin-transfer torque on the free layer may be expressed as [17]:

$$\boldsymbol{\tau}_{STT} = \sigma\eta(\theta)\frac{1}{t_{FL}}\frac{\hbar}{2}\frac{J}{e}\mathbf{M}\times\mathbf{M}\times\hat{\mathbf{z}}, \tag{7.1}$$

where J is electric current density, t_{FL} is the thickness of free layer, $\sigma = \pm 1$ defines the magnetization orientation of the polarizing layer along $\hat{\mathbf{z}}$ and $\eta(\theta)$ is the angular dependence represented in section 4.1.1 [5]. The damping torque due to an applied external magnetic field can be written as [17]:

$$\boldsymbol{\tau}_{\alpha} = -\frac{\gamma\alpha}{1+\alpha^2}\mathbf{M}\times\mathbf{M}\times\mathbf{H}_{app}\,. \tag{7.2}$$

The steady-state precession of the free layer can be expected and magnetostatic effects are small compared to the influence of the external field (Figure 3.15 (a)). The steady-state precession is absent for specific combinations of device-dependent parameters and applied field magnitudes [17]. In Ref. [17] Figure 12.8 shows the curves indicating combinations of current and field amplitude and direction resulting in steady-state precession of a simplified all-perpendicular spin valve.

Easy-plane and easy-axis spin-torque oscillators

One of the qualities of STOs is that they are tunable over a wide frequency range by varying the applied DC current or magnetic field. However, STOs with a large microwave emission power and a narrow linewidth are of the most challenging issues to move the STOs to the practical applications. The output power is typically too weak for any practical applications. In order to improve the output power, several methods have been proposed, for example, using synchronization through the phase-locking mode of an array of STOs [72] or using MgO-based MTJs to replace the spin valves [94], which increase the output power to several μW level because of an increased magnetoresistance signal. However, most practical applications require these devices to operate in either zero or weak applied

magnetic fields. For that, one particularly promising STO device was proposed the uses a spin-torque nanopillar consisting of an out-of-plane (OP) magnetized spin polarizer and an in-plane (IP) magnetized free layer [88,95]. Another type of STOs uses CoFeB-MgO based MTJ that consists of an OP free layer and an IP spin polarizer, which shows large-power microwave oscillations in the absence of any external magnetic fields [96,97]. In these two types of STO geometries, the spin-polarizing layer is perpendicular to the free layer a large spin-torque can be initially generated, which results in a lower threshold current to drive the OP precession and a larger amplitude of the microwave signals.

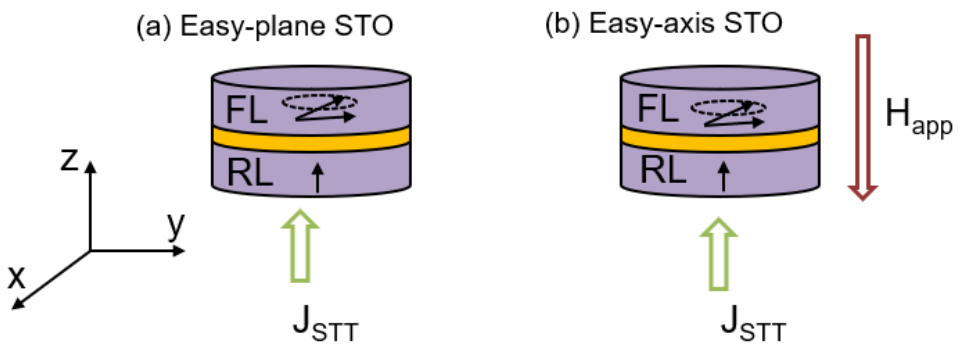

Figure 3.17: (a) easy-plane STO and (b) easy-axis STO.

Figure 3.17 presents two types of oscillators: easy-plane STO and easy-axis STO. The easy-plane STO can operate without an applied magnetic field. Figure 3.18 (a) shows the simulated oscillation frequency of free layer as a function of the applied current. When the current density increases from $0.0\ \mu A/nm^2$ to $0.04\ \mu A/nm^2$, the frequency varies from $0\,GHz$ to $8\,GHz$. We find that the frequency behavior strongly depends on the variation of the z-component of the averaged magnetization (Figure 3.18 (b)), showing that the frequency is related to the effective demagnetization field of the free layer [98]

$f = (\gamma/2\pi)4\pi M_s \langle m_z \rangle$. Since the maximum demagnetizing field occurs when the magnetization of the free layer is driven fully perpendicular, the maximum precession frequency would be $f_{\max} = 2\gamma M_s$. Simulations shown in Figure 3.18 (b) indicate that a flat plate at frequency of $8\,\text{GHz}$ is observed. We infer that this comes from the competition between the demagnetization field which prefers the in-plane magnetization and spin-transfer torque prefers +z magnetization direction at negative current. Figure 3.18 (c) shows the time-dependence of magnetization components of free layer. The precession angle free layer of the easy-plane STO is large for low currents and tends to decrease with increase of the perpendicular current.

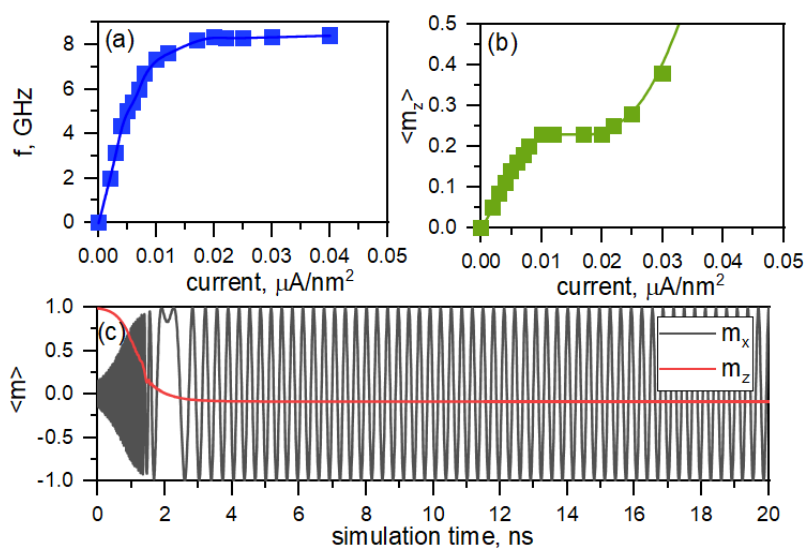

Figure 3.18: Micromagnetic simulations of easy-plane STO: (a) precession frequency (b) precession angle (c) m_z and m_x components for $J = 0.01\,\mu\text{A}/\text{nm}^2$. The thickness of free layer is $t_{FL} = 0.8\,\text{nm}$. For all simulations $M_s = 1350\,\text{emu}/\text{cm}^3$, $K_u = 1.11\,\text{Merg}/\text{cm}^3$, $\alpha = 0.008$, $A_{ex} = 10^{-6}\,\text{erg}/\text{cm}^2$ and diameter $D = 40\,\text{nm}$.

In order to compare the easy-plane STO with the easy-axis STO, Figure 3.17 (b) represents an easy-axis STO with applied external magnetic field H_{app}. When the current density increases from 0 to $0.1\,\mu\text{A}/\text{nm}^2$, the precessional frequency

of the free layer is non-linearly increasing up to saturation frequency $f = 10\,\text{GHz}$. The corresponding z-component (Figure 3.19 (b)) is decreasing because of the increase of the current making it to switch in the z-direction.

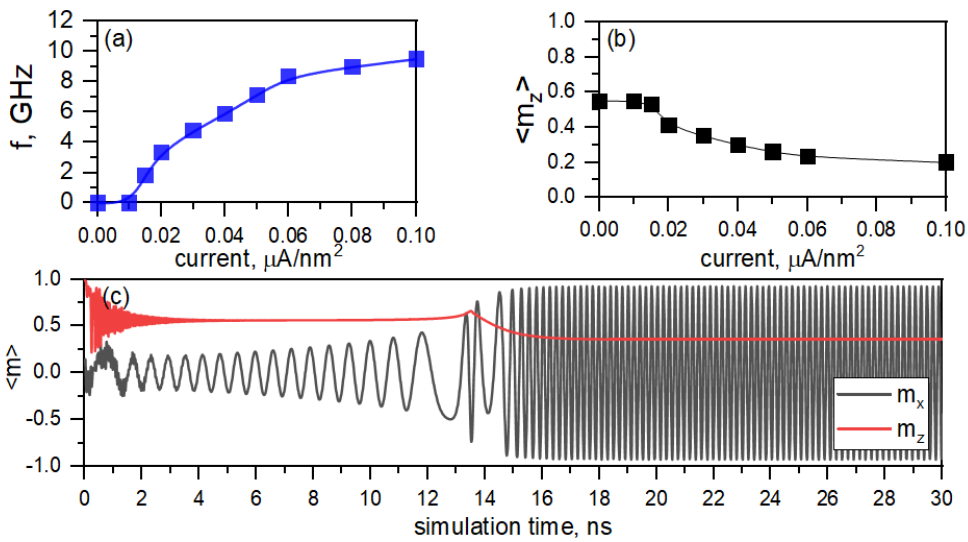

Figure 3.19: Micromagnetic simulations of easy-axis STO: (a) precession frequency (b) precession angle (c) m_z and m_x components for $J = 0.02\,\mu\text{A}/\text{nm}^2$. The thickness of free layer is $t_{FL} = 3.0\,\text{nm}$. For all simulations $M_s = 1350\,\text{emu}/\text{cm}^3$, $K_u = 1.11\,\text{Merg}/\text{cm}^3$, $\alpha = 0.008$, $A_{ex} = 10^{-6}\,\text{erg}/\text{cm}^2$ and diameter $D = 40\,\text{nm}$. The applied magnetic field was $H_{app} = 0.5\,\text{T}$.

We, then, compare the room temperature operation of the STOs including an easy-plane STO and an easy-axis STO with an applied field. The easy-axis STO with an applied field is chosen for comparison as it was the original idea for an STO and it was shown in multiple works [85,87,99,100]. Figures 3.20 (a) and (b) compare the frequency spectrum of the easy-plane STO and easy-axis STO with an applied field, respectively. The structure parameters of the STOs are chosen such that they operate at the same frequency at zero-temperature. We find that the linewidth of the easy-axis STO with an applied field is narrower compared to the easy-plane STO. We attribute the reduced linewidth in the latter

case to the fact that the precessional frequency is largely given by the applied field that is temperature and thermal noise independent. On the other hand, for the easy-plane single-FL STO, the precessional frequency is determined by the anisotropy and exchange interactions. These interactions are affected by the thermal noise because they are related to the instantaneous magnetization states, which are a part of the stochastic magnetization dynamics. We note that the operational linewidth can be reduced by synchronizing multiple STOs or synchronizing the STOs to an AC current or external field [101-103].

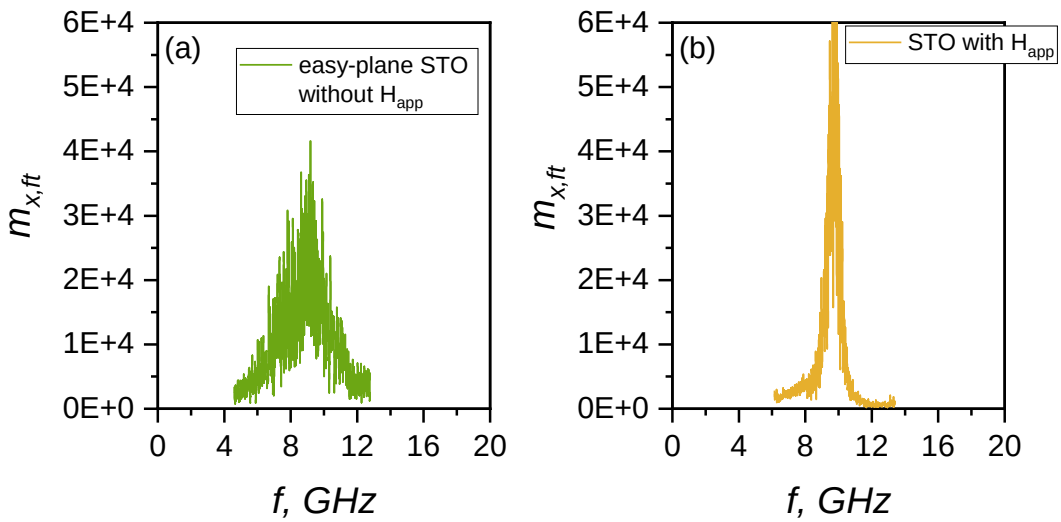

Figure 3.20: Fourier spectrum of m_x for the operation at room temperature of an STOs $J = 0.04\,\mu\text{A}/\text{nm}^2$ for (a) easy-plane single-FL STO with the following parameters: thickness $t = 0.8\,\text{nm}$, $M_s = 1350\,\text{emu}/\text{cm}^3$, $K_u = 1.11\,\text{Merg}/\text{cm}^3$, $\alpha = 0.008$; (b) easy-axis STO with an applied field with the following parameters: $t = 3.0\,\text{nm}$, $M_s = 1350\,\text{emu}/\text{cm}^3$, $K_u = 1.11\,\text{Merg}/\text{cm}^3$, $\alpha = 0.008$, $J = 0.01\,\mu\text{A}/\text{nm}^2$ and $H_{app} = 0.4\,\text{T}$. For all cases $D = 40\,\text{nm}$.

3.6.3 STO based on antiferromagnets

An absence of compact and reliable generators and receivers of coherent signals in the frequency range 0.1 – 10 THz has been identified as a fundamental physical and

technological problem. The existing approaches to THz-frequency generation, including superconductor Josephson junctions [104] or free electron lasers require complex setups. It has been demonstrated that ferromagnetic (FM) layered structures driven by a spin-transfer torque (STT) which compensates magnetic damping, can be used as spin-torque oscillator in the frequency range of 1–30 GHz [83]. In order to increase the generation frequency it was proposed to use antiferromagnets (AFM) rather than FM films as active layers of spintronic auto-oscillators [105]. Unfortunately, the traditional method of the STT-induced damping compensation in FM does not work for AFM. To compensate damping in a FM, the DC spin current must be polarized parallel to the direction of the static equilibrium magnetization. However, since AFMs have two magnetic sublattices with opposite magnetizations, the STT decreasing the damping in one of the sublattices increases it in the other sublattice, thus resulting in a zero net effect. Fortunately, the presence in an AFM of two magnetic sublattices coupled by a strong exchange interaction qualitatively changes the magnetization dynamics of AFM. In particular, it has been shown, that, in contrast with a FM, STT acting on an AFM can lead to a dynamic instability in the magnetic sublattice orientation which results in the rotation of the magnetizations of the AFM sublattices in the plane perpendicular to the direction of polarization of the applied spin current. This mechanism has been already used to experimentally switch the orientation of magnetic sublattices in AFM materials. However, the STT-induced rotation of the magnetic sublattices in an AFM has not been recognized so far as a possible mechanism of realization of THz-frequency AFM oscillators, since in a magnetically compensated AFM the steady rotation of sublattices does not create any AC spin-current. In this work [90] it was demonstrated theoretically that a simple structure consisting of a metallic Pt layer with

a strong spin-orbit interaction and a layer of a bi-axial antiferromagnetic (AFM) dielectric as shown in Figure 3.21. The THz-range frequency as a function of applied current density is shown on Figure 3.21.

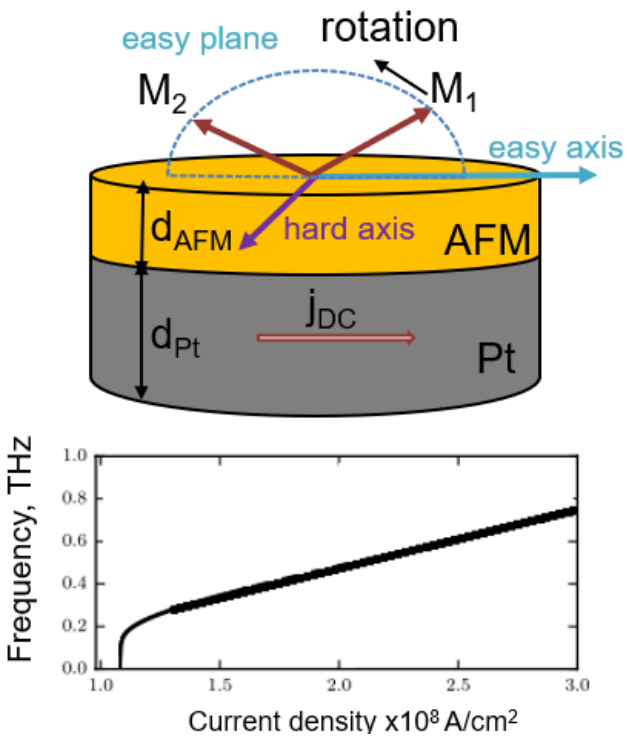

Figure 3.21: Schematic view of the THz-frequency oscillator based on a Pt/AFM bilayer. The AFM hard axis lies in the bilayer plane perpendicular to the direction of the DC STT current. Solid dark brown arrows show canted magnetizations under the action of the spin-current. The spin-transfer torque (STT)-induced non-uniform in time rotation of the canted AFM sublattices creates in the Pt layer an AC spin-pumping signal at THz frequencies. This geometry was initially proposed and discussed in [106].

Despite recent success in demonstrating STO functionality in devices of various geometries and configurations further research is necessary before STOs can enter a broader class of applications. For example, the output power and frequency should be significantly enhanced, the linewidths narrowed, and materials selection and fabrication process optimized. These challenges in part require systems and materials solutions, many of these challenges have recently been addressed [72,81,82]. The output power can be

enhanced by synchronizing multiple STO. The precessional frequencies can be enhanced by increasing the applied fields and currents during operation. Additional magnetic layers may be incorporated which exert local effective fields to avoid having the external applied fields. Materials and configuration considerations can help reduce distributions and linewidths. Narrow linewidths can improve STO synchronization properties and increase output power. Chapter 7 of this work presents a field-free spin-transfer oscillator based on composite antiferromagnets and combines the benefits of the STOs described in this chapter.

Part II

Micromagnetic modeling and analysis

Chapter 4

Micromagnetic modeling of perpendicular magnetic tunnel junction

There is considerable interest in perpendicular magnetic anisotropy (PMA) magnetic tunnel junctions (p-MTJ) for spin torque transfer random access memory (STT-RAM) for improved thermal stability and lower critical currents. Perpendicular magnetic anisotropy (PMA) materials have unique advantages when used in magnetic tunnel junctions, which are the most critical part of spin-torque transfer RAMs (STT-RAMs) that are being researched intensively as future non-volatile memory technology. In perpendicular magnetic anisotropy films, the demagnetizing field is in the same direction as that of the applied biasing field. Hence the perpendicular materials are thermally stable as the device size shrinks. The finite element linear basis representation from chapter 2 is used to model spin transfer torques in magnetic tunnel junction. In-plane and out-of-plane spin transfer torques are discussed in the context of all-metallic spin-valves and magnetic tunnel junctions with the current-perpendicular-to-plane geometry. The chapter also discusses the

micromagnetic study of the thermal stability and magnetization switching by spin polarized current in perpendicular magnetic tunnel junctions (p-MTJs).

4.1 Micromagnetic modeling of spin-transfer torque

4.1.1 All-metallic spin-valve

The spin transfer torque (STT) on either magnetic layer of a FM/NM/FM multilayer stack with current flowing perpendicular to the plane, can be expressed as:

$$\boldsymbol{\tau}_{STT+} = \eta(\theta)\frac{\gamma}{M_s \delta t}\frac{\hbar}{2}\frac{J_{+-}}{e}\hat{\mathbf{m}}_+ \times \hat{\mathbf{m}}_+ \times \hat{\mathbf{m}}_- . \tag{4.1}$$

Here, $\hat{\mathbf{m}}_+$ and $\hat{\mathbf{m}}_-$ are the unit magnetization vectors of the two ferromagnetic layers in the stack, $\hbar$ is the reduced Planck constant, γ is a gyromagnetic ratio, M_s is the saturation magnetization, e is an electron charge, δt is an effective depth and assuming that spin transfer is a purely an interface effect $\delta t \to 0$ and J_{+-} is the electric current density (positive when the electrons flow from layer + to layer -).

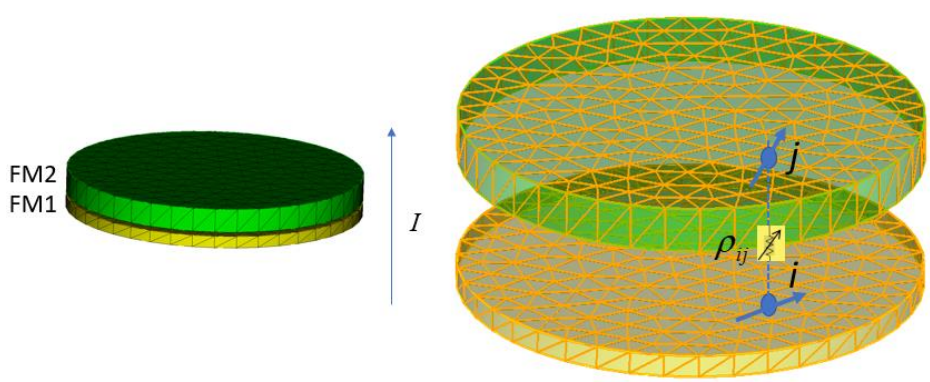

Figure 4.1: Finite element model representation of a spin valve. (a) a nanopillar composed of two ferromagnetic layers separated by a nonmagnetic spacer layer (spacer not shown) (b) a pairwise correspondence between the nodes and a conducting channel of variable resistivity used for modeling magnetoresistance to account for current redistribution for each pair of corresponding nodes.

The angular dependence of the STT efficiency can be written as:

$$\eta(\theta) = \frac{Q_+}{A + B\cos\theta} + \frac{Q_-}{A - B\cos\theta}, \tag{4.2}$$

where Q_+, Q_-, A and B are device-dependent constant [5] and $\cos\theta = \hat{\mathbf{m}}_+ \cdot \hat{\mathbf{m}}_-$.

Figure 4.1 shows a finite element representation of the cylindrical spin valve composed of two ferromagnetic layers separated by a nonmagnetic normal spacer layer (spacer layer not shown). Figure 4.1 shows the mesh that defines the discretized model in more detail. A tetrahedral discretization scheme is chosen that yields identical triangulation of the two NM/FM interfaces. The identical triangulation implies a pairwise correspondence between mesh nodes on opposite sides of the spacer layer. The spin torque acting on the magnetic moment in the vicinity of node can be represented in the finite element representation as [17]:

$$\boldsymbol{\tau}_{i,STT} = \varsigma_i \eta(\theta_{ij}) \frac{\gamma}{M_{s,i} t_i} \frac{\hbar}{2} \frac{J_{ij}}{e} \hat{\mathbf{m}}_i \times \hat{\mathbf{m}}_i \times \hat{\mathbf{m}}_j, \tag{4.3}$$

where $\hat{\mathbf{m}}_i$ and $\hat{\mathbf{m}}_j$ are unit magnetization vectors of node i and j, respectively. Node j is directly opposite of node i across the spacer layer, $\cos\theta = \hat{\mathbf{m}}_i \cdot \hat{\mathbf{m}}_j$, t_i is the effective depth associated with node i and depends on the local mesh dimensions and ς_i is an indicator function which equals unity if node i belongs to a NM/FM interface, and is zero otherwise.

The total electric current I_{total} flowing through the spin-valve is typically externally controlled, the current density J_{ij} can be approximated as $J_{ij} = I_{total} / S$, where S is the cross-sectional area of the spin valve. However, this approximation is not valid for the case of domain wall or non-uniform magnetization states in one or both magnetic layers. In this case the current should be redistributed and consider the effect of GMR mentioned in the

previous chapter 3 of this work. In micromagnetics GMR effect can be modeled by assigning to each interfacial node pair i, j a correspond conductivity channel with the resistance $\rho_{ij} = 1 + r_{MR}\left(1 - \cos\theta_{ij}\right)/2$, where $r_{MR} = \left(R_{AP} - R_P\right)/R_P$ is the GMR ratio discussed in section 3.2.1. The current density for each channel $J_{ij} = V/\rho_{ij}$, where V is the voltage difference between NM/FM interfaces. The current for each channel could be written as $I_{ij} = G_{ij}V$, $G_{ij} = S_{ij}/\rho_{ij}$ where G_{ij} is the conductance and S_{ij} is the cross-area of the correspondent channel. Using the law of the charge conservation the voltage through the spin-valve could be written as $V = I_{total}/G$, where $G = \sum_{i,j} 1/\rho_{ij} = \sum_{i,j} G_{ij}$ represents the total conductivity of the array of the parallel channels through the space layer (Figure 4.1). Sometimes if the total voltage V_{total} across the device is known the voltage drop at each resistor could be found, and the current density at interfacial node i could be represented as $J_{ij} = I_{ij}/S_{ij}$. Using the equation (4.3) we can write the Landau-Lifshitz-Gilbert (LLG) equation with STT term associated with the influence of spin polarized currents and magnetic fields:

$$\frac{d\hat{\mathbf{m}}_i}{dt} = -\gamma\hat{\mathbf{m}}_i \times \mathbf{H}_{i,eff} + \alpha_i\hat{\mathbf{m}}_i \times \frac{d\hat{\mathbf{m}}_i}{dt} + \varsigma_i\eta\left(\theta_{ij}\right)\frac{\gamma}{M_{s,i}t_i}\frac{\hbar}{2}\frac{J_{ij}}{e}\hat{\mathbf{m}}_i \times \hat{\mathbf{m}}_i \times \hat{\mathbf{m}}_j, \qquad (4.4)$$

or it could be rewritten as

$$\frac{d\hat{\mathbf{m}}_i}{dt} = -\gamma\hat{\mathbf{m}}_i \times \left(\mathbf{H}_{i,eff} + \mathbf{H}_{i,STT}\right) + \alpha_i\hat{\mathbf{m}}_i \times \frac{d\hat{\mathbf{m}}_i}{dt}, \qquad (4.5)$$

where the STT field can be represented as:

$$\mathbf{H}_{i,STT} = -\varsigma_i\eta\left(\theta_{ij}\right)\frac{1}{M_{s,i}t_i}\frac{\hbar}{2}\frac{J_{ij}}{e}\hat{\mathbf{m}}_i \times \hat{\mathbf{m}}_j, \qquad (4.6)$$

is a field-like expression for the STT term, which could be added to the total effective field $\mathbf{H}_{i,eff}$. Equation (4.4) can be written in an explicit form:

$$\frac{d\hat{\mathbf{m}}_i}{dt} = -\frac{\gamma}{1+\alpha_i^2}\left[\hat{\mathbf{m}}_i \times \left(\mathbf{H}_{i,eff} + \mathbf{H}_{i,STT}\right) + \alpha_i \hat{\mathbf{m}}_i \times \hat{\mathbf{m}}_i \times \left(\mathbf{H}_{i,eff} + \mathbf{H}_{i,STT}\right)\right]. \qquad (4.7)$$

it has been shown that the $\mathbf{H}_{i,STT}$ in the second term on the right-hand side of the equation 4.7 does not noticeable affect the magnetization dynamics in spin-valve structures.

4.1.2 Magnetic tunnel junction

In the case of micromagnetic modeling of spin transfer torques in MTJs the so-called out-of-plane torque contribution in addition to the in-plane torque contribution [17] is considered. The out-of-plane torque is given by:

$$\boldsymbol{\tau}_{OPSTT,+} = \beta\eta(\theta)\frac{\gamma}{M_s \delta t}\frac{\hbar}{2}\frac{J_{+-}}{e}\hat{\mathbf{m}}_+ \times \hat{\mathbf{m}}_- , \qquad (4.8)$$

where all the symbols have the same meaning as in equation (4.1) and β is the magnitude of the out-of-plane torque $\boldsymbol{\tau}_{OPSTT,+}$ with respect to the in-plane torque contribution in equation 4.1. The LLG equation for MTJ could be rewritten as:

$$\begin{aligned}\frac{d\hat{\mathbf{m}}_i}{dt} = &-\gamma \hat{\mathbf{m}}_i \times \mathbf{H}_{i,eff} + \alpha_i \hat{\mathbf{m}}_i \times \frac{d\hat{\mathbf{m}}_i}{dt} + \varsigma_i \eta\left(\theta_{ij}\right)\frac{\gamma}{M_{s,i} t_i}\frac{\hbar}{2}\frac{J_{ij}}{e}\hat{\mathbf{m}}_i \times \hat{\mathbf{m}}_i \times \hat{\mathbf{m}}_j \\ &+ \beta \varsigma_i \eta\left(\theta_{ij}\right)\frac{\gamma}{M_{s,i} t_i}\frac{\hbar}{2}\frac{J_{ij}}{e}\hat{\mathbf{m}}_i \times \hat{\mathbf{m}}_j .\end{aligned} \qquad (4.9)$$

The explicit form of the equation (4.9) can be written as:

$$\frac{d\hat{\mathbf{m}}_i}{dt} = -\frac{\gamma}{1+\alpha_i^2}\left[\hat{\mathbf{m}}_i \times \left(\mathbf{H}_{i,eff} + \mathbf{H}_{i,STT}\right) + \alpha_i \hat{\mathbf{m}}_i \times \hat{\mathbf{m}}_i \times \left(\mathbf{H}_{i,eff} + \mathbf{H}_{i,STT}\right)\right], \qquad (4.10)$$

where the equations for the corresponding fields can be written as:

$$\mathbf{H}_{i,STT} = \mathbf{H}_{i,IPSTT} + \mathbf{H}_{i,OPSTT},$$
$$\mathbf{H}_{i,IPSTT} = -\varsigma_i \eta\left(\theta_{ij}\right) \frac{1}{M_{s,i} t_i} \frac{\hbar}{2} \frac{J_{ij}}{e} \hat{\mathbf{m}}_i \times \hat{\mathbf{m}}_j, \tag{4.11}$$
$$\mathbf{H}_{i,OPSTT} = -\beta \varsigma_i \eta\left(\theta_{ij}\right) \frac{1}{M_{s,i} t_i} \frac{\hbar}{2} \frac{J_{ij}}{e} \hat{\mathbf{m}}_j.$$

Here, $\mathbf{H}_{i,IPSTT}$ and $\mathbf{H}_{i,OPSTT}$ are accounting in-plane and out-of-plane torques, respectively.

4.2 Perpendicular magnetic tunnel junction

Magnetic random-access memory (MRAM) devices are envisioned as a major candidate for future memory technologies [66,107,108]. Recent MRAM prototypes use perpendicular magnetic tunnel junctions (p-MTJ) as a storage element. Several experimental [57,109,110] and computer modeling [62,111] studies of p-MTJ devices have been presented. The main advantages of p-MTJ compared to in-plane MTJ are higher thermal stability and critical switching current reduction for p-MTJ. Theoretical works characterizing the thermal stability and switching currents of p-MTJ devices often follow from macrospin based models, which turn out to be invalid when non-uniform magnetization dynamics occurs. A direct relation between the thermal stability and switching current is often assumed while such relation is not, in fact, present when non-uniform magnetization dynamics occurs. Therefore, extracting thermal barrier from current measurements typically results in values that do not correspond to the real thermal stability for the device. Even for small p-MTJs, the scaling of the thermal stability and switching currents with respect to the device size can be non-trivial and does not follow typically presented simplified models. Thermal stability factor discussed in section 3.3.2 of this work

is related to the minimal energy path (MEP) and generally can be via uniform rotation or domain wall while switching by spin-polarized current is related to the magnetostatic field distribution in the device and is related more to local effects during switching, especially for large devices.

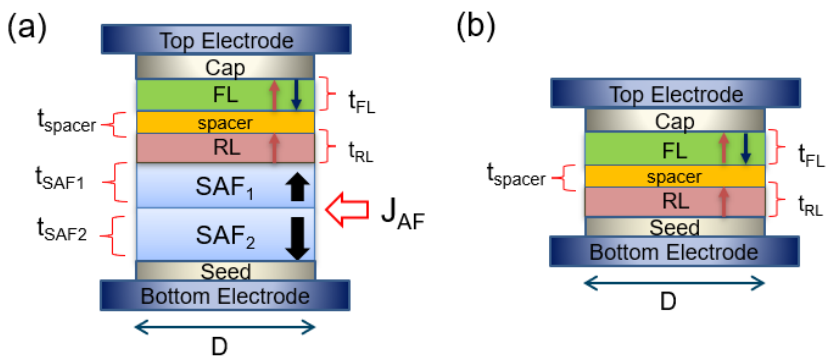

Figure 4.2: Perpendicular magnetic tunnel junction (p-MTJ) stack: (a) full stack, (b) simplified model with standalone free layer.

We consider a four-layer stack of cylindrical cross-section of diameter D (Figure 4.2). The stack includes a free layer (FL), reference layer (RL), and two synthetic anti-ferromagnet layers (SAF1 and SAF2). FL has a thickness of t_{FL}, saturation magnetization M_{sFL}, perpendicular uniaxial surface anisotropy at the bottom surface with density K_{sFL} and no bulk anisotropy. RL has $t_{RL} = t_{FL}$, $M_{sRL} = M_{sFL}$ and surface anisotropy energy $K_{sRL} = K_{sFL}$ on its top surface. SAF1 has thickness t_{SAF1} and SAF2 has a thickness t_{SAF2}, saturation magnetization $M_{sSAF1} = M_{sSAF2}$, and volumetric uniaxial anisotropy $K_{uSAF1} = K_{uSAF2}$. SAF1 and SAF2 are exchange coupled with negative surface exchange energy density J_{AF}. RL is strongly ferromagnetically coupled to SAF1. RL and FL are separated with a spacer layer of thickness t_{spacer}. SAF1 and SAF2 are intended for

compensating the magnetostatics effects of RL and their thickness in all results is chosen such that the magnetostatic field generated by the RL, SAF1, and SAF2 averaged in the volume of FL is zero. For comparison and for highlighting the influence of the full stack, we also show and discuss results for a simplified model of a standalone FL (Figure 4.2 (b)), i.e. assuming a fixed RL and excluding its magnetostatic effects [112]. As we show next, the current-induced switching process is significantly affected by the magnetostatic field due to the presence of the stack. For the full 4-layer stack we define the antiparallel to parallel (AP-P) and parallel to antiparallel (P-AP) magnetization states of the FL with respect to the RL magnetization direction.

The simulations are accomplished using a finite element based micromagnetic simulator FastMag [113], which allows computing the magnetization dynamics by solving the Landau-Lifshitz-Gilbert equation and separately the energy barrier by using the Nudged Elastic Band method (NEB method) [114] discussed in section 2.5 of this work, which finds a set of the magnetization states (images) associate with energies along MEP.

4.2.1 Minimal energy path and thermal stability

One of the key parameters characterizing p-MTJ devices is the normalized energy barrier $\Delta = E/k_B T$, where E is the energy barrier between the up and down or down and up states, k_B is Boltzmann's constant, and T is the temperature, assumed to be $T = 300\,\mathrm{K}$, i.e. the room temperature. Another key parameter is the critical current density J_{C0} required for the FL switching. Finally, an important parameter characterizing the efficiency of an

MTJ operation is the figure of merit $FOM = \Delta / I_{C0}$, where I_{C0} is the critical switching current related to J_{C0} via $I_{C0} = J_{C0} \pi D^2 / 4$.

Figure 4.3 shows the results for the three parameters, Δ, J_{C0}, and FOM as a function of the D and FL thickness t_{FL}. We identify three regimes: small, intermediate, and large D. For small D, roughly $D < 20\,\text{nm}$, Δ increases with D and decreases with t_{FL}. The value of J_{C0} decreases with both D and t_{FL}. The corresponding FOM is nearly flat independent of D, as predicted by macrospin based models.

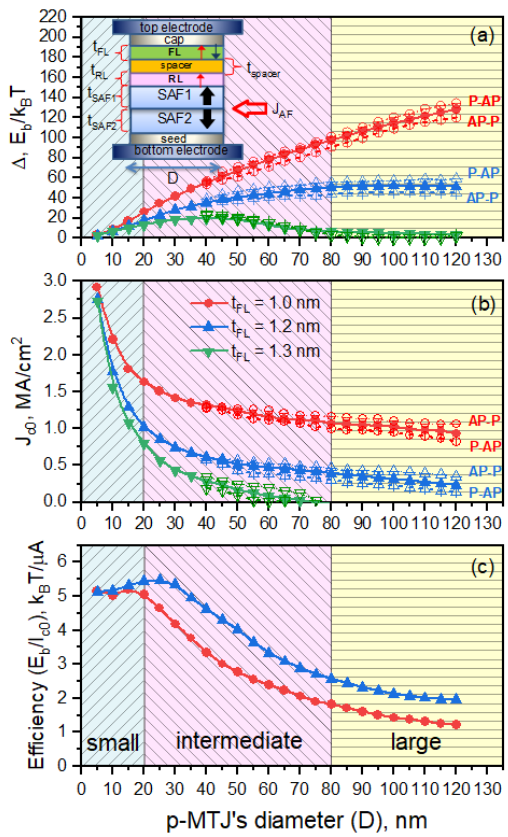

Figure 4.3: (a) Thermal stability factor Δ, (b) Switching current density J_{C0}, (c) FOM vs. D for different t_{FL} for $M_{sFL} = M_{sRL} = 1200\,\text{emu/cm}^3$, $M_{sSAF1} = M_{sSAF2} = 340\,\text{emu/cm}^3$, $K_{sFL} = 1.088\,\text{erg/cm}^2$, $K_{uSAF1} = K_{uSAF2} = 1.24\,\text{Merg/cm}^3$, $A_{ex} = 10^{-6}$ erg/cm, $J_{AF} = -0.1242\,\text{erg/cm}^2$, $\alpha = 0.008$, $t_{SAF1} = 3\,\text{nm}$, $t_{spacer} = 1\,\text{nm}$.

The behavior can be explained by considering that the MEP and switching for smaller D are both obtained by uniform magnetization rotation, so that both Δ and I_{C0} scale as $K_{eff}D^2$, where K_{eff} is the effective anisotropy given by:

$$K_{eff} = \frac{K_{sFL}}{t_{FL}} - \frac{\pi M_s^2 (3N_z - 4\pi)}{4\pi}. \tag{4.12}$$

and N_z is the demagnetization factor depending on D [10] described in section 2.4.3. We observed that the range of such macrospin-like behavior is extended to larger D for thicker FL. We attribute this to a greater demagnetization field associated with a greater DW width, hence delaying the initiation of non-uniform magnetization modes. We also observe no substantial difference in single FL versus compensated 4-layer stack models in this regime. From Figure 4.3 (c), this is the most efficient regime for p-MTJ device operation, so it is advantageous to engineer the free layer to delay the onset of non-uniform modes which reduce the efficiency of the device.

For intermediate D around $(20\,\text{nm} < D < 80\,\text{nm})$, Figure 4.3 shows that J_{C0} presents a slower decrease with increasing D, while I_{C0} increases with D. Δ shows non-trivial behavior, where thinner FLs show a decreased dependence on D, whereas thicker FLs (1.3 nm) have a maximal Δ in the D dependence followed by the Δ reduction to zero eventually, at which point the switching current also goes to zero. An interesting observation is that FOM can show a maximum at some optimal $D = D_0$, which occurs at $D \sim 30\,\text{nm}$ for the middle FL thickness (1.2 nm). Such maximum occurs at greater D for thicker FLs. We attribute this maximum to different behaviors for current-induced switching versus MEP. Both switching and MEP transition from a uniform rotation to DW

motion around the same D, i.e. $D = 40\,\text{nm}$, as shown in Figures 4.4 and 4.6 (a). However, MEP presents a more uniform magnetization than the switching path, and the DW for the MEP is wider. This is because switching is due to the spin transfer torque (STT) [18,19]; STT can be included as an additional effective field (or torque) component, which reduces the domain wall width. The more uniform MEP utilizes more volume for Δ, thus leading to a greater FOM. However, for large enough D, MEP is fully dominated by the DW and the behavior changes to that of the large range discussed later.

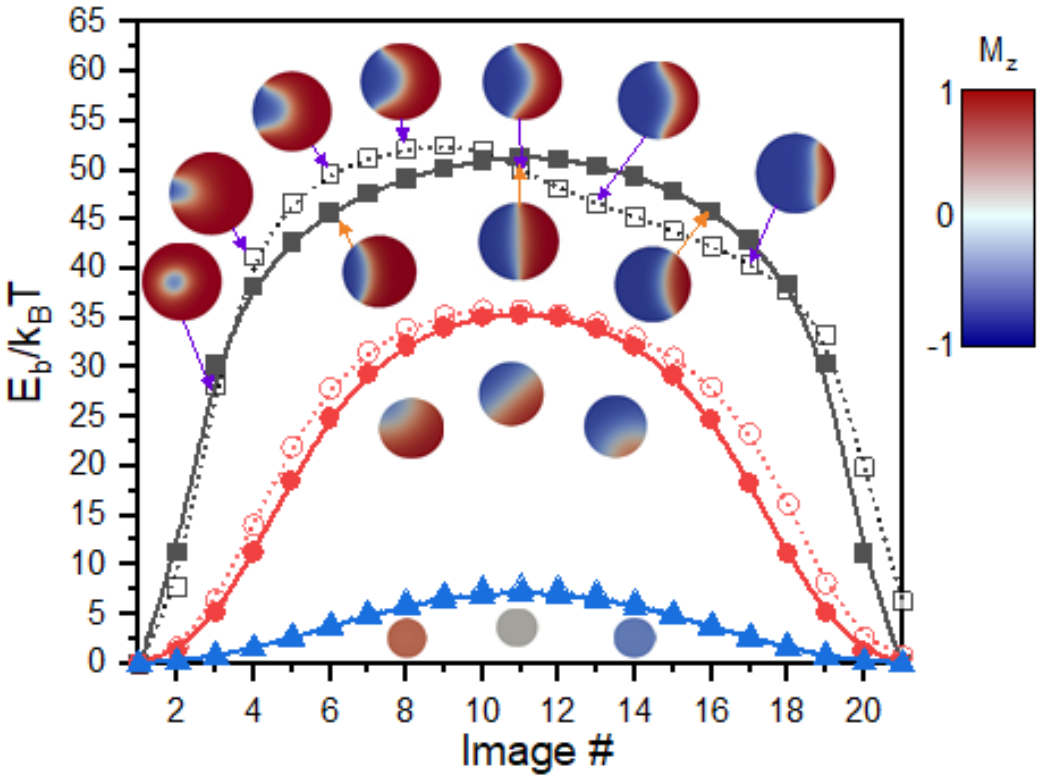

Figure 4.4: MEP and associated images vs. the image # for $t_{FL} = 1.2\,\text{nm}$ and $D = 10\,\text{nm}$, $40\,\text{nm}$, and $120\,\text{nm}$. Standalone FL, $D = 10\,\text{nm}$, Standalone FL, $D = 40\,\text{nm}$, Standalone FL with $D = 120\,\text{nm}$. Stack, $D = 10\,\text{nm}$, Stack, $D = 40\,\text{nm}$, Stack, $D = 120\,\text{nm}$. The structure properties are as in Figure 4.3.

To explain the transition out of the single domain regime, consider first the case of a standalone FL. We can give an approximation:

$$K_{eff} \approx \frac{K_{sFL}}{t_{FL}} - 2\pi M_s^2 + \frac{3\pi M_s^2 t_{FL}}{D}, \tag{4.13}$$

obtained by the first-order Taylor expansion of the demagnetization factor N_z for small t_{FL}/D. For thicker FL, the factor $K_s/t_{FL} - 2\pi M_s^2$, which is the infinite film effective anisotropy energy density, is smaller and can even be negative. The third term $3\pi M_s^2 t_{FL}/D$ contributes to K_{eff}, but it becomes smaller with an increase of D. This leads to a slower or no increase of Δ with D and decrease of J_{C0}. We find that MEP is by DW for the standalone FL for any D in this regime. This behavior differs from what is suggested by [108], where for greater D a bubble-like MEP is hypothesized.

4.2.2 Current-induced magnetization switching and efficiency

The switching is a more complicated process. The initial switching dynamics in the form of precession starts in the center, in contrast to the MEP, which starts at the edge of the device.

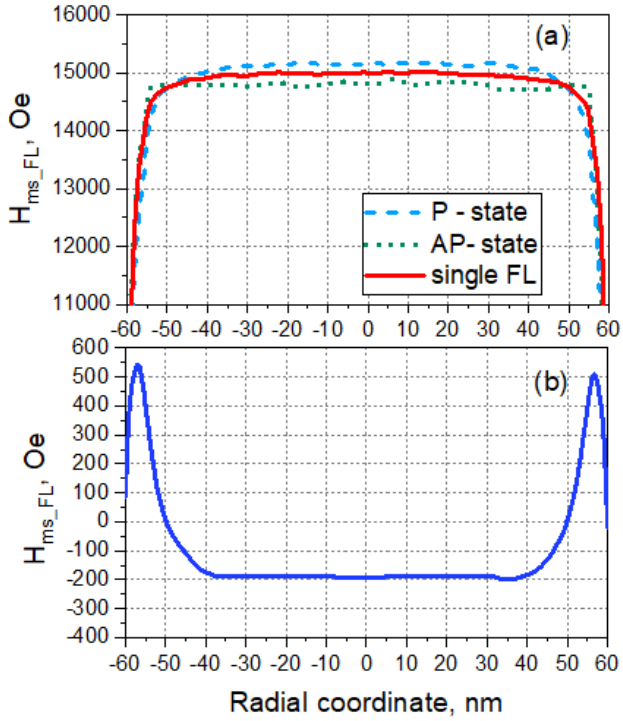

Figure 4.5: Magnetostatic field profile in p-MTJ free layer. (a) Total magnetostatic field profile in FL and (b) Stray field in FL from the rest of the stack (excluding FL) for $t_{FL} = 1.2$ nm and $D = 120$ nm.

The reason for that becomes clear considering the demagnetization field in the free layer shown in Figure 4.5 (a). The field is stronger in the middle, which makes the initial dynamics to become easier. The way it leads to switching is different depending on the size. For not too large sizes (the approximate range of $20\,\text{nm} < D < 60\,\text{nm}$), the initial dynamics propagates to the edge, nucleating a DW. The DW propagates, leading to switching. For greater diameters $(D > 60\,\text{nm})$, the precession in the middle can continue for an extended period of time until the edges switch, followed by non-uniform dynamics of more than one DW (see Figure 4.6 (a)). Such a process appears as bubble-like switching [109,111]. We emphasize that such bubble-like behavior is obtained even for a standalone FL and is not necessarily caused by the stack. Finally, in the intermediate regime, we observe no

substantial difference for single FL versus compensated 4-layer stack behavior, just up to 8% for Δ and 10% for J_{c0} in Figure 4.3.

In the large diameter regime, we find there is a substantial effect of the full stack on Δ, MEP, J_{c0}, and switching behavior. Even though the stack is compensated, there is still a noticeable difference of Δ and J_{c0} for the AP-P and P-AP transitions. This is unlike for the smaller D, where the compensation results in the same Δ and J_{c0} as for standalone FLs. These differences are due to the non-uniform and non-symmetric MEP and switching path caused by the magnetostatic fields from the stack (see Figure 4.5 (b)).

When comparing the minimal energy path MEP in Figure 4.4 for the standalone FL vs. the full stack, we find that the stack creates a non-symmetric path and even the maximum energies differ. The saddle point, which is the state of the largest energy, is shifted towards one of the ends, so that it corresponds to a curved DW. This can be explained by the fact that the magnetostatic field from the SAF1,2 and RL is non-uniform. Together with the demagnetization field of the FL (see Figure 4.5 (a)), it leads to a different magnetostatic field distribution in the FL for AP-P and P-AP cases, so that it re-arranges the MEP resulting in the differences in Δ demonstrated in Figure 4.4.

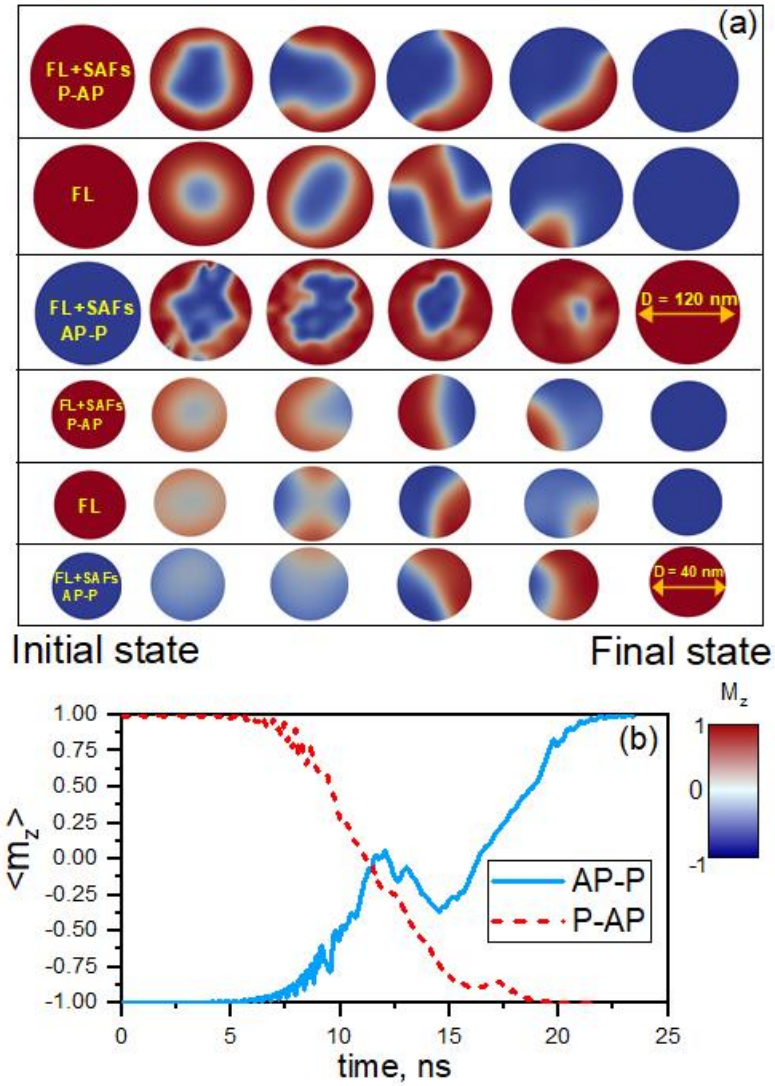

Figure 4.6: Current-induced switching of p-MTJ. (a) Snapshots of the z-component of the normalized magnetization m_z for $D = 40\,\text{nm}$ and $120\,\text{nm}$ for $t_{FL} = 1.2\,\text{nm}$; (b) average normalized magnetization m_z vs. time for $D = 120\,\text{nm}$ and $t_{FL} = 1.2\,\text{nm}$. An applied current density was $J = 1.35\,\text{MA/cm}^2$ and $J_{C0,P-AP} \approx 0.23\,\text{MA/cm}^2$, $J_{C0,AP-P} \approx 0.31\,\text{MA/cm}^2$.

Similarly, the switching behavior (shown in Figure 4.6) also significantly differs for the AP-P and P-AP cases for larger diameters ($D > 80\,\text{nm}$). For the P-AP, the switching behavior is similar to that obtained for the standalone FL, i.e. dynamics starts from the middle, a bubble is formed that persists in the middle for a period of time, the bubble leads

to nucleation at the edge, which propagates via a DW, resulting a switching. On the other hand, for the AP-P case, switching starts from the edges, forming an "inverse bubble". The inverse bubble persists for a period of time until switching is accomplished. The resulting switching time tends to be longer than that for the P-AP case and the switching current (Figure 4.6 (b)) is higher. This behavior, again, is explained by the non-uniform magnetostatic field distributions due to the combination of the demagnetization field in the FL and the field from the RL and SAF1,2. The field from the stack is stronger positively closer to the edge and weaker negatively in the middle (Figure 4.5 (b)). For the P-AP case it enhances the FL demagnetization field in the middle supporting the bubble switching. For the AP-P case it locally enhances the FL demagnetization field at the edge and suppresses it in the middle, thus leading to the inverse bubble behavior.

The corresponding FOM decreases for all thicknesses at the rate of $\frac{1}{D}$ [66,108]. To explain this behavior, let us consider a standalone FL. Both MEP and switching are by DW. The value of energy barrier Δ could be represented as:

$$\Delta = \frac{4t_{FL}D(K_{eff}A_{ex})^{1/2}}{k_B T}, \tag{4.14}$$

with exchange constant A_{ex}, which is obtained as the DW energy as the DW passes through the diameter [46,66,115]. J_{C0} is related to the current required for the DW nucleation and it is approximately the same as the current required for switching a small FL, i.e.

$$J_{C0} = \frac{4\alpha e K_{eff} t_{FL}}{\eta \hbar}. \tag{4.15}$$

where η is the spin transfer torque efficiency, α is the damping constant, $\hbar$ is reduced Plank constant, and e is the electron charge. For the stack, FOM has a similar behavior

because Δ and J_{C0} have the same trends of increase and decrease for the P-AP and AP-P cases. We stress the fact that for larger D there is no direct relation between J_{C0} or I_{C0} and Δ.

In summary, we found that there may be significant differences in the energy path and switching behaviors depending on geometrical and stack parameters. Perpendicular magnetic tunnel junction (p-MTJ) comprising a four-layer stack of free layer, reference layer and synthetic antiferromagnets is discussed. It is demonstrated that the minimal energy path (MEP) – related to the thermal stability of the system – does not necessarily follow the same trajectory as the current-induced switching. The MEP can be by uniform rotation (UR) or by domain wall (DW), whereas the current-induced switching can be by UR, DW, or by bubble formation depending on geometrical and stack parameters. The bubble formation is further affected by the direction of switching, i.e. parallel to antiparallel (P-AP) versus AP-P switching. It is shown that the existence of different regimes where the energy barrier (EB) and the figure of merit, defined as a ratio between the energy barrier and switching current, show characteristic dependencies and even optimum points depending on the device diameter and the stack parameters. The presented results may explain recent experiments. For smaller D, both the MEP and switching are by uniform rotation. For larger D, the MEP is by DW, whereas switching can be by DW or by a bubble formation, which agrees with recent theoretical works [115,116]. The bubble can be formed in a standalone FL and in the 4-layer stack. For the P-AP case the bubble is formed similarly to the standalone case, starting from the middle. On the other hand, for the AP-P case, an inverse bubble is formed, starting from the edge. Depending on the geometry and material parameters Δ can increase with D, be constant, or decrease. Contrary to general

theoretical models [46,115] and in agreement with recent experimental works [111,116,117], the FOM can have a peak in its diameter dependence, which is attributed to the difference in the DW diameter for the MEP and switching path. For greater diameters, the FOM scales as 1/D.

Acknowledgement

Chapter 4, in part, is a reprint of material as appeared in I. Volvach, J. G. Alzate, Y. J. Chen, A. J. Smith, D. L. Kencke, and V. Lomakin, "Thermal stability and magnetization switching in perpendicular magnetic tunnel junctions," Applied Physics Letters 116, 19 (2020). This work was supported by Semiconductor Research Corporation. The dissertation author was the primary investigator and author of the text used in this chapter.

Chapter 5

Perpendicular magnetic tunnel junction with composite free layer

Spin transfer torque (STT) MRAM devices utilizing perpendicular magnetic tunnel junctions (p-MTJs) are the most promising candidates [79,118]. An important goal in designing p-MTJ devices are reducing the switching current while maintaining a required thermal stability. Unfortunately, there are limitation on the ability to achieve this goal. Increasing the lateral device size leads to a decrease of the figure of merit (FOM), viz. the ratio between the energy barrier and switching current [46,108]. Increasing the thickness when using surface anisotropy [60] leads to limitations in terms of thermal stability. Increasing the thickness when possibly using bulk anisotropy would not help with increasing FOM. It was shown earlier that using an exchange-coupled-composite free layer (ECC FL) for perpendicular magnetic tunnel junction can improve the operation as predicted by a two-spin model [119]. In [119] was mention that relatively insensitive to the damping parameter of the magnetic hard layer in the ECC structure. However, neither the

operation of ECC FLs for more realistic cases of non-uniform switching nor their energy barriers have been investigated.

This chapter presents a micromagnetic study of ECC FL for perpendicular magnetic tunnel junction (p-MTJs). The study includes the switching current, energy barrier, and efficiency, viz. the ratio between the energy barrier and switching current, as functions of the structure size and exchange energy density. This chapter also shows that using ECC FL can lead to significant improvement of the switching properties, particularly in the regime in which the magnetization dynamics is spatially non-uniform.

5.1 Operation of the exchange-coupled-composite free layer (ECC FL)

We consider a circularly cylindrical stack of diameter D as shown on the Figure 5.1. The stack includes an ECC FL with two ferromagnetic layers FL_{hard} and FL_{soft} as well as a reference layer exchange coupled to the synthetic antiferromagnetic layers. FL_{hard} has a thickness $t_{FL_{hard}}$, saturation magnetization $M_{sFL_{hard}}$ and perpendicular volumetric uniaxial anisotropy $K_{uFL_{hard}}$. FL_{soft} has a thickness $t_{FL_{soft}} = t_{FL_{hard}}$, $M_{sFL_{soft}} = M_{sFL_{hard}}$ and volumetric uniaxial anisotropy energy density $K_{uFL_{soft}}$. We note that the volumetric anisotropy can be also considered as an equivalent representation of the surface anisotropy. FL_{hard} and FL_{soft} are ferromagnetically exchange coupled with surface exchange energy density J_{ex}.

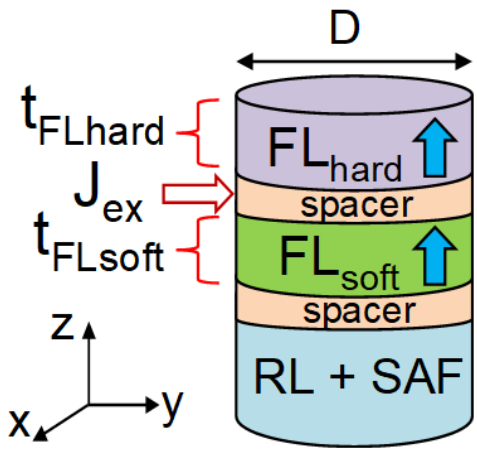

Figure 5.1: p-MTJ stack, including ECC free layer and SAF reference layers.

We define $\kappa = K_{uFL_{hard}} / K_{uFL_{soft}}$ as the ratio between the volumetric uniaxial anisotropy energy densities of the ECC FL sublayers. The RL and SAF are compensated in that the magnetostatic field generate by them and averages the free layers is zero. For the current induced switching simulations we assume the spin transfer torque (STT) via Slonczewski's models [120,121] at the bottom surface of FL_{soft} with the current density J_c. The presented simulations are accomplished using a finite-element-based micromagnetic simulator FastMag [113]. FastMag allows computing the magnetization dynamics by solving the Landau–Lifshitz–Gilbert equation. It also allows computing the energy barrier by using the nudged-elastic-band (NEB) method [114], which finds a set of magnetization states (images) associated with energies along the minimal energy path (MEP).

5.2 Characterization of p-MTJ with ECC FL

The key parameters considered are the normalized energy barrier $\Delta = E_b / k_B T$, where E_b is the energy barrier between the up and down or down and up states as determined by the NEB method, k_B is Boltzmann's constant, and temperature $T = 300\,\mathrm{K}$ as well as the critical switching current density J_{c0} and figure of merit (FOM) or efficiency:

$$FOM = \frac{4E_b}{\pi D^2 J_{c0}}. \tag{5.1}$$

We considered devices of two diameters: $D = 40\,\mathrm{nm}$ representing a case a domain-wall switching and MEP and $D = 10\,\mathrm{nm}$ representing a case of mostly uniform switching and MEP. The thickness of the layers for the $D = 10\,\mathrm{nm}$ case is chosen larger to maintains a sufficiently high thermal stability. For different values of κ we adjusted $K_{uFL_{hard}}$, such that $\Delta = 85$ in the limit of sufficiently large J_{ex}. We chose this approach (of adjusting $K_{uFL_{hard}}$) to make the comparison of J_{c0} and FOM clear. Keeping the same value of $K_{uFL_{hard}}$ leads to lower values of J_{c0}, but the behavior of all the parameters with respect to J_{ex} is the same.

Figure 5.2 shows Δ, J_{c0}, and FOM as a function of J_{ex} for different κ for $D = 40\,\mathrm{nm}$ in Figure 5.2 (a-c) and $D = 10\,\mathrm{nm}$ in Figure 5.2 (d-f). From Figures 5.2 (a) and (d), Δ increases with J_{ex} until J_{ex} reaches a certain saturation level at which Δ is maximal. From Figure 5.2 (b) and (e), J_{c0} is non monotonous with J_{ex} but rather has an optimal value at which it is minimal. The reduction of J_{c0} is greater for greater κ and it can be reduced more than twice as compared to the single FL case.

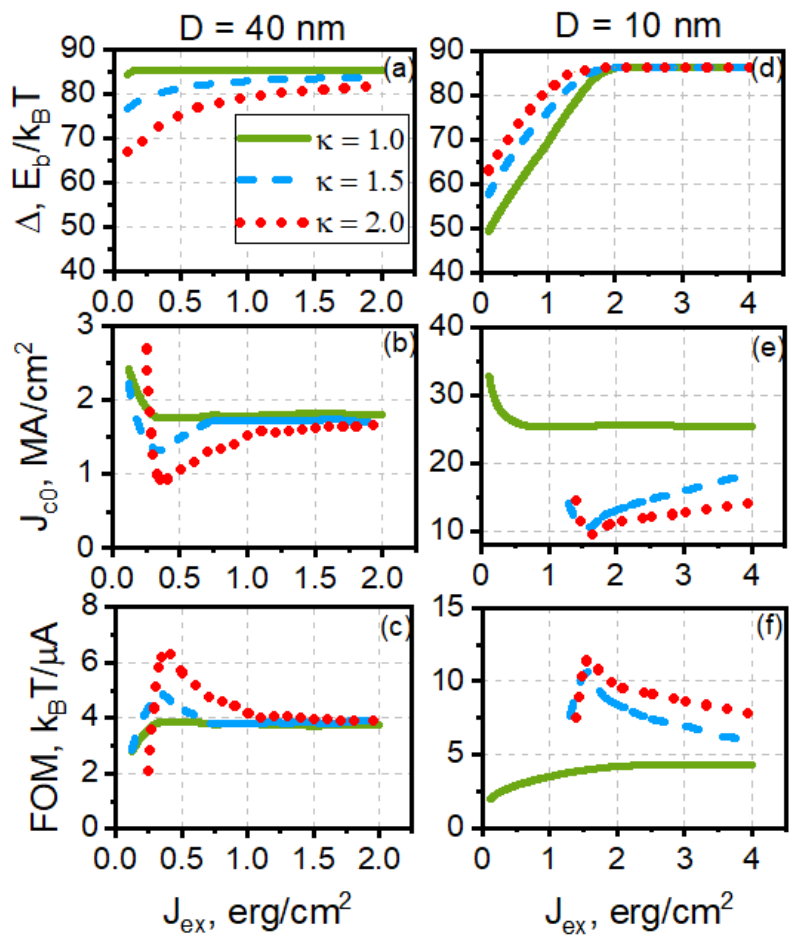

Figure 5.2: Thermal stability, critical switching current density and efficiency of p-MTJ with ECC free layer. (a) Thermal stability Δ, (b) critical current density J_{c0}, (c) FOM vs. J_{ex} for $D = 40\,\text{nm}$ $t_{FL_{soft}} = t_{FL_{hard}} = 1.2\,\text{nm}$, $t_{spacer} = 0.3\,\text{nm}$. (d) Δ, (e) J_{c0}, (f) FOM vs. J_{ex} for $D = 10\,\text{nm}$, $t_{FL_{soft}} = t_{FL_{hard}} = 4.0\,\text{nm}$, $t_{spacer} = 0.3\,\text{nm}$. In all cases $M_{sFL_{hard}} = M_{sFL_{soft}} = 960\,\text{emu/cm}^3$, $A_{ex} = 10^{-6}$ erg/cm, $\alpha = 0.008$, $K_{uFL_{hard}} = K_{uFL_{soft}} = 6.11\,\text{Merg/cm}^3$ for $\kappa = 1.0$, $K_{uFL_{hard}} = 7.33\,\text{Merg/cm}^3$ and $K_{uFL_{soft}} = 4.88\,\text{Merg/cm}^3$ for $\kappa = 1.5$, $K_{uFL_{hard}} = 8.14\,\text{Merg/cm}^3$ and $K_{uFL_{soft}} = 4.07\,\text{Merg/cm}^3$ for $\kappa = 2.0$.

The corresponding FOM in Figure 5.2 (c) and (f) has a peak with respect to J_{ex} with the maximal improvement of FOM of over 1.6 times. The mechanism leading to these improvements is that switching of FL_{soft} assists in switching of FL_{hard}. It is important that the FL_{soft} is next to RL, as it is easier to start switching it first. The switching of FL_{hard} is

then induced. For too small J_{ex}, the exchange strength is not sufficient to switch FL_{hard}. For too large J_{ex}, the hard layer prevents switching of the soft layer. For the optimal J_{ex}, the exchange strength both allows easier switching of FL_{soft} by STT and allow the following switching of FL_{hard} by exchange coupling. The saturation J_{ex} for Δ and the optimal J_{ex} for J_{c0} and FOM are significantly higher for the case of $D = 10\,\text{nm}$. This is explained by the greater layer thickness, i.e. the effect of the surface exchange coupling needs to propagate through the larger thickness of the layers to lead to switching of the entire layers.

5.2.1. Thermal stability

The behavior of Δ in Figure 5.2 (a) and (d) is explained in more detail in Figure 5.3, which shows MEP between the up and down states of the ECC FL for selected κ and J_{ex}. For $D = 40\,\text{nm}$ in Figure 5.3 (a) and (b), the MEP is by domain wall reversal. This is similar to the behavior shown in Figure 5.2 of [60] and this is because this D is greater than the domain wall length, which approximately is $8\,\text{nm}$. The MEP has a local minimum for weakly coupled FL_{hard} and FL_{soft} (Figure 5.4 (a)). This is because for the weak exchange coupling, the two layers are reversed nearly separately. For stronger exchange coupling (Figure 5.4 (b)) the local minimum disappears, the barrier increases because the reversal occurs for both layers together, with a small offset. In the limit of an infinitely large exchange coupling the barrier can be understood as the one due to a single layer with an intrinsic anisotropy energy density given by [122] and could be written as:

$$K_{uECCFL} = \left(\frac{t_{FL_{soft}}}{t_{ECCFL}}\right) K_{uFL_{soft}} + \left(\frac{t_{FL_{hard}}}{t_{ECCFL}}\right) K_{uFL_{hard}} , \tag{5.2}$$

where the total thickness of the stack is:

$$t_{ECCFL} = t_{FL_{soft}} + t_{FL_{hard}} . \tag{5.3}$$

For $D = 10\,\text{nm}$ in Figure 5.3 (c) and (d), the MEP is by uniform rotation because this D is smaller than the domain wall length, which is similar to Figure 4.4 of [60]. These cases exhibit a behavior similar to that of Figure (a) and (b).

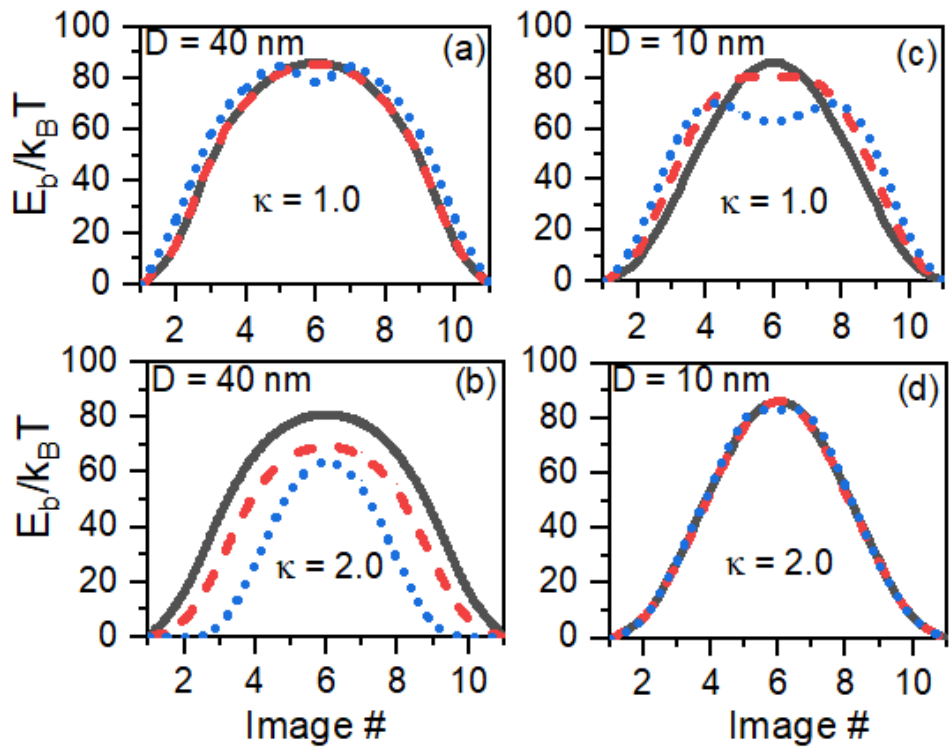

Figure 5.3: Minimal energy path, i.e. energy vs. image #. (a) and (b) are for $t_{FL_{soft}} = t_{FL_{hard}} = 1.2\,\text{nm}$ and $D = 40\,\text{nm}$ with the following curve parameters: ▬ $J_{ex} = 2.0\,\text{erg/cm}^2$, ▬ ▬ $J_{ex} = 0.25\,\text{erg/cm}^2$, and ● ● $J_{ex} = 0.05\,\text{erg/cm}^2$. (c) and (d) are for $t_{FL_{soft}} = t_{FL_{hard}} = 4.0\,\text{nm}$ and $D = 10\,\text{nm}$ with the following curve parameters: ▬ $J_{ex} = 3.0\,\text{erg/cm}^2$, ▬ ▬ $J_{ex} = 1.5\,\text{erg/cm}^2$, and ● ● $J_{ex} = 1.0\,\text{erg/cm}^2$.

5.2.2. Current-induced switching properties

The behavior of J_{c0} in Figures 5.2 (b) and (e) is further explained in Figure 5.4, which shows the STT induced magnetization switching dynamics (for m_z) for the FL_{soft} and FL_{hard} for different J_{ex}. For $D = 40\,\text{nm}$ in Figure 5.4 (a), we find that for small J_{ex} FL_{soft} switches but cannot lead to switching of the FL_{hard} because of the weak coupling. For intermediate J_{ex}, FL_{soft} initiates switching and that induces switching of FL_{hard}. The switching of FL_{soft} is easier than FL_{hard} and hence J_{c0} is smaller. At the same time the exchange coupling is strong enough to also switch FL_{hard}. Once m_z of FL_{hard} changes polarity ($t \approx 20\,\text{ns}$), the anisotropy field assists in driving it towards $m_z \to -1$. In this final stage of reversal, the FL_{hard} magnetization switching precedes that of FL_{soft}.

For large J_{ex}, both FL_{soft} and FL_{hard} switch together with almost identical switching trajectories. We also find that the lateral components of the normalized magnetization m_x of FL_{soft} and FL_{hard} are in phase, with the amplitude of oscillations greater in FL_{soft}, indicating that this is FL_{soft} that induces motion and switching of FL_{hard} via the exchange field. The switching process is by domain wall, which leads to the oscillatory behavior of m_z. For $D = 10\,\text{nm}$ in (b), the dynamics of FL_{soft} and FL_{hard} is similar to the case of $D = 40\,\text{nm}$, but the switching in both layers is mostly by uniform rotation, which is indicated by the absence of oscillations in the m_z time dependence.

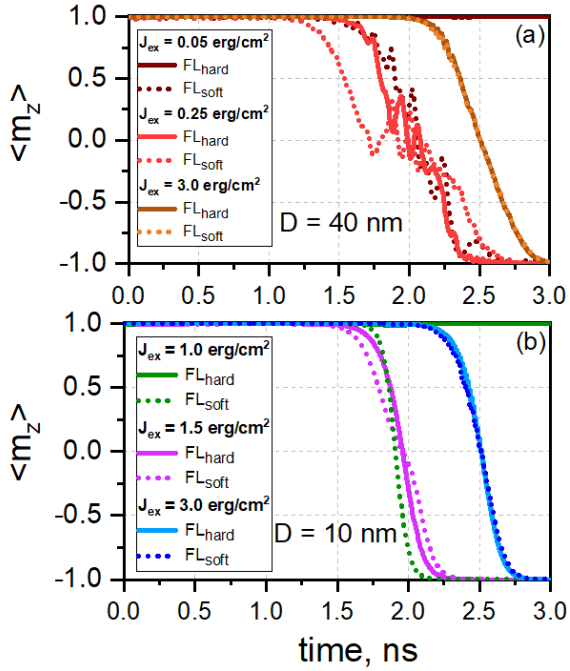

Figure 5.4: Current-induced magnetization switching of p-MTJ with ECC free layer. (a) Average normalized magnetization component m_z vs. time for FL_{soft} and FL_{hard} for different J_{ex} with $\kappa = 2.0$ for $D = 40\,\text{nm}$ and $J_c = 8.5\,\text{MA/cm}^2$ in (a) and $D = 10\,\text{nm}$ in (b) with $J_c = 30\,\text{MA/cm}^2$.

5.3 Advantages of using of p-MTJ with ECC free layer

In this chapter we described the micromagnetic study of the thermal stability and switching properties of p-MTJ with an ECC free layer. The motivation of using the ECC media is similar to the case of magnetic recording media [120,121,123] i.e. the soft layer component would assist in reducing the switching current, while the thermal barrier is maintained at a prescribed value. However, there are also differences. In the recording media case, the thickness of the layers is typically above the domain wall length, so that additional barrier cannot be gained by increasing the thickness further while the switching field is reduced due to the soft layer [120,121,123]. In the MRAM case, the energy barrier would increase by increasing the hard layer thickness if bulk anisotropy materials are used.

However, this possible increase would not increase FOM. Adding a soft layer, on the other hand, can increase FOM while a sufficient energy barrier is insured by the hard layer parameters.

The thermal stability factor and critical switching current density dependent on exchange coupling strength and effective anisotropy ratio between the sublayers. Energy barrier increases with J_{ex} for smaller exchange coupling and saturates for greater values of J_{ex}. The critical switching current has a minimum at an optimal value of J_{ex}. The corresponding FOM has a peak with a significant FOM improvement as compared to a single free layer.

Acknowledgement

Chapter 5, in part, is a reprint of material as appeared in I. Volvach, E. E. Fullerton, and V. Lomakin, “Thermal stability and magnetization switching of composite free layer with perpendicular magnetic anisotropy,” AIP Advances 11, 1 (2021). This work was supported as part of the Quantum-Materials for Energy Efficient Neuromorphic-Computing (Q-MEEN-C), an Energy Frontier Research Center funded by the U.S. Department of Energy, Office of Science, Basic Energy Sciences under Award #DE-SC0019273 and Extreme Science and Engineering Discovery Environment (XSEDE) supported by NSF Grant #ACI-1548562. The dissertation author was the primary investigator and author of the text used in this chapter.

Chapter 6

Perpendicular magnetic tunnel junction with defects and properties distributions

As it was mentioned in previous chapter of this work spin transfer torque (STT) MRAM devices utilizing perpendicular magnetic tunnel junctions (p-MTJs) are the most promising candidates for the future memory application. An important goal in designing p-MTJ devices are reducing the switching current while maintaining a required thermal stability. However, typically in experiment the free layer (FL) of p-MTJ have the edge and surface roughness. It is important to predict the behavior of the p-MTJ stack in the presence of surface roughness.

This chapter presents a micromagnetic study for p-MTJ's FL with edge and surface defects. The study includes the switching current, energy barrier, and efficiency as functions of the edge and surface roughness amplitude. We also provide a detailed study of minimal energy path and current induced magnetization switching as a function of the various surface and edge roughness size. We show that the presence of edge/surface defects

can lead to worthening of the switching properties, particularly in the regime in which the magnetization dynamics is spatially non-uniform. We also discuss the granularity and parameters distributions in p-MTJ stack and its operation at zero and room temperatures.

6.1 p-MTJ with edge roughness

We consider a circularly cylindrical stack of diameter D as shown on the Figure 6.1 (a). The stack includes a standalone FL with reference layer exchange coupled to a synthetic antiferromagnetic layer. FL has a thickness t_{FL}, saturation magnetization M_{sFL} and perpendicular volumetric uniaxial anisotropy K_{uFL}. The reference layer RL and synthetic antiferromagnetic layers SAF are compensated in that the magnetostatic field generate by them and averages the free layers is zero. We define σ as the mean value of FL edge roughness amplitude as shown on Figure 6.1 (b). The illustration of the edge roughness amplitude is shown on Figure 6.1 (c). We consider the maximum edge roughness value up to 6 nm. For the current induced switching simulations, we assume the spin transfer torque (STT) via Slonczewski's models at the bottom surface of FL with the current I_c. The presented simulations are accomplished using a finite-element-based micromagnetic simulator FastMag. FastMag allows computing the magnetization dynamics by solving the Landau–Lifshitz–Gilbert equation. It also allows computing the energy barrier by using the nudged-elastic-band (NEB) method, which finds a set of magnetization states (images) associated with energies along the minimal energy path (MEP). For the critical switching current definition, the eigen value solver was used. The eigen value solver allows a very accurate calculation of the critical switching current compared to the common

approaches based on infinite pulse.

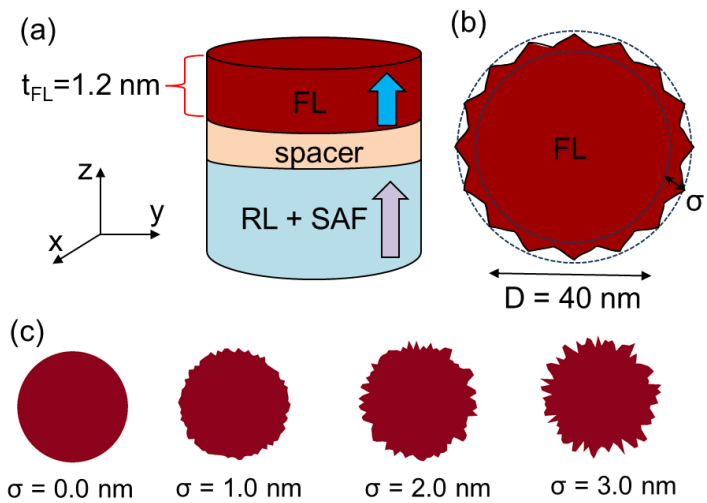

Figure 6.1: p-MTJ stack: (a) including free layer FL and SAF reference layers. (b) FL with edge roughness (c) random edge roughness representation of p-MTJ FL for different roughness radius σ.

The key parameters considered are the normalized energy barrier $\Delta = E_b / k_B T$, where E_b is the energy barrier between the up and down or down and up states as determined by the NEB method, k_B is Boltzmann's constant, and temperature $T = 300\,\mathrm{K}$ and $FOM = E_b / I_{c0}$. Figure 6.2 (a) shows the minimal energy for the FL of p-MTJ for the case without edge roughness. For the case of edge roughness, the MEP was not significantly affected Figure 6.2 (b).

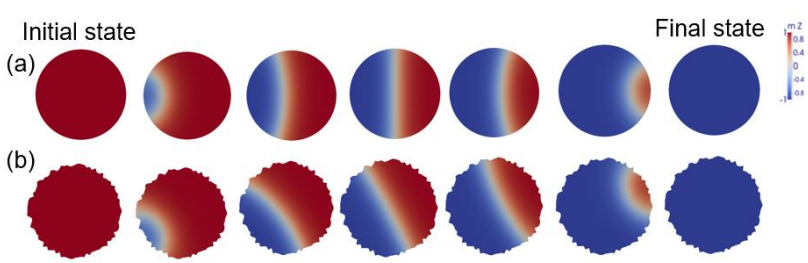

Figure 6.2: Snapshots of m_z magnetization component of the minimal energy path for p-MTJ stack: (a) without edge roughness, (b) with edge roughness of 2 nm.

Figure 6.4 (a) shows that the thermal stability factor is not changing for the case of edge roughness with small amplitude, i.e. $\sigma \leq 2.0\,\text{nm}$. This could be explained by the fact that the amplitude of the roughness in practice is relatively small to affect the MEP. However, when $\sigma > 2.0\,\text{nm}$ (Figure 6.4 (a)) the thermal stability factor decreases due to decrease of effective anisotropy of the FL that is affected by the edge roughness.

Figure 6.3 (a) and (b) shows the current-induced magnetization switching of the p-MTJ with edge roughness. The presence of the edge roughness changes the magnetization behavior of FL during the switching. Figure 6.3 (a) demonstrates the start of the switching from the center of FL, whereas Figure 6.3 (b) the current-induced switching starts from the edge of FL. This could be explained that the switching current is associated with local effect in FL and the switching starts where the magnetostatic field is the highest. The edge roughness creates the higher magnetostatic field at the edges of FL compared to the center of FL. The switching current increases with increase of the edge roughness amplitude due to the possibility of the "pinning" of the domain wall in the FL by the edge roughness (Figure 6.4 (b)).

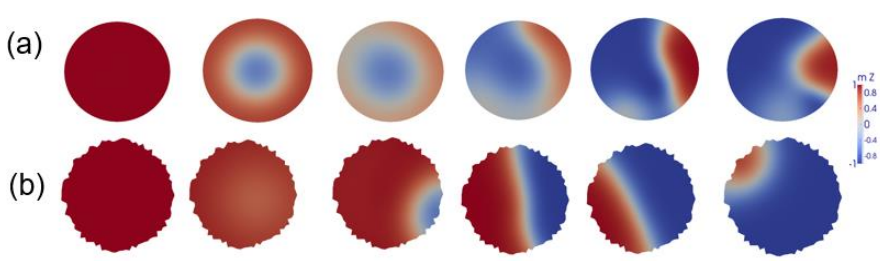

Figure 6.3: Snapshots of m_z magnetization component of the current-induced switching of p-MTJ stack: (a) without edge roughness, (b) with edge roughness of 2 nm. The applied current $I_c = 2.0\,\mu\text{A}$.

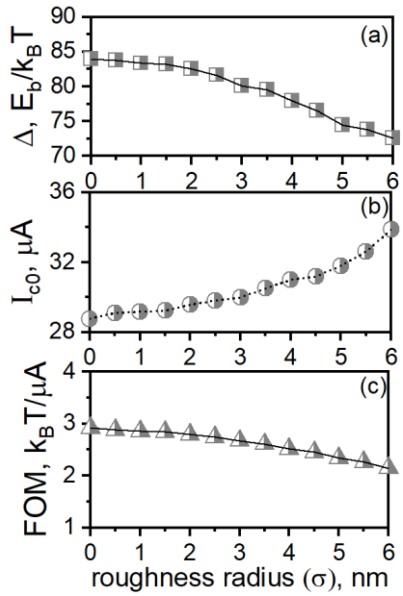

Figure 6.4: (a) Δ, (b) I_{c0}, (c) FOM vs. edge roughness radius σ for $M_{sFL} = 1200\,\mathrm{emu/cm^3}$, $K_{sFL} = 1.088\,\mathrm{erg/cm^2}$, $A_{ex} = 10^{-6}\,\mathrm{erg/cm}$, $\alpha = 0.008$, $t_{spacer} = 1\mathrm{nm}$.

Figure 6.4 (c) shows the FOM as a function of edge roughness amplitude $\sigma \le 2.0\,\mathrm{nm}$. The efficiency (FOM) of p-MTJ decreases when the roughness amplitude increases. and (b) shows the current-induced magnetization switching of the p-MTJ with edge roughness.

6.2 p-MTJ with surface roughness

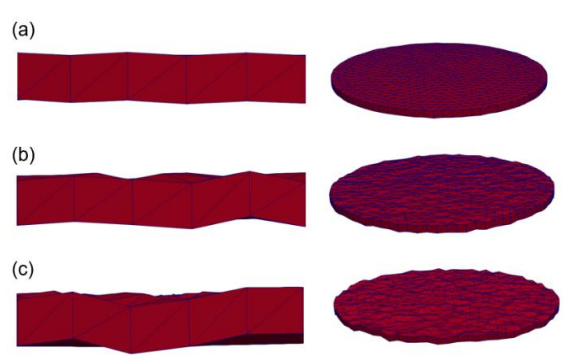

Figure 6.5: Micromagnetic representation of p-MTJ FL layer with surface roughness: (a) random surface roughness with 0.05 nm amplitude, (b) random surface roughness with 0.15 nm amplitude. FL with edge roughness (c) random surface roughness with 0.25 nm amplitude.

Figure 6.5 shows the representation of the surface roughness for p-MTJ's FL. For micromagnetic modeling of the surface roughness the thickness of FL was considered constant. Figure 6.6 shows the behavior of the thermal stability, average magnetostatic field, critical switching current and efficiency as a function of surface roughness. The surface roughness increases the stability of FL due to decrease of the demagnetization field (Figure 6.6 (b)). With stability increasing the critical switching current is also increases and the overall efficiency of the device decreases.

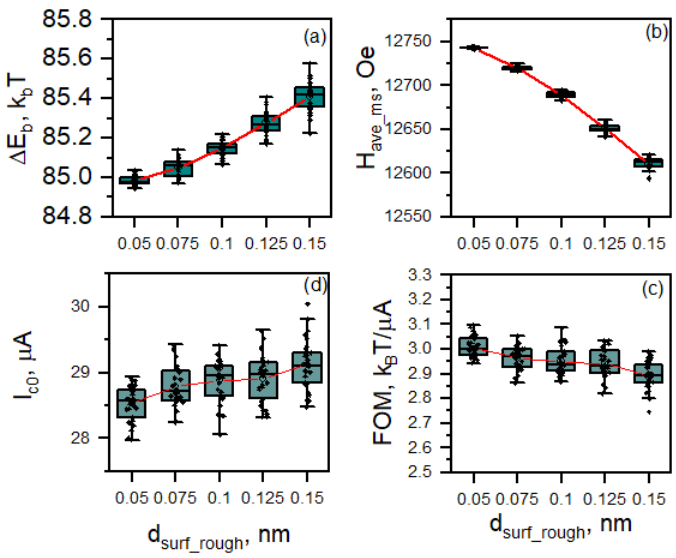

Figure 6.6: (a) Δ, (b) H_{ave_ms}, (c) I_{C0}, (d) FOM vs. surface roughness amplitude d_{surf_rough} for $M_{sFL} = 1200\,\text{emu/cm}^3$, $K_{sFL} = 1.088\,\text{erg/cm}^2$, $A_{ex} = 10^{-6}$ erg/cm, $\alpha = 0.008$, $t_{spacer} = 1\,\text{nm}$.

6.3 Granular free layer in p-MTJ

Figure 6.7 shows the granular representation of the FL of p-MTJ. The grain representation is based on Voronoi tessellation method [124] that allows relatively well modeling of the actual magnetic granular media. Each color in Figure 6.7 represents different properties of each grain. In this section we show the behavior of the granular FL

as a function of intergranular exchange coupling energy density J_{ex} for with/without material parameters distribution. We define σ_{H_k} as anisotropy field distribution in % between the grains from the given mean value H_k. We studied the thermal stability and critical switching current for both $\sigma_{H_k} = 0$ and $\sigma_{H_k} \neq 0$. We also show the behavior of the granular FL under zero and room temperatures.

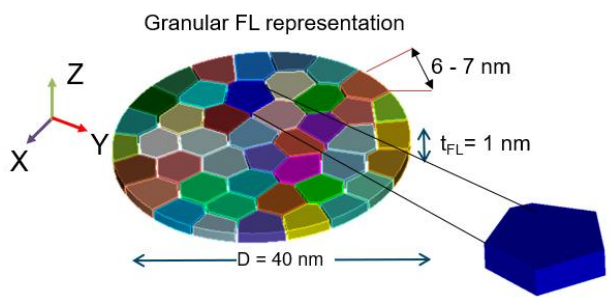

Figure 6.7: Illustration of granular FL of p-MTJ. Different grain color associated with different H_k in each grain within the granular FL.

6.3.1 Granular free layer at zero temperature

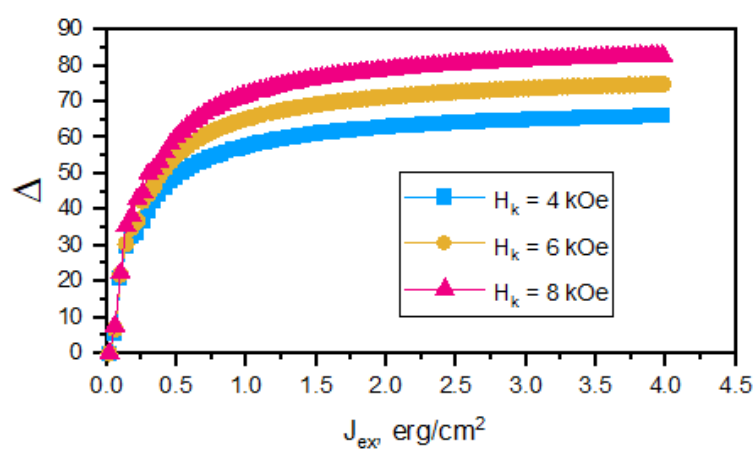

Figure 6.8: Thermal stability factor as a function of the exchange coupling constant J_{ex} between the grains for different H_k of granular FL of p-MTJ.

Figure 6.8 shows the thermal stability factor of FL as a function on intergranular exchange coupling J_{ex}. The thermal stability factor Δ has non-linear

dependence vs. J_{ex} for different uniaxial anisotropy field H_k. The thermal stability factor Δ increases for higher H_k. For small exchange coupling, i.e. $0.1 < J_{ex} < 1.0\,\mathrm{erg/cm^2}$, Δ increases up to some saturation value associated with maximum value and for $J_{ex} > 1.0\,\mathrm{erg/cm^2}$ Δ is independent on J_{ex}. For $0.1 < J_{ex} < 1.0\,\mathrm{erg/cm^2}$ the grains in FL are weakly coupled and the overall thermal stability factor exhibits an average for all the grains and depends on H_k of a single grain. For relatively high $J_{ex} > 1.0\,\mathrm{erg/cm^2}$ the grains in FL are well coupled, and FL exhibits the continuous solid FL behavior.

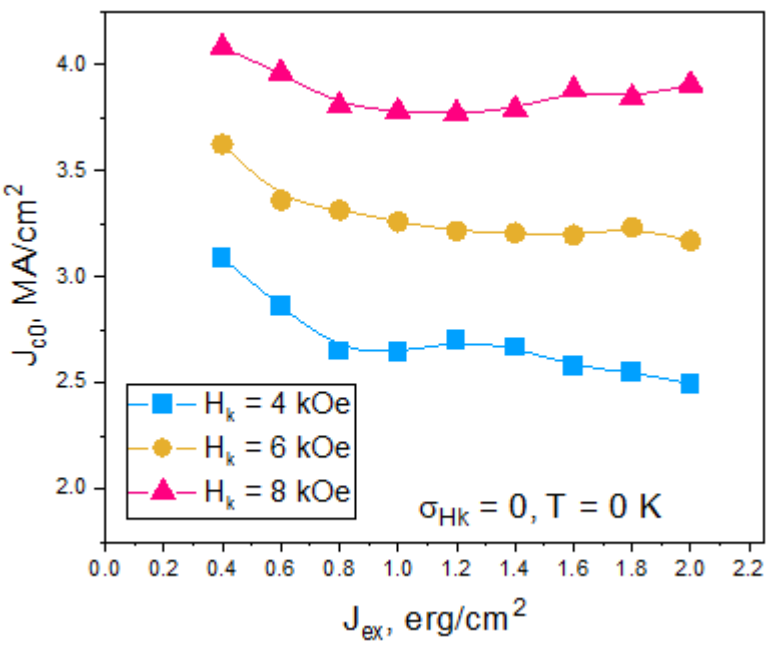

Figure 6.9: Critical switching current density at $T = 0\,\mathrm{K}$ vs. J_{ex} for different H_k values and without distribution in the grains $\sigma_{H_k} = 0\%$. All the grains within FL have the same value of H_k.

Figure 6.9 shows the critical switching current at $T = 0\text{K}$ of granular FL as a function on intergranular exchange coupling J_{ex}. The critical switching current is higher when the grains are weakly coupled because the switching happens grain by grain as shown on Figure 6.10 (a). For a strong exchange coupling the switching of granular FL happens via domain wall (Figure 6.10 (b)) and results in lower switching current density.

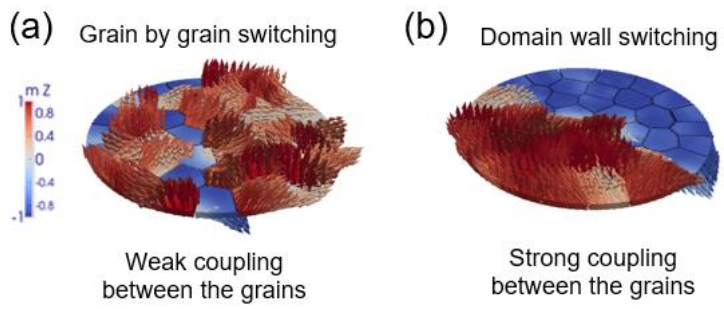

Figure 6.10: Current induced switching of the granular FL: (a) non-uniform separate grain switching for $J_{ex} = 0.4\,\text{erg}/\text{cm}^2$, (b) Domain wall switching for $J_{ex} = 1.0\,\text{erg}/\text{cm}^2$.

6.3.2 Granular free layer at room temperature

The write process in an STT-RAM bit is inherently stochastic due to thermal fluctuations, which give rise to a distribution of the magnetization of the free layer both before and during switching. As a result, the time taken by the bit to switch has a wide distribution. In real life the devices are operating at a room temperature $T = 300\text{K}$ and it is necessary to predict the switching behavior of granular FL of p-MTJ under the effect of thermal fluctuations. Write error rates (WER) method is briefly discussed in section 3.3.3 and that correspond to the applied current failing to correctly switch the magnetization in the free layer. As shown in section 2.5, NEB can be an efficient method to compute energy barriers from which this thermal stability can be assessed. However, it is not enough to

have the full picture. Indeed, the behavior of a device under the influence of a thermal fields depends not only on the shape of the energy landscape in the magnetic configuration space, but also on the type of reversal process involved. Figure 6.11 shows WER behavior for granular p-MTJ's FL as a function of intergranular exchange coupling energy density J_{ex} for the same material parameters of the grains.

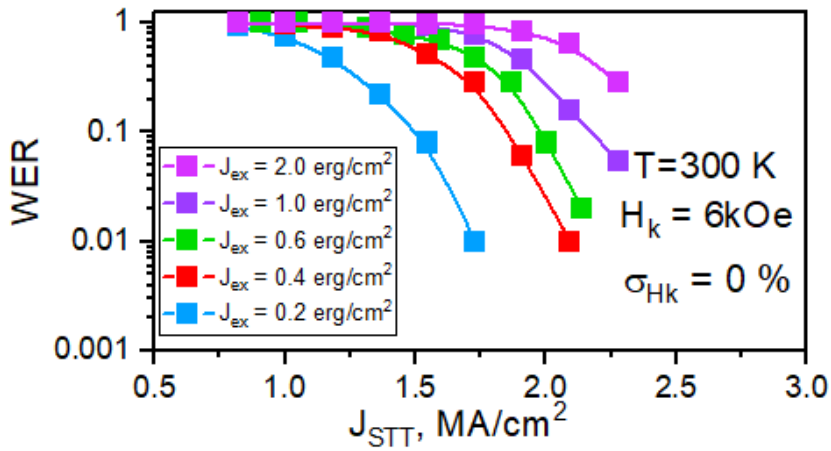

Figure 6.11: Write error rate vs J_{ex} for granular FL of p-MTJ at $T = 300\,\mathrm{K}$. The switching current pulse width was $P_{sw} = 8\,\mathrm{ns}$.

Granular free layer at room temperature and material properties distribution.

We have already discussed the behavior of the granular FL without any material properties distribution at $T = 300\mathrm{K}$. It is important to mention that the magnetic granular FL might consist of different grains with different material parameters, such as: magnetic anisotropy, damping constant, exchange coupling, saturation magnetization, etc. The grains could have different physical sizes which might affect the efficiency of the device during switching process. Here, we consider the FL with nearly same grain's size (Figure 6.7) with distribution of the anisotropy field H_k between the grains in FL. Figure 6.12 shows the

example of distribution of H_k vs distribution coefficient σ_{H_k} given in %. Figure 6.13 shows WER at $T = 300\text{K}$ for granular FL for different σ_{H_k} and two different mean values of H_k. We consider exchange coupling energy density $J_{ex} = 0.6\,\text{erg}/\text{cm}^2$ between the grains. Figure 6.13 (a) shows WER for $H_k = 4000\,\text{Oe}$ and different σ_{H_k}. The critical switching current density is increases since with increase of σ_{H_k} and WER curves moves to the right side. This is because for higher σ_{H_k} there are grains with very high and very low H_k which makes the switching not efficient compared to the case when the grains have the same properties. For $H_k = 6000\,\text{Oe}$ (Figure 6.13 (b)) the WER is not affected by the distribution of H_k and the critical switching current density stays the same.

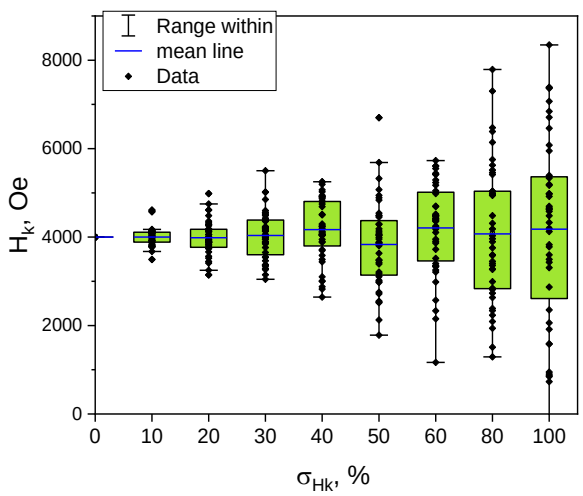

Figure 6.12: Illustration of anisotropy field H_k distribution in granular FL with distribution constant σ_{H_k}.

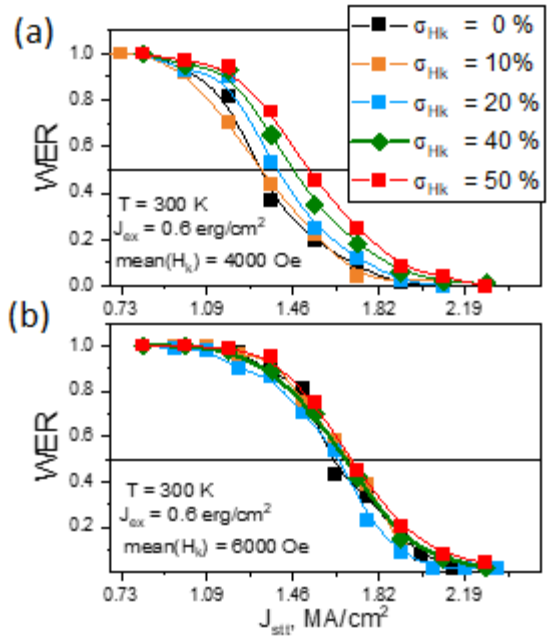

Figure 6.13: WER at $T = 300\,\mathrm{K}$ for granular FL of p-MTJ with anisotropy field distribution in the FL's grains. The switching current pulse width was $P_{sw} = 8\,\mathrm{ns}$.

In this chapter we considered the p-MTJ's FL with edge and surface roughness. In general, the presence of physical roughness in FL might lead to the worthening of the p-MTJ device performance. The edge roughness slightly affected the performance of the FL and the efficiency of the device dropped by ~3% compared to FL without any edge roughness. For the FL with surface roughness the thermal stability factor Δ increased by 3 % due to average demagnetization field drop which led to increase of the critical switching current I_{c0} by 6 % and the FL overall efficiency decreased by ~ 4% depending on the surface roughness amplitude. We also considered the effect of granularity in FL of p-MTJ with and without anisotropy field distribution in the grains for both zero and room temperatures. For granular FL the intergranular exchange coupling energy density J_{ex} plays an important role. For low $0.1 < J_{ex} < 1.0\,\mathrm{erg/cm^2}$ the minimal anergy path and current-

induced switching behavior depends on the properties of each separate grain in FL. For stronger $J_{ex} > 1.0\,\mathrm{erg/cm^2}$ the device behaves similar to continuous FL that discussed in previous chapters.

Acknowledgement

Chapter 6, in part, is a reprint of material as appeared in I. Volvach, Z. Lin and V. Lomakin, “Perpendicular magnetic tunnel junction with edge and surface roughness and material distribution” currently being prepared for submission. The dissertation author was the primary investigator and author of this material.

Chapter 7

Magnetic spin-torque oscillator

This chapter discusses antiferromagnetically exchange coupled composite (soft/hard) spin torque oscillator (AF-ECC STO). For the AF-ECC STO we demonstrate its operation via an analytical model and micromagnetic analysis. The operation mechanism is based on the exchange field due to the antiferromagnetic coupling between soft and hard sub-layers of the free layer as well as on the easy-plane anisotropy of the soft sub-layer. AF-ECC STO can generate large amplitude magnetization oscillations, which can be tuned over a broad frequency range with precessions mostly generated by the soft layer. We also demonstrate that AF-ECC STO offers a flexibility in current control of the oscillation frequency and magnetization angle for realistic material parameters.

7.1 Antiferromagnetically exchange coupled composite STO

Conventional STOs based on a ferromagnetic free layer have several limitations (section 3.6), such as their highest frequency, which is limited by the saturation

magnetization and anisotropy energy density, as well as the general need to have an applied field for a steady precession or to maintain stability and modulate the oscillation frequency range. There are modified STO configurations that can result in increased precession frequency. In particular, recent reports include theoretical studies based on macrospin models that show that STOs based on an antiferromagnetic free layer (FL) can operate at up to THz frequencies [73,77-79,89-92]. Similar ideas can be extended to using synthetic antiferromagnetic (AF) FLs [73,89-91] and discussed in section 3.6 of this work. Reported work [92] using a macrospin approximation showed that synthetic AF free layer can result in high-frequency oscillations due to strong AF exchange. However, such STO configurations have limitations, including a need for an impractically strong AF coupling, lack of a generated microwave field, small precession angle, and narrow frequency/current range of operation.

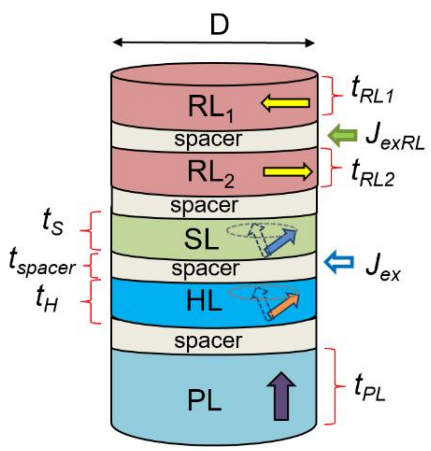

Figure 7.1: AF ECC STO structure.

The AF-ECC STO is shown in Figure 7.1. The FL of the AF-ECC STO is composed of a soft sub-layer (SL) and a hard sub-layer (HL) that are AF coupled through their

surfaces with the surface exchange energy density J_{ex}. The SL and HL, respectively, have a thickness of t_s and t_h, saturation magnetization $M_{s,s}$ and $M_{s,h}$, perpendicular uniaxial anisotropy energy density $K_{u,s}$ and $K_{u,h}$, damping constants α_s and α_h, and exchange constants A_s and A_h. In addition to the FL with SL and HL, the stack includes a polarizing layer (PL) having t_{PL}, $M_{s,PL}$, and $K_{u,PL}$ as well as an AF-coupled read layer (RL) consisting of two sublayers, RL_1 and RL_2, having $t_{RL1} = t_{RL2}$ and $K_{u,h} = K_{RL1}$, which are AF coupled with J_{exRL}. The magnetic layers are separated by spacer layers.

The motivation for the AF-ECC structure is to allow for a tunable precession operation at high frequencies and realistic values of the material and structural parameters, including J_{ex}. The operation of the AF-ECC STO is based on the interplay between the effective anisotropy and AF exchange interactions. $K_{u,h}$ is chosen high to maintain a perpendicular effective anisotropy in HL needed for driving SL. On the other hand, $K_{u,s}$ is chosen low such that the FL effectively has an easy-plane anisotropy, which allows driving its large-amplitude precession via the AF exchange. The PL has a perpendicular anisotropy that is greater than that of the HL to keep it mostly fixed. The magnetostatic fields from the polarizing layer are not compensated, i.e., there is no an AF coupled sublayer to cancel the magnetostatic field from the polarizing layer as often is done for MTJs used in MRAM [62,66,125]. The reason for using a single PL is that the effect of the magnetostatic field from PL has an insignificant effect on the STO precession and so there is no need in adding an extra layer. The PL has a perpendicular anisotropy that is greater than that of the HL. The role of the RL is to generate an electric signal by means of tunnel magnetoresistance

(TMR). The RL is magnetized in-plane (in the *x*-direction) and the TMR is related to the x-direction of the magnetization in the SL. The values of J_{ex} and J_{exRL} are chosen based on experimental results of using Ru and Ir as AF coupling interlayer material [14,126-128].

7.2 Theoretical model of AF-ECC STO

To explain the operation of AF-ECC STO, we first consider a two-spin model, assuming spatially uniform magnetization states in the soft and hard layers, which are expected to be valid for smaller STOs. We, then, show results of micromagnetic simulations of structures of larger sizes with possibly non-uniform dynamics.

In the two-spin approximation, the dynamics can be described by the Landau-Lifshits-Gilbert (LLG) [18,19] equation for the two magnetization states

$$\frac{d\mathbf{m}_\xi}{dt} = -\gamma(\mathbf{m}_\xi \times \mathbf{H}_\xi^{eff} + \alpha \mathbf{m}_\xi \times \mathbf{m}_\xi \times \mathbf{H}_\xi^{eff}), \quad (7.3)$$

Here, γ is the gyromagnetic ratio, $\mathbf{m}_\xi$ is the normalized magnetization, and $\mathbf{H}_\xi^{eff}$ is the effective field, including the spin-transfer torque (STT), exchange field, and effective anisotropy fields:

$$\mathbf{H}_\xi^{eff} = \beta_\xi \mathbf{m}_\xi \times \mathbf{p} + \frac{J_{ex}}{d_\xi M_{s,\xi}} \mathbf{m}_\varsigma + H_{K,\xi}^{eff} m_{z\xi} \hat{\mathbf{z}}. \quad (7.4)$$

The subscript ξ is for HL ($\xi = h$) or SL ($\xi = s$) and the subscript ς is for the other layer, i.e., for $\xi = h$ the value of $\varsigma = s$ and vice versa. The STT component (the first term in the equation 7.4 is present only for HL, i.e., $\beta_s = 0$. For the STT term in HL, $\hat{\mathbf{p}}$ is the magnetization of the polarizing layer, which is assumed to be perpendicular, i.e., $\hat{\mathbf{p}} = \hat{\mathbf{z}}$. STT parameter determining the effective STT field strength is defined as:

$$\beta_h = \frac{J\eta\hbar_e}{2eM_{s,h}\delta_h}, \tag{7.5}$$

where J is the electric current density, η is the spin transfer torque efficiency, $\hbar$ is reduced Planck's constant, e is the electron charge, and δ_h is the HL thickness. The effective anisotropy field could be represented as:

$$H_{K,\xi}^{eff} = H_{K,\xi} - \pi M_{s,\xi}^2 \left(\frac{3N_z}{4\pi} - 1 \right), \tag{7.6}$$

and is the given in terms of the intrinsic anisotropy field which could be written as:

$$H_{K,\xi} = \frac{2K_{u,\xi}}{M_{s,\xi}}. \tag{7.7}$$

In Eq. 7.6 the demagnetization factor N_z is represented in [10] and in chapter 2 of this work; for the material parameters chosen, $H_{K,s}^{eff} < 0$ and $H_{K,h}^{eff} > 0$. The magnetostatic interactions between the layers have only small quantitative effects.

The LLG equation 7.4 describes the initial dynamics and the steady state precession. The steady state precession can also be characterized by considering the azimuthal (φ) and elevation (θ) components of the torques. The dominant torques can be explicitly given:

$$\begin{aligned} &T_{\varphi\xi}^{ex} = -\frac{J_{ex}}{d_\xi M_{s,\xi}} \sin(\theta_h + \theta_s);\ T_{\varphi\xi}^{an} = \frac{H_{K,\xi}^{eff}}{2} \sin(2\theta_\xi), \\ &T_{\theta\xi}^{ex} = \frac{J_{ex}}{d_\xi M_{s,\xi}} \sin(\phi_\xi - \phi_\zeta) \sin\theta_\zeta - \alpha T_{\varphi\xi}^{ex};\ T_{\theta\xi}^{an} = -\alpha T_{\varphi\xi}^{an}, \\ &T_{\theta h}^{stt} = \beta_h \sin\theta_h. \end{aligned} \tag{7.8}$$

where θ_s and θ_h are the elevation angles of the magnetization in HL and SL, and the azimuthal relative angle ϕ between the magnetizations in HL and SL. The angles θ_s, θ_h, and ϕ are constant as a function of time during the precession. The rest of the torques can

be neglected assuming small α. The elevation angles θ_s and θ_h have an important role in determining the torques and in determining the magnetization magnitude of the precession in SL and HL. The relative azimuthal angle ϕ has an important role in determining the elevation torque $T_{\theta\xi}^{ex}$ and in the non-uniform magnetization behavior in larger structures, as shown in the micromagnetic analysis.

The angles θ_s, θ_h, and ϕ can be found as solutions of the following system of equations:

$$\begin{aligned} &T_{\theta h}^{ex} + T_{\theta h}^{an} + T_{\theta h}^{stt} = 0, \\ &T_{\theta s}^{ex} + T_{\theta s}^{an} = 0, \\ &f = \frac{\gamma(T_{\varphi h}^{ex} + T_{\varphi h}^{an})}{\sin\theta_h} = \frac{\gamma(T_{\varphi s}^{ex} + T_{\varphi s}^{an})}{\sin\theta_s}. \end{aligned} \tag{7.9}$$

where the two equations in the first row represent balancing the elevation torques needed for a sustained precessional orbit and the last equation represents the fact that the precessional frequency f in HL and SL is the same.

7.3 Study of the AF-ECC STO operation

In this section, we study the operation of the AF-ECC STO assuming the simplified model, which includes the SL and HL of the FL (as in the inset of Figure 7.2). The study incudes the zero- and room temperature operation. We also show that the operation of the full stack of Figure 7.1 is not altered significantly by the presence of the rest of the stack layers.

7.3.1 Operation at zero temperature

Figure 7.3 shows m_z in the HL and SL for three values of J_{ex} as a function of J. The two values are chosen based on experimental results of using Ru and Ir as AF coupling interlayer material [14,126-128]. From Figure 7.3 (a), for a given J_{ex}, f increases with J and reaches the maximal value $f_{\max}$ when θ_s and θ_h approach π. From the analysis of Equations 7.8 and 7.9, $f_{\max}$ can be approximated by:

$$f_{\max} = -\gamma \left(\frac{2J_{ex}}{d_s M_{s,s}} + H_{K,s}^{eff} \right) \tag{7.10}$$

when assuming that the maximal frequency is obtained for $\theta_s = \theta_h = \pi$. From here, the maximal frequency depends on both $H_{K,s}^{eff}$ and J_{ex}, and it can reach values of several hundreds of GHz for large J_{ex} and $H_{K,s}^{eff}$. From Figure 7.3 (b), for smaller J_{ex}, the magnetization of SL has a much greater in-plane component, i.e., it generates a much stronger external magnetic field than that of the HL. With an increase of J, m_z of the SL changes its sign from being opposite to the HL direction to the same direction and with a further increase of J, the magnetization of SL approaches the perpendicular direction together with that of HL. For greater J_{ex}, the magnetization of both the HL and SL are mostly in plane for small J and both approach the perpendicular direction for larger J. From Figure 7.2 (c), the angle φ increases with J and decreases with J_{ex}.

To understand the behavior in Figure 7.2 and demonstrate the role of different magnetic interactions, Figure 7.3 shows the azimuthal and elevation torques for the case of $J_{ex} = -0.4\,\mathrm{erg/cm^2}$. As explained in the model of Eqs. 7.8 and 7.9, the elevation torques

should balance to zero to maintain a steady-state precession.

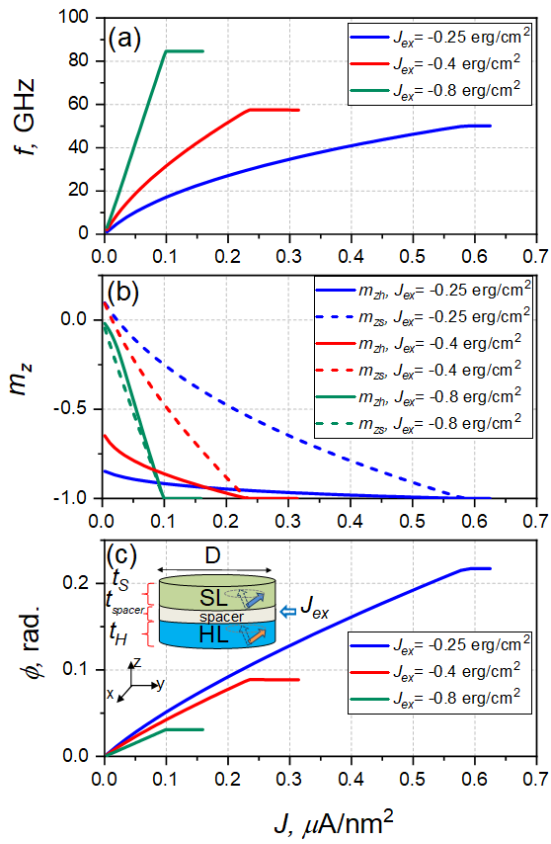

Figure 7.2: Inset shows the AF-ECC STO structure. The results obtained via the 2-spin model are shown for (a) f, (b) m_z, and (c) φ as functions of J for different exchange coupling J_{ex} for $D = 20\,\text{nm}$, $t_h = t_s = 0.8\,\text{nm}$, $t_{spacer} = 0.3\,\text{nm}$, $M_{s,s} = 1350\,\text{emu/cm}^3$, $M_{s.h} = 470\,\text{emu/cm}^3$, $K_{u,h} = 4\,\text{Merg/cm}^3$, $K_{u,s} = 1.11\,\text{Merg/cm}^3$, $\alpha_h = \alpha_s = 0.008$.

From Figure 7.3 (a), the elevation torques in the HL are dominated by the exchange and STT components, which are of an opposite sign maintaining the torque balance. The anisotropy elevation torque component in the HL is relatively insignificant. For the SL (Figure 7.3 (c)), the elevation torques are dominated by the exchange and effective anisotropy components**,** which are again of an opposite sign maintaining the balance. The exchange elevation torques in the SL and HL have an opposite sign, which explains the

same sign of m_z in the HL and SL as shown in Figure 7.2 (a). The azimuthal torques (Figures 7.3 (b) and 7.3 (d)) are dominated by exchange and anisotropy components, whereas the STT component is subdominant. The reason for the weak STT contribution is related to the fact that the main role of STT is to overcome the system damping given by α, which is small. The azimuthal anisotropy and exchange torques in the HL (Figure 7.3 (b)) have an opposite sign with the exchange torque dominating. In the SL (Figure 7.3 (d)), the azimuthal exchange and anisotropy torques are of the same sign and thus they are added to results in the total azimuthal torque. In the steady state, the total azimuthal scaled torques in the HL and SL are the same and they match the precessional frequency in Figure 7.2 (a), in agreement with the two-spin model of Eqs. 7.8 and 7.9.

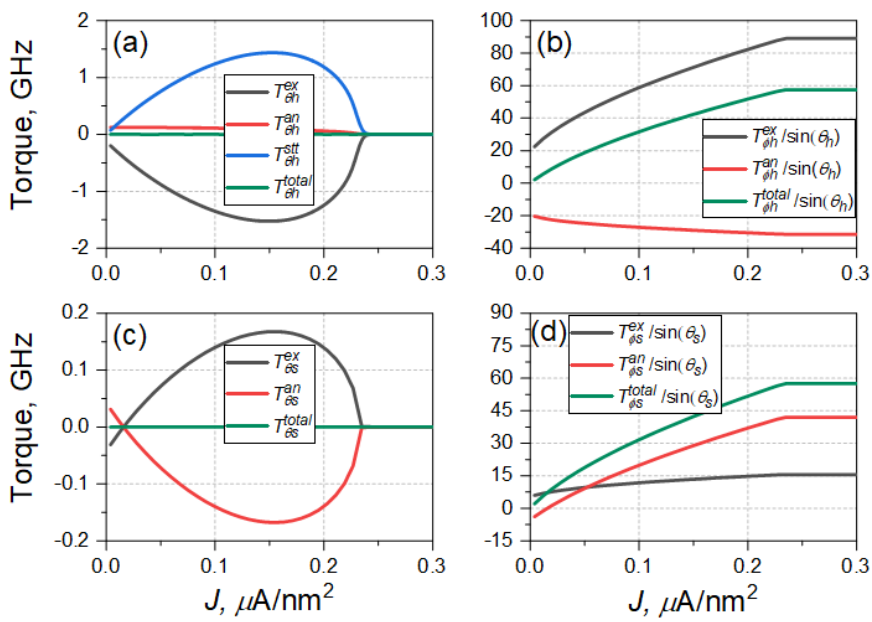

Figure 7.3: (a) and (c) elevation torques in HL and SL; (b) and (d) azimuth torques in HL and SL. The torques are given for $J_{ex} = -0.4\,\mathrm{erg/cm^2}$ in the units of GHz, i.e., they are obtained by multiplying the actual torques by γ.

We also studied the effect of different α_h and α_s, and found that an increase of α_h and α_s leads to an increase of the required J. The major increase of the required J is due to α_s, e.g., to maintain the same f with a double value of α_s, J needs to be almost doubled. On the other hand, an increase in α_h has an insignificant effect on the required J. This behavior is because $T_{\theta s}^{ex}$ needs to increase to compensate an increase in $T_{\theta s}^{an}$ due to an increased α_s, which, in turn, leads to an increase in $T_{\theta h}^{ex}$ and $T_{\theta h}^{an}$ required for the elevation torque compensation, and hence an increase of J. Noting that, typically, soft materials have lower damping constants this behavior constitutes an added benefit [119].

We next show results of micromagnetic simulations obtained using the finite element based micromagnetic simulator FastMag [113].

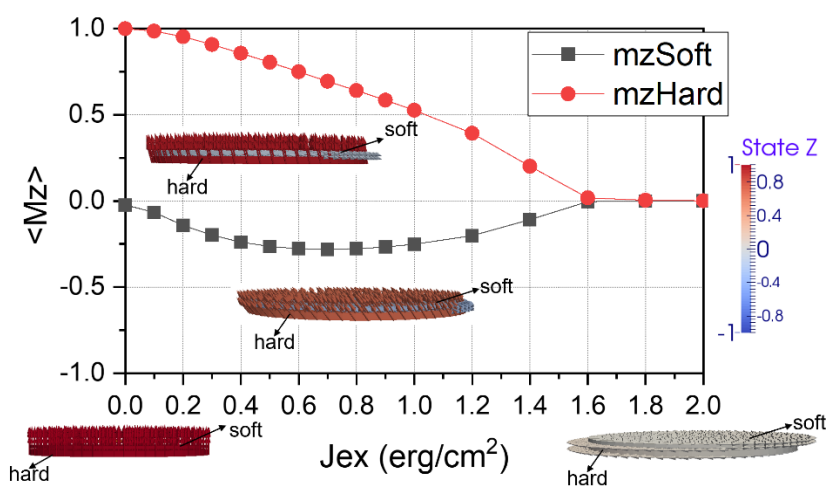

Figure 7.4: Magnetization orientation vs J_{ex} for HL and SL for the AF-ECC STO structure.

Figure 7.4 shows the micromagnetic simulations for the orientation of the magnetization for HL and SL of the AF-ECC STO as a function of J_{ex} at $J = 0$. The

increase of the exchange interaction constant J_{ex} leads to in-plane orientation of both HL and SL.

We considered STOs of different sizes and found that the behavior of smaller STOs ($D < 10\,\text{nm}$) is nearly identical to the two-spin model in Figures 7.3 and 7.4, whereas for larger sizes the behavior has more complicated features resulting from magnetization non-uniformities. Figure 7.5 shows micromagnetic results for the same parameters as in Figure 7.2 for $D = 20\,\text{nm}$ and $40\,\text{nm}$ with $J_{ex} = -0.4\,\text{erg}/\text{cm}^2$ and Figure 7.6 shows the magnetization states corresponding to different responses in Figure 7.5.

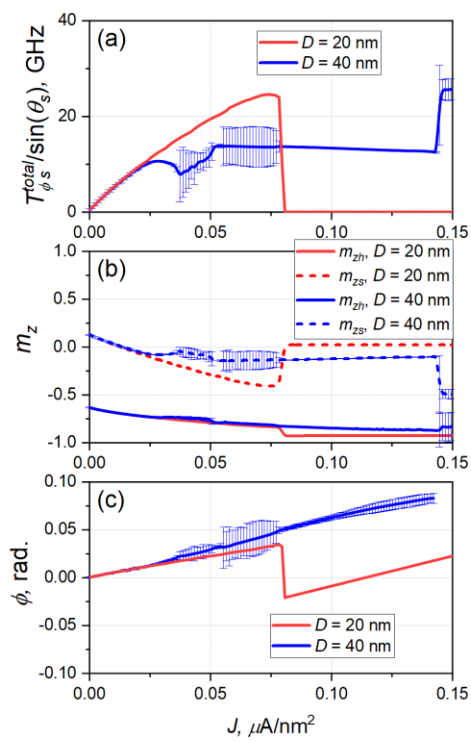

Figure 7.5: Micromagnetic results for (a) the average scaled torque $T^{total}_{\varphi s}/\sin\theta_s$, which approximates the precessional frequency f, (b) averages m_z in HL and SL, and (c) averaged φ as a function of J for $J_{ex} = -0.4\,\text{erg}/\text{cm}^2$ for two values of $D = 20\text{nm}$ and $40\,\text{nm}$. The rest of the parameters are as in Figure 7.2 and $A_s = A_h = 1\mu\text{erg}/\text{cm}$. The bars represent the value spread for a given J.

For smaller J the behaviors of all parameters in Figure 7.6 are close to those for the two-spin model in Figure 7.3 and the precession of the AF-ECC STO is nearly uniform (Figure 7.6 (a)). For greater J the behavior deviates. For the smaller size of $D = 20\,\text{nm}$, with an increase of J, the precession becomes more non-uniform (Figure 7.6 (b)). At a certain J ($J = 0.15\,\mu\text{A}/\text{nm}^2$), the magnetization of the SL goes into a vortex state (Figure 7.6 (c)), the magnetization of the HL is mostly out of plane, and the precession stops. This behavior can be explained by the azimuthal angle ϕ in Figure 7.5(c) (and Figure 7.2(c)), i.e., for greater J, ϕ increases and it leads to an increased exchange torques that, in turn, leads to the magnetization twisting resulting in the vortex state. For the greater size, $D = 40\,\text{nm}$, and greater J, the precession becomes more non-uniform. The parameters in Figure 7.6 have deviations in certain ranges and for larger J (for $J = 0.09\,\mu\text{A}/\text{nm}^2$) the precession becomes highly non-uniform and sporadic.

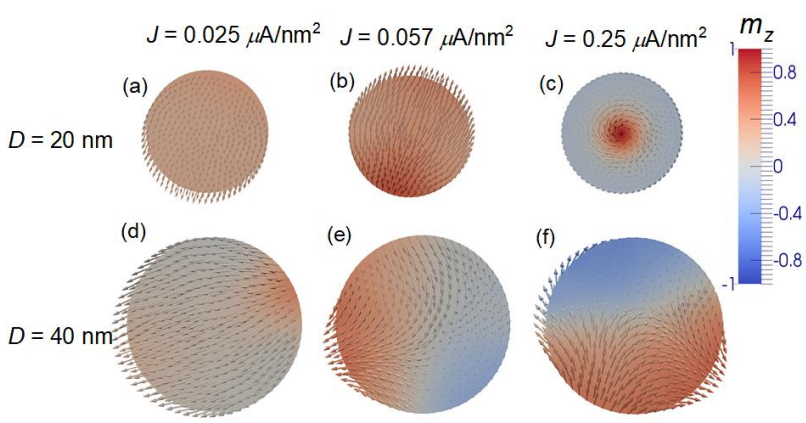

Figure 7.6: Snapshots of m_z of SL for $J_{ex} = -0.4\,\text{erg}/\text{cm}^2$ for $D = 20\,\text{nm}$ and $40\,\text{nm}$ for different J. The rest of the parameters are as in Figures 7.3 and 7.6.

As shown in Figure 7.6 (e and f), the magnetization precessional states change in

certain patterns with features of precessing domain walls and vorticies. Figures 7.6 and 7.7 are shown for $J_{ex} = -0.4\,\mathrm{erg/cm^2}$, which is a practical value for Ru [126]. For a greater $J_{ex} = -0.8\,\mathrm{erg/cm^2}$, which can be achieved with, e.g., Ir [127], the behavior is qualitatively similar but the range of J with uniform precession is broader and the precessional frequency is greater.

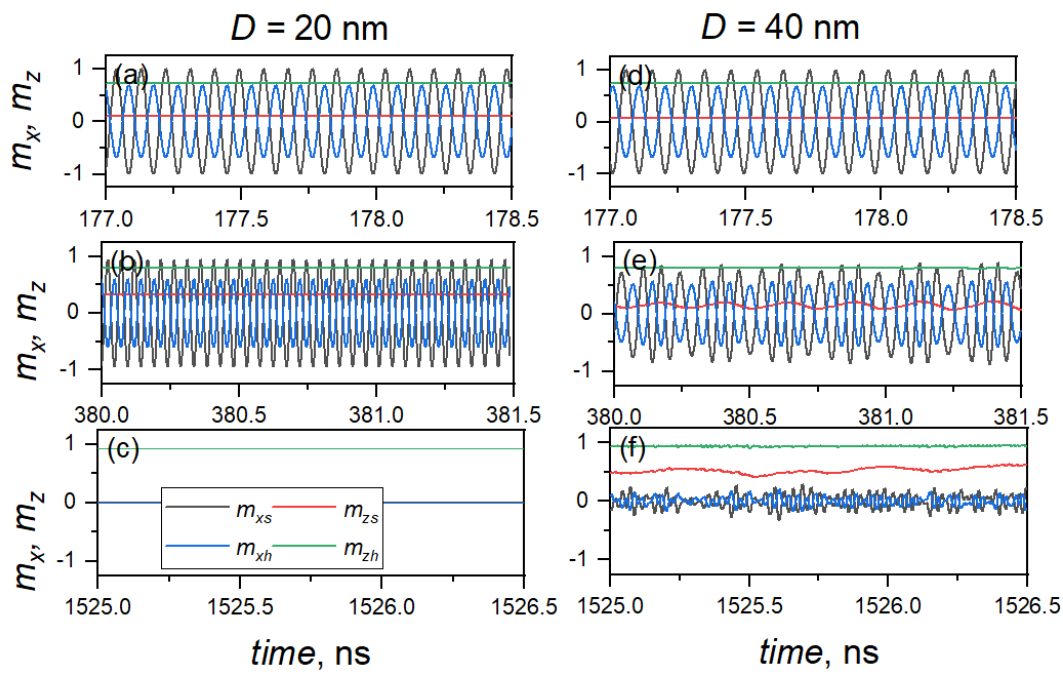

Figure 7.7: Time dependence of the normalized magnetization components m_x and m_z vs. J in SL and HL for $J_{ex} = -0.4\,\mathrm{erg/cm^2}$ for $D = 20\,\mathrm{nm}$ and $40\,\mathrm{nm}$. For (a) and (d) $J = 0.025\,\mu\mathrm{A/nm^2}$, for (b) and (e) $J = 0.057\,\mu\mathrm{A/nm^2}$, and for (c), (f) $J = 0.25\,\mu\mathrm{A/nm^2}$.

Figure 7.7 shows the averaged m_x and m_z in the SL and HL for $D = 20\,\mathrm{nm}$ and $40\,\mathrm{nm}$ for different values of J. At the smallest shown J (Figures 7.6 (a) and (d)), the behavior of m_x and m_z for $D = 20\,\mathrm{nm}$ and $40\,\mathrm{nm}$ is nearly the same: the precession is uniform with mostly in-plane precession in the SL and smaller amplitude precession in the HL, which corresponds to mostly uniform profiles in Figures 7.6 (a) and (d). At a greater J

and $D = 20\,\text{nm}$, the SL still has a uniform precession with a higher frequency (Figure 7.7 (b)), whereas for $D = 40\,\text{nm}$ the precession becomes partially non-uniform with a lower frequency (Figure 7.7 (e)). At the highest J, for $D = 20\,\text{nm}$ the SL does not precess (Figure 7.7 (c)), which corresponds to the vortex state as shown in Figure 7.6 (c). At the same highest J, for $D = 40\,\text{nm}$ the HL has a highly non-uniform precession (Figure 7.7 (f)), which corresponds to the spatial magnetization profile of Figure 7.6 (f).

7.3.2 Operation at room temperature

Characterizing thermal noise is important for understanding the operation of STOs finite temperatures. Here, we show results of the micromagnetic analysis of the AF-ECC STO at room temperature $T = 300\text{K}$. The micromagnetic simulation were performed with the FastMag simulator that included stochastic effects [29,129].

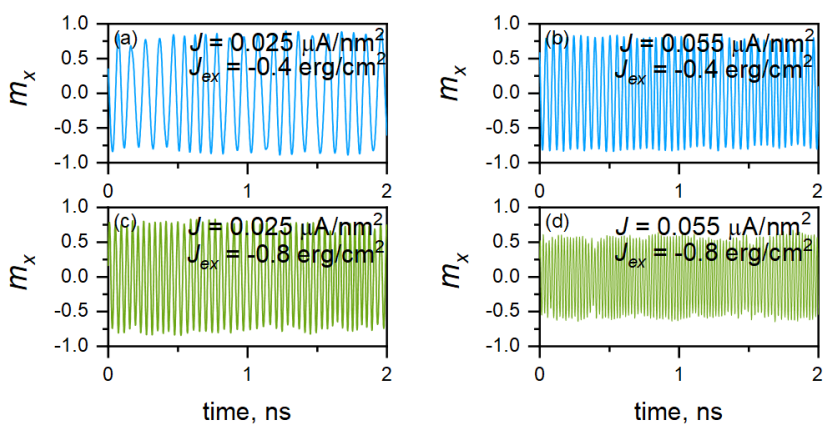

Figure 7.8: Magnetization component m_z vs time at room temperature for different J and J_{ex}.

Figure 7.8 shows the magnetization dynamics in the FL for different J and J_{ex}. The time dependence shows precession as at zero temperature but the precessional

amplitude and frequency have some random variations. Figure 7.9 shows the Fourier spectrum corresponding to the time dynamics results in Figure 7.9. The spectrum has a maximum at the frequency corresponding to the zero-temperature frequency. The linewidth depends on the particular choice of the structure parameters. Generally, we find that higher J and J_{ex}, which correspond to higher precessional frequencies lead to a narrower linewidth. This behavior is important as one of the important benefits of the AF-ECC STO is its high-frequency operation.

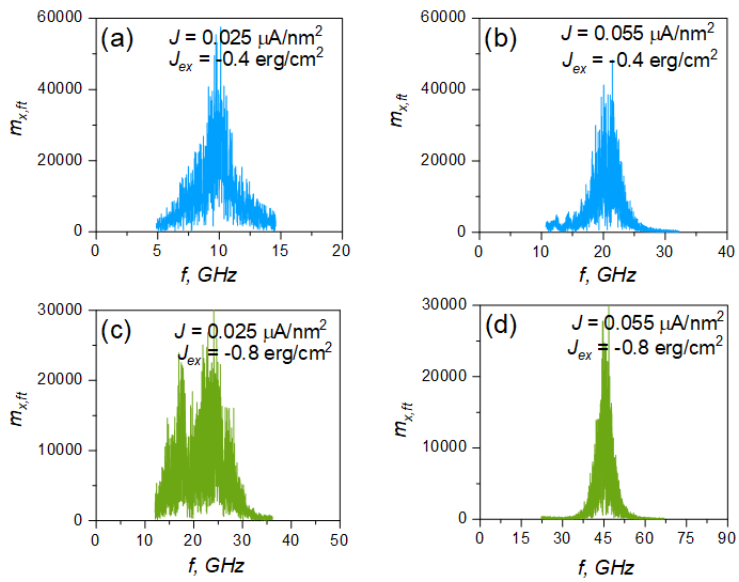

Figure 7.9: Fourier spectrum of m_x for the operation at room temperature for different J and J_{ex} for the AF-ECC STO.

We then compare the room temperature operation of the AF-ECC STO with the operation of other STO types, including an easy-plane single-FL STO, which is chosen as it can operate without an applied field [88], and an easy-axis STO with an applied field, which is chosen as it was the original concept for an STO [85,87,99,100]. Both STOs chosen for comparison operate only at lower frequency ranges that those typical of the AF-

ECC STO and, therefore, the comparisons are done at the lower frequency range.

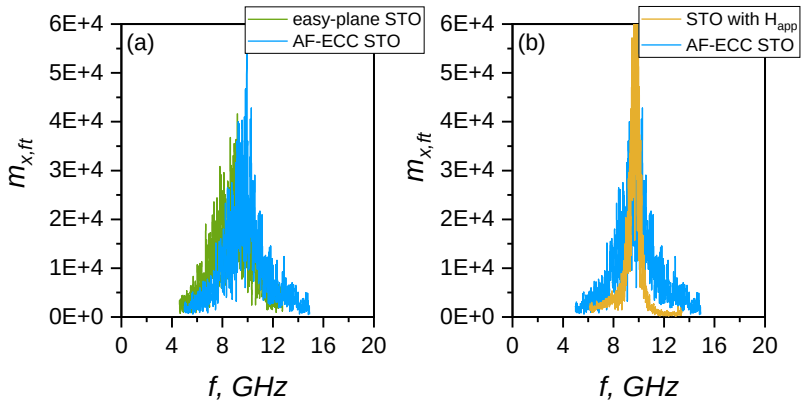

Figure 7.10: Fourier spectrum of m_x for the operation at room temperature of an AF-ECC STO with $J_{ex} = -0.4\,\text{erg}/\text{cm}^2$ and $J = 0.04\,\mu\text{A}/\text{nm}^2$ compared to (a) easy-plane single-FL STO with the following parameters: thickness $t = 0.8\,\text{nm}$, $M_s = 1350\,\text{emu}/\text{cm}^3$, $K_u = 1.11\,\text{Merg}/\text{cm}^3$, $J = 0.04\,\mu\text{A}/\text{nm}^2$, $\alpha = 0.008$; (b) easy-axis STO with an applied field with the following parameters: $t = 3.0\,\text{nm}$, $M_s = 1350\,\text{emu}/\text{cm}^3$, $\alpha = 0.008$, $J = 0.01\,\mu\text{A}/\text{nm}^2$ and $H_{app} = 0.4\,\text{T}$. For all cases $D = 40\,\text{nm}$.

Figures 7.10 (a) and (b) compare the frequency spectrum of AF-ECC STO with those of the easy-plane single-FL STO and easy-axis STO with an applied field, respectively. The structure parameters of the STOs are chosen such that they operate at the same frequency at zero-temperature. We find that the linewidth of the easy-plane single-FL STO is about the same as that of the AF-ECC STO (Figure 7.10(a)). On the other hand, the linewidth of the easy-axis STO with an applied field is narrower (Figure 7.10 (b)). We attribute the reduced linewidth in the latter case to the fact that the precessional frequency is largely given by the applied field that is temperature and thermal noise independent. On the other hand, for the AF-ECC STO and easy-plane single-FL STO, the precessional frequency is determined by the anisotropy and exchange interactions. These interactions are

affected by the thermal noise because they are related to the instantaneous magnetization states, which are a part of the stochastic magnetization dynamics. We note that the linewidth can be reduced by synchronizing multiple STOs or synchronizing the STOs to an AC current or external field [101-103]. In summary, this chapter discussed an AF-ECC STO, which has its FL composed of AF coupled SL and HL. The easy-plane anisotropy of the SL allows the operation at realistic AF coupling strengths producing large precession angles, which is important for generating a large signal.

We developed an analytical model based on a two-spin approximation and further used micromagnetics to study size effects. The precessional frequency can be tuned in a broad frequency range. The operation of the STO can be understood from an interplay between the exchange and anisotropy interactions. The magnetizations in the SL and HL have an azimuthal angular shift, which plays an important role in setting the precessional angle and frequency. The micromagnetic study shows that for smaller currents the operation is close to that predicted by the two-spin model, whereas for greater currents the precessional motion becomes non-uniform.

We investigated the operation of the AF-ECC STO at zero-temperature as well as at room temperature, which includes stochastic thermal noise effects. The linewidth of the Fourier spectrum of the magnetization is higher for greater current densities and AF exchange energy densities, which correspond to higher operational frequencies. The linewidth of the AF-ECC STO is greater than that of an easy-axis STO with an applied field and similar to an easy-plane single-FL STO. AF-ECC STO can be used to generate tunable high-frequency electric signals or to generate an oscillating magnetic field for applications such as microwave assisted magnetic recording. In the latter case, there is no need in the RL

layers. A microwave field can be generated because the precession magnetization magnitude in the SL can be greater than that in the HL.

Acknowledgement

Chapter 7, in part, is a reprint of material as appeared in I. Volvach, A. D. Kent, E. E. Fullerton, and V. Lomakin, “Spin-transfer torque oscillator with an antiferromagnetic exchange coupled composite free layer”. Submitted to Physical Review Applied and currently is under review. This work was supported as part of the Quantum-Materials for Energy Efficient Neuromorphic-Computing (Q-MEEN-C), an Energy Frontier Research Center funded by the U.S. Department of Energy, Office of Science, Basic Energy Sciences under Award #DE-SC0019273 and Extreme Science and Engineering Discovery Environment (XSEDE) supported by NSF Grant #ACI-1548562. The dissertation author was the primary investigator and author of this material.

Chapter 8

Conclusions

In conclusion, this dissertation explored different areas related to spin-currents-powered perpendicular magnetic tunnel junction (p-MTJ) based devices such as magnetoresistive random access memory (MRAM) and spin-torque oscillators (STOs). For the p-MTJ-based memory devices we were mainly looking at ways to tune their behavior under an applied current and ways to improve their thermal stability, current-induced switching and efficiency properties. Our findings on p-MTJ's memory application will help to approach the key requirements of the p-MTJ's free layer, such as high thermal stability and low damping. This will potentially make STT-MRAM an alternative, high-density, high-speed, non-volatile random-access memory to conventional MRAM.

This work also includes a separate study of antiferromagnetically exchange coupled composite (soft/hard) spin torque oscillator (AF-ECC STO) which combines the properties of previously developed and known types of STOs. For the AF-ECC STO we demonstrated its operation via an analytical model and micromagnetic analysis. The operation mechanism

is based on the exchange field due to the antiferromagnetic coupling between soft and hard sub-layers of the free layer as well as on the easy-plane anisotropy of the soft sub-layer. AF-ECC STO can generate large amplitude magnetization oscillations, which can be tuned over a broad frequency range with precessions mostly generated by the soft layer. We also demonstrated that AF-ECC STO offers a flexibility in current control of the oscillation frequency and magnetization angle for realistic material parameters. Our findings on AF-ECC STO can be used in microwave assisted magnetic recording (MAMR) technology.

Bibliography

[1] W. F. Brown, *Micromagnetics* (Krieger Pub Co, 1978).

[2] T. L. Gilbert, *A phenomenological theory of damping in ferromagnetic materials*, IEEE Trans. Magn. 40, 6 (2004).

[3] M. D. Stiles and J. Miltat, *Spin-transfer torque and dynamics*, Spin Dynamics in Confined Magnetic Structures Iii 101 (2006).

[4] L. Landau and E. Lifshits, *On the Theory of the Dispersion of Magnetic Permeability in Ferromagnetic Bodies*, Ukrainian Journal of Physics 53 (2008).

[5] J. Xiao, A. Zangwill, and M. D. Stiles, *Macrospin models of spin transfer dynamics*, Phys. Rev. B 72, 1 (2005).

[6] S. Zhang, P. M. Levy, and A. Fert, *Mechanisms of spin-polarized current-driven magnetization switching*, Physical Review Letters 88, 23 (2002).

[7] J. E. M. a. M. J. Donahue, *Handbook of Magnetism and Advanced Magnetic Materials* (John Wiley & Sons, Ltd., 2007), Vol. volume Micromagnetism.

[8] T. L. Chow, *Introduction to electromagnetic theory : a modern perspective* (Jones & Bartlett Learning, 2006), Illustrated edn.

[9] R. Moskowitz and E. D. Torre, *Theoretical Aspects of Demagnetization Tensors*, IEEE Trans. Magn. Mag2, 4 (1966).

[10] G. M. Wysin, *Magnetic Excitations and Geometric Confinement: Theory and Simulations*, Magnetic Excitations and Geometric Confinement: Theory and Simulations (2015).

[11] M. Kuteifan, Micromagnetic modeling of spintronic devices for memory and recording applications, Ph. D. Thesis UCSD, 2018.

[12] M. D'Aquino, Nonlinear Magnetization Dynamics in Thin-films and Nanoparticles. Ph.D. thesis, 2004.

[13] M. A. Ruderman and C. Kittel, *Indirect Exchange Coupling of Nuclear Magnetic Moments by Conduction Electrons*, Physical Review 96, 1 (1954).

[14] S. S. P. Parkin, N. More, and K. P. Roche, *Oscillations in Exchange Coupling and Magnetoresistance in Metallic Superlattice Structures - Co/Ru, Co/Cr, and Fe/Cr*, Physical Review Letters 64, 19 (1990).

[15] P. Bruno and C. Chappert, *Ruderman-Kittel Theory of Oscillatory Interlayer Exchange Coupling*, Phys. Rev. B 46, 1 (1992).

[16] J. Unguris, R. J. Celotta, and D. T. Pierce, *Observation of 2 Different Oscillation Periods in the Exchange Coupling of Fe/Cr/Fe(100)*, Physical Review Letters 67, 1 (1991).

[17] M. V. Lubarda, Micromagnetic Modeling and Analysis for Memory and Processing Application, Ph.D. Thesis, 2012.

[18] J. C. Slonczewski, *Current-driven excitation of magnetic multilayers*, J. Magn. Magn. Mater. 159, 1-2 (1996).

[19] L. Berger, *Emission of spin waves by a magnetic multilayer traversed by a current*, Phys. Rev. B 54, 13 (1996).

[20] S. Urazhdin, W. L. Lim, and A. Higgins, *Effect of polarizer dynamics on current-induced behaviors in magnetic nanopillars*, Phys. Rev. B 80, 14 (2009).

[21] D. C. Ralph and M. D. Stiles, *Spin transfer torques*, J. Magn. Magn. Mater. 320, 7 (2008).

[22] D. V. Berkov, *Numerical calculation of the energy barrier distribution in disordered many-particle systems: the path integral method*, J. Magn. Magn. Mater. 186, 1-2 (1998).

[23] E. Paz, F. Garcia-Sanchez, and O. Chubykalo-Fesenko, *Numerical evaluation of energy barriers in nano-sized magnetic elements with Lagrange multiplier technique*, Physica B-Condensed Matter 403, 2-3 (2008).

[24] D. Sheppard, R. Terrell, and G. Henkelman, *Optimization methods for finding minimum energy paths*, Journal of Chemical Physics 128, 13 (2008).

[25] G. Henkelman, B. P. Uberuaga, and H. Jonsson, *A climbing image nudged elastic band method for finding saddle points and minimum energy paths*, Journal of Chemical Physics 113, 22 (2000).

[26] P. Maragakis, S. A. Andreev, Y. Brumer, D. R. Reichman, and E. Kaxiras, *Adaptive nudged elastic band approach for transition state calculation*, Journal of Chemical Physics 117, 10 (2002).

[27] R. Dittrich, T. Schrefl, A. Thiaville, J. Miltat, V. Tsiantos, and J. Fidler, *Comparison of Langevin dynamics and direct energy barrier computation*, J. Magn. Magn. Mater. 272 (2004).

[28] D. J. Dunlop, *and O. Ozdemir, Rock Magnetism, Cambridge Studies in Magnetism*, (1997).

[29] D. V. Berkov and N. L. Gorn, *Stochastic dynamic simulations of fast remagnetization processes: recent advances and applications*, J. Magn. Magn. Mater. 290 (2005).

[30] D. A. Garanin, *Fokker-Planck and Landau-Lifshitz-Bloch equations for classical ferromagnets*, Phys. Rev. B 55, 5 (1997).

[31] A. Bachtold, M. Henny, C. Terrier, C. Strunk, C. Schonenberger, J. P. Salvetat, J. M. Bonard, and L. Forro, *Contacting carbon nanotubes selectively with low-ohmic contacts for four-probe electric measurements*, Appl. Phys. Lett. 73, 2 (1998).

[32] X. Hoffer, C. Klinke, J. M. Bonard, L. Gravier, and J. E. Wegrowe, *Spin-dependent magnetoresistance in multiwall carbon nanotubes*, Europhysics Letters 67, 1 (2004).

[33] Y. Oshima, T. Takenobu, K. Yanagi, Y. Miyata, H. Kataura, K. Hata, Y. Iwasa, and H. Nojiri, *Intrinsic Magnetoresistance of Single-Walled Carbon Nanotubes Probed by a Noncontact Method*, Physical Review Letters 104, 1 (2010).

[34] A. Fert, *Nobel Lecture: Origin, development, and future of spintronics*, Reviews of Modern Physics 80, 4 (2008).

[35] G. Binasch, P. Grunberg, F. Saurenbach, and W. Zinn, *Enhanced Magnetoresistance in Layered Magnetic-Structures with Antiferromagnetic Interlayer Exchange*, Phys. Rev. B 39, 7 (1989).

[36] A. H. Bobeck, R. F. Fischer, A. J. Perneski, J. P. Remeika, and Vanuiter.Lg, *Application of Orthoferrites to Domain-Wall Devices*, IEEE Trans. Magn. Mag5, 3 (1969).

[37] R. Suzuki, *Recent Development in Magnetic-Bubble Memory*, Proceedings of the Ieee 74, 11 (1986).

[38] G. Baumgartner, M. Carrard, L. Zuppiroli, W. Bacsa, W. A. deHeer, and L. Forro, *Hall effect and magnetoresistance of carbon nanotube films*, Phys. Rev. B 55, 11 (1997).

[39] X. H. Lou, C. Adelmann, S. A. Crooker, E. S. Garlid, J. Zhang, K. S. M. Reddy, S. D. Flexner, C. J. Palmstrom, and P. A. Crowell, *Electrical detection of spin transport in lateral ferromagnet-semiconductor devices*, Nature Physics 3, 3 (2007).

[40] M. N. Baibich, J. M. Broto, A. Fert, F. N. Vandau, F. Petroff, P. Eitenne, G. Creuzet, A. Friederich, and J. Chazelas, *Giant Magnetoresistance of (001)Fe/(001) Cr Magnetic Superlattices*, Physical Review Letters 61, 21 (1988).

[41] P. Z. a. I. Mertig, *Handbook of Magnetism and Advanced Magnetic Materials, volume Fundamentals and Theory, chapter Enhanced Magnetoresistance. John Wiley & Sons, Ltd.*, (2007).

[42] G. A. Prinz, *Spin-Polarized Transport*, Physics Today 48, 4 (1995).

[43] C. Chappert, A. Fert, and F. N. Van Dau, *The emergence of spin electronics in data storage*, Nature Materials 6, 11 (2007).

[44] S. Tehrani, J. M. Slaughter, M. Deherrera, B. N. Engel, N. D. Rizzo, J. Salter, M. Durlam, R. W. Dave, J. Janesky, B. Butcher, K. Smith, and G. Grynkewich, *Magnetoresistive random access memory using magnetic tunnel junctions*, Proceedings of the Ieee 91, 5 (2003).

[45] M. Julliere, *Tunneling between Ferromagnetic-Films*, Physics Letters A 54, 3 (1975).

[46] A. V. Khvalkovskiy, D. Apalkov, S. Watts, R. Chepulskii, R. S. Beach, A. Ong, X. Tang, A. Driskill-Smith, W. H. Butler, P. B. Visscher, D. Lottis, E. Chen, V. Nikitin, and M. Krounbi, *Basic principles of STT-MRAM cell operation in memory arrays*, J. Phys. D Appl. Phys. 46, 7 (2013).

[47] J. S. Moodera, L. R. Kinder, T. M. Wong, and R. Meservey, *Large Magnetoresistance at Room-Temperature in Ferromagnetic Thin-Film Tunnel-Junctions*, Physical Review Letters 74, 16 (1995).

[48] T. Miyazaki and N. Tezuka, *Giant Magnetic Tunneling Effect in Fe/Al2o3/Fe Junction*, J. Magn. Magn. Mater. 139, 3 (1995).

[49] W. H. Butler, X. G. Zhang, T. C. Schulthess, and J. M. MacLaren, *Spin-dependent tunneling conductance of Fe vertical bar MgO vertical bar Fe sandwiches*, Phys. Rev. B 63, 5 (2001).

[50] J. Mathon and A. Umerski, *Theory of tunneling magnetoresistance of an epitaxial Fe/MgO/Fe(001) junction*, Phys. Rev. B 63, 22 (2001).

[51] M. Bowen, V. Cros, F. Petroff, A. Fert, C. M. Boubeta, J. L. Costa-Kramer, J. V. Anguita, A. Cebollada, F. Briones, J. M. de Teresa, L. Morellon, M. R. Ibarra, F. Guell, F. Peiro, and A. Cornet, *Large magnetoresistance in Fe/MgO/FeCo(001) epitaxial tunnel junctions on GaAs(001)*, Appl. Phys. Lett. 79, 11 (2001).

[52] S. S. P. Parkin, C. Kaiser, A. Panchula, P. M. Rice, B. Hughes, M. Samant, and S. H. Yang, *Giant tunnelling magnetoresistance at room temperature with MgO (100) tunnel barriers*, Nature Materials 3, 12 (2004).

[53] S. Yuasa, A. Fukushima, H. Kubota, Y. Suzuki, and K. Ando, *Giant tunneling magnetoresistance up to 410% at room temperature in fully epitaxial Co/MgO/Co magnetic tunnel junctions with bcc Co(001) electrodes*, Appl. Phys. Lett. 89, 4 (2006).

[54] S. Ikeda, J. Hayakawa, Y. Ashizawa, Y. M. Lee, K. Miura, H. Hasegawa, M. Tsunoda, F. Matsukura, and H. Ohno, *Tunnel magnetoresistance of 604% at 300 K by suppression of Ta diffusion in CoFeB/MgO/CoFeB pseudo-spin-valves annealed at high temperature*, Appl. Phys. Lett. 93, 8 (2008).

[55] R. Sbiaa, H. Meng, and S. N. Piramanayagam, *Materials with perpendicular magnetic anisotropy for magnetic random access memory*, Physica Status Solidi-Rapid Research Letters 5, 12 (2011).

[56] A. D. Kent and D. C. Worledge, *A new spin on magnetic memories*, Nature Nanotechnology 10, 3 (2015).

[57] S. Ikeda, K. Miura, H. Yamamoto, K. Mizunuma, H. D. Gan, M. Endo, S. Kanai, J. Hayakawa, F. Matsukura, and H. Ohno, *A perpendicular-anisotropy CoFeB-MgO magnetic tunnel junction*, Nature Materials 9, 9 (2010).

[58] R. Sbiaa, S. Y. H. Lua, R. Law, H. Meng, R. Lye, and H. K. Tan, *Reduction of switching current by spin transfer torque effect in perpendicular anisotropy magnetoresistive devices (invited)*, J. Appl. Phys. 109, 7 (2011).

[59] D. Apalkov, S. Watts, A. Driskill-Smith, E. Chen, Z. T. Diao, and V. Nikitin, *Comparison of Scaling of In-Plane and Perpendicular Spin Transfer Switching Technologies by Micromagnetic Simulation*, IEEE Trans. Magn. 46, 6 (2010).

[60] I. Volvach, J. G. Alzate, Y. J. Chen, A. J. Smith, D. L. Kencke, and V. Lomakin, *Thermal stability and magnetization switching in perpendicular magnetic tunnel junctions*, Appl. Phys. Lett. 116, 19 (2020).

[61] S. Mangin, D. Ravelosona, J. A. Katine, M. J. Carey, B. D. Terris, and E. E. Fullerton, *Current-induced magnetization reversal in nanopillars with perpendicular anisotropy*, Nature Materials 5, 3 (2006).

[62] A. V. Khvalkovskiy, D. Apalkov, S. Watts, R. Chepulskii, R. S. Beach, A. Ong, X. Tang, A. Driskill-Smith, W. H. Butler, P. B. Visscher, D. Lottis, E. Chen, V. Nikitin, and M. Krounbi, *Basic principles of STT-MRAM cell operation in memory arrays (vol 46, 074001, 2013)*, J. Phys. D Appl. Phys. 46, 13 (2013).

[63] D. Bedau, H. Liu, J. Z. Sun, J. A. Katine, E. E. Fullerton, S. Mangin, and A. D. Kent, *Spin-transfer pulse switching: From the dynamic to the thermally activated regime*, Appl. Phys. Lett. 97, 26 (2010).

[64] D. Bedau, H. Liu, J. J. Bouzaglou, A. D. Kent, J. Z. Sun, J. A. Katine, E. E. Fullerton, and S. Mangin, *Ultrafast spin-transfer switching in spin valve nanopillars with perpendicular anisotropy*, Appl. Phys. Lett. 96, 2 (2010).

[65] S. Bhatti, R. Sbiaa, A. Hirohata, H. Ohno, S. Fukami, and S. N. Piramanayagam, *Spintronics based random access memory: a review*, Materials Today 20, 9 (2017).

[66] D. Apalkov, B. Dieny, and J. M. Slaughter, *Magnetoresistive Random Access Memory*, Proceedings of the Ieee 104, 10 (2016).

[67] C. Song, R. Q. Zhang, L. Y. Liao, Y. J. Zhou, X. F. Zhou, R. Y. Chen, Y. F. You, X. Z. Chen, and F. Pan, *Spin-orbit torques: Materials, mechanisms, performances, and potential applications*, Progress in Materials Science 118 (2021).

[68] M. I. Dyakonov and V. I. Perel, *Possibility of Orienting Electron Spins with Current*, Jetp Letters-Ussr 13, 11 (1971).

[69] M. I. Dyakonov and V. I. Perel, *Current-Induced Spin Orientation of Electrons in Semiconductors*, Physics Letters A A 35, 6 (1971).

[70] E. I. Rashba, *Spin-orbit coupling goes global*, Journal of Physics-Condensed Matter 28, 42 (2016).

[71] E. I. Rashba, *Quantum nanostructures in strongly spin-orbit coupled two-dimensional systems*, Phys. Rev. B 86, 12 (2012).

[72] A. Slavin and V. Tiberkevich, *Nonlinear Auto-Oscillator Theory of Microwave Generation by Spin-Polarized Current*, IEEE Trans. Magn. 45, 4 (2009).

[73] V. Puliafito, R. Khymyn, M. Carpentieri, B. Azzerboni, V. Tiberkevich, A. Slavin, and G. Finocchio, *Micromagnetic modeling of terahertz oscillations in an antiferromagnetic material driven by the spin Hall effect*, Phys. Rev. B 99, 2 (2019).

[74] S. I. Kiselev, J. C. Sankey, I. N. Krivorotov, N. C. Emley, R. J. Schoelkopf, R. A. Buhrman, and D. C. Ralph, *Microwave oscillations of a nanomagnet driven by a spin-polarized current*, Nature 425, 6956 (2003).

[75] S. I. Kiselev, J. C. Sankey, I. N. Krivorotov, N. C. Emley, M. Rinkoski, C. Perez, R. A. Buhrman, and D. C. Ralph, *Current-induced nanomagnet dynamics for magnetic fields perpendicular to the sample plane*, Physical Review Letters 93, 3 (2004).

[76] S. I. Kiselev, J. C. Sankey, I. N. Krivorotov, N. C. Emley, A. G. F. Garcia, R. A. Buhrman, and D. C. Ralph, *Spin-transfer excitations of permalloy nanopillars for large applied currents*, Phys. Rev. B 72, 6 (2005).

[77] J. Torrejon, M. Riou, F. A. Araujo, S. Tsunegi, G. Khalsa, D. Querlioz, P. Bortolotti, V. Cros, K. Yakushiji, A. Fukushima, H. Kubota, S. Y. Uasa, M. D. Stiles, and J. Grollier, *Neuromorphic computing with nanoscale spintronic oscillators*, Nature 547, 7664 (2017).

[78] J. Grollier, D. Querlioz, and M. D. Stiles, *Spintronic Nanodevices for Bioinspired Computing*, Proceedings of the Ieee 104, 10 (2016).

[79] J. A. Katine and E. E. Fullerton, *Device implications of spin-transfer torques*, J. Magn. Magn. Mater. 320, 7 (2008).

[80] L. N. Volvach, A. E. Volvach, M. G. Larionov, G. C. MacLeod, P. Wolak, B. Kramer, K. M. Menten, A. Kraus, J. Brand, A. Zanichelli, S. Poppi, and S. Righini, *Flaring water masers associated with W49N*, Astronomy & Astrophysics 628 (2019).

[81] S. Kaka, M. R. Pufall, W. H. Rippard, T. J. Silva, S. E. Russek, and J. A. Katine, *Mutual phase-locking of microwave spin torque nano-oscillators*, Nature 437, 7057 (2005).

[82] F. B. Mancoff, N. D. Rizzo, B. N. Engel, and S. Tehrani, *Phase-locking in double-point-contact spin-transfer devices*, Nature 437, 7057 (2005).

[83] M. Tsoi, A. G. M. Jansen, J. Bass, W. C. Chiang, V. Tsoi, and P. Wyder, *Generation and detection of phase-coherent current-driven magnons in magnetic multilayers*, Nature 406, 6791 (2000).

[84] W. H. Rippard, M. R. Pufall, S. Kaka, T. J. Silva, S. E. Russek, and J. A. Katine, *Injection locking and phase control of spin transfer nano-oscillators*, Physical Review Letters 95, 6 (2005).

[85] Z. M. Zeng, G. Finocchio, and H. W. Jiang, *Spin transfer nano-oscillators*, Nanoscale 5, 6 (2013).

[86] C. X. Zheng, H. H. Chen, X. L. Zhang, Z. Z. Zhang, and Y. W. Liu, *Spin torque nano-oscillators with a perpendicular spin polarizer*, Chinese Physics B 28, 3 (2019).

[87] I. Firastrau, L. D. Buda-Prejbeanu, B. Dieny, and U. Ebels, *Spin-torque nano-oscillator based on a synthetic antiferromagnet free layer and perpendicular to plane polarizer*, J. Appl. Phys. 113, 11 (2013).

[88] D. Houssameddine, U. Ebels, B. Delaet, B. Rodmacq, I. Firastrau, F. Ponthenier, M. Brunet, C. Thirion, J. P. Michel, L. Prejbeanu-Buda, M. C. Cyrille, O. Redon, and B. Dieny, *Spin-torque oscillator using a perpendicular polarizer and a planar free layer*, Nature Materials 6, 6 (2007).

[89] R. Khymyn, I. Lisenkov, V. S. Tiberkevich, A. N. Slavin, and B. A. Ivanov, *Transformation of spin current by antiferromagnetic insulators*, Phys. Rev. B 93, 22 (2016).

[90] R. Khymyn, I. Lisenkov, V. Tiberkevich, B. A. Ivanov, and A. Slavin, *Antiferromagnetic THz-frequency Josephson-like Oscillator Driven by Spin Current*, Scientific Reports 7 (2017).

[91] C. Safranski and J. Z. Sun, *Interface moment dynamics and its contribution to spin-transfer torque switching process in magnetic tunnel junctions*, Phys. Rev. B 100, 1 (2019).

[92] H. Zhong, S. Z. Qiao, S. S. Yan, L. J. Liang, Y. R. Zhao, and S. S. Kang, *Terahertz spin-transfer torque oscillator based on a synthetic antiferromagnet*, J. Magn. Magn. Mater. 497 (2020).

[93] D. Houssameddine, J. F. Sierra, D. Gusakova, B. Delaet, U. Ebels, L. D. Buda-Prejbeanu, M. C. Cyrille, B. Dieny, B. Ocker, J. Langer, and W. Maas, *Spin torque driven excitations in a synthetic antiferromagnet*, Appl. Phys. Lett. 96, 7 (2010).

[94] Z. M. Zeng, P. K. Amiri, I. N. Krivorotov, H. Zhao, G. Finocchio, J. P. Wang, J. A. Katine, Y. M. Huai, J. Langer, K. Galatsis, K. L. Wang, and H. W. Jiang, *High-Power Coherent Microwave Emission from Magnetic Tunnel Junction Nano-oscillators with Perpendicular Anisotropy*, Acs Nano 6, 7 (2012).

[95] A. D. Kent, B. Ozyilmaz, and E. del Barco, *Spin-transfer-induced precessional magnetization reversal*, Appl. Phys. Lett. 84, 19 (2004).

[96] P. Guo, J. F. Feng, H. X. Wei, X. F. Han, B. Fang, B. S. Zhang, and Z. M. Zeng, *Temperature dependence of microwave oscillations in magnetic tunnel junctions with a perpendicularly magnetized free layer*, Appl. Phys. Lett. 106, 1 (2015).

[97] Z. M. Zeng, G. Finocchio, B. S. Zhang, P. K. Amiri, J. A. Katine, I. N. Krivorotov, Y. M. Huai, J. Langer, B. Azzerboni, K. L. Wang, and H. W. Jiang, *Ultralow-current-density and bias-field-free spin-transfer nano-oscillator*, Scientific Reports 3 (2013).

[98] U. Ebels, D. Houssameddine, I. Firastrau, D. Gusakova, C. Thirion, B. Dieny, and L. D. Buda-Prejbeanu, *Macrospin description of the perpendicular polarizer-planar free-layer spin-torque oscillator*, Phys. Rev. B 78, 2 (2008).

[99] M. d'Aquino, C. Serpico, G. Bertotti, R. Bonin, and I. D. Mayergoyz, *Analysis of thermally induced magnetization dynamics in spin-transfer nano-oscillators*, Physica B-Condensed Matter 407, 9 (2012).

[100] R. Sato, Y. Saito, and K. Mizushima, *Current-dependent linewidth of a spin-transfer nano-oscillator*, J. Magn. Magn. Mater. 321, 8 (2009).

[101] M. d'Aquino, C. Serpico, R. Bonin, G. Bertotti, and I. D. Mayergoyz, *Analysis of synchronized regimes for injection-locked spin-transfer nano-oscillators*, Physica B-Condensed Matter 407, 9 (2012).

[102] M. d'Aquino, C. Serpico, R. Bonin, G. Bertotti, and I. D. Mayergoyz, *Micromagnetic study of phase-locking in spin-transfer nano-oscillators driven by currents and ac fields*, J. Appl. Phys. 109, 7 (2011).

[103] K. N. Aleshin, V. V. Matrosov, and K. G. Mishagin, *Synchronization of Spin-Transfer Nano-Oscillator by an External Source*, Technical Physics Letters 43, 3 (2017).

[104] L. Ozyuzer, A. E. Koshelev, C. Kurter, N. Gopalsami, Q. Li, M. Tachiki, K. Kadowaki, T. Yamamoto, H. Minami, H. Yamaguchi, T. Tachiki, K. E. Gray, W. K. Kwok, and U. Welp, *Emission of coherent THz radiation from superconductors*, Science 318, 5854 (2007).

[105] H. V. Gomonay and V. M. Loktev, *Spin transfer and current-induced switching in antiferromagnets*, Phys. Rev. B 81, 14 (2010).

[106] O. R. Sulymenko, O. V. Prokopenko, V. S. Tiberkevich, A. N. Slavin, B. A. Ivanov, and R. S. Khymyn, *Terahertz-Frequency Spin Hall Auto-oscillator Based on a Canted Antiferromagnet*, Physical Review Applied 8, 6 (2017).

[107] L. Thomas, G. Jan, S. Le, S. Serrano-Guisan, Y. J. Lee, H. L. Liu, J. Zhu, J. Iwata-Harms, R. Y. Tong, S. Patel, V. Sundar, D. N. Shen, Y. Yang, R. R. He, J. Haq, Z. J. Teng, V. Lam, P. Liu, Y. J. Wang, T. Zhong, and P. K. Wang, *Probing magnetic properties of STT-MRAM devices down to sub-20 nm using Spin-Torque FMR*, 2017 Ieee International Electron Devices Meeting (Iedm) (2017).

[108] H. Sato, E. C. I. Enobio, M. Yamanouchi, S. Ikeda, S. Fukami, S. Kanai, F. Matsukura, and H. Ohno, *Properties of magnetic tunnel junctions with a MgO/CoFeB/Ta/CoFeB/MgO recording structure down to junction diameter of 11 nm*, Appl. Phys. Lett. 105, 6 (2014).

[109] T. Devolder, A. Le Goff, and V. Nikitin, *Size dependence of nanosecond-scale spin-torque switching in perpendicularly magnetized tunnel junctions*, Phys. Rev. B 93, 22 (2016).

[110] G. Jan, L. Thomas, S. Le, Y. J. Lee, H. L. Liu, J. Zhu, J. Iwata-Harms, S. Patel, R. Y. Tong, S. Serrano-Guisan, D. N. Shen, R. R. He, J. Haq, J. Teng, V. Lam, R. Annapragada, Y. J. Wang, T. Zhong, T. Torng, and P. K. Wang, *Achieving Sub-ns switching of STT-MRAM for future embedded LLC applications through improvement of nucleation and propagation switching mechanisms*, 2016 Ieee Symposium on Vlsi Technology (2016).

[111] M. Lavanant, P. Vallobra, S. P. Watelot, V. Lomakin, A. D. Kent, J. Sun, and S. Mangin, *Asymmetric Magnetization Switching in Perpendicular Magnetic Tunnel Junctions: Role of the Synthetic Antiferromagnet's Fringe Field*, Physical Review Applied 11, 3 (2019).

[112] L. Thomas, G. Jan, S. Le, Y. J. Lee, H. L. Liu, J. Zhu, S. Serrano-Guisan, R. Y. Tong, K. Y. Pi, D. N. Shen, R. R. He, J. Haq, Z. J. Teng, R. Annapragada, V. Lam, Y. J. Wang, T. Zhong, T. Torng, and P. K. Wang, *Solving the Paradox of the Inconsistent Size Dependence of Thermal Stability at Device and Chip-level in Perpendicular STT-MRAM*, 2015 Ieee International Electron Devices Meeting (Iedm) (2015).

[113] R. Chang, S. Li, M. V. Lubarda, B. Livshitz, and V. Lomakin, *FastMag: Fast micromagnetic simulator for complex magnetic structures (invited) (vol 109, 07D358, 2011)*, J. Appl. Phys. 110, 3 (2011).

[114] R. Dittrich, A. Thiaville, J. Miltat, and T. Schrefl, *Rigorous micromagnetic computation of configurational anisotropy energies in nanoelements*, J. Appl. Phys. 93, 10 (2003).

[115] G. D. Chaves-O'Flynn, G. Wolf, D. Pinna, and A. D. Kent, *Micromagnetic study of spin transfer switching with a spin polarization tilted out of the free layer plane*, J. Appl. Phys. 117, 17 (2015).

[116] P. Bouquin, S. Rao, G. S. Kar, and T. Devolder, *Size dependence of spin-torque switching in perpendicular magnetic tunnel junctions*, Appl. Phys. Lett. 113, 22 (2018).

[117] K. Tsunoda, M. Aoki, H. Noshiro, Y. Iba, S. Fukuda, C. Yoshida, Y. Yamazaki, A. Takahashi, A. Hatada, M. Nakabayashi, Y. Tsuzaki, and T. Sugii, *Area Dependence of Thermal Stability Factor in Perpendicular STT-MRAM Analyzed by Bi-directional Data Flipping Model*, 2014 Ieee International Electron Devices Meeting (Iedm) (2014).

[118] J. Z. Sun, S. L. Brown, W. Chen, E. A. Delenia, M. C. Gaidis, J. Harms, G. Hu, X. Jiang, R. Kilaru, W. Kula, G. Lauer, L. Q. Liu, S. Murthy, J. Nowak, E. J. O'Sullivan, S. S. P. Parkin, R. P. Robertazzi, P. M. Rice, G. Sandhu, T. Topuria, and D. C. Worledge, *Spin-torque switching efficiency in CoFeB-MgO based tunnel junctions*, Phys. Rev. B 88, 10 (2013).

[119] I. Yulaev, M. V. Lubarda, S. Mangin, V. Lomakin, and E. E. Fullerton, *Spin-transfer-torque reversal in perpendicular anisotropy spin valves with composite free layers*, Appl. Phys. Lett. 99, 13 (2011).

[120] R. H. Victora and X. Shen, *Exchange coupled composite media for perpendicular magnetic recording*, IEEE Trans. Magn. 41, 10 (2005).

[121] D. Suess, T. Schrefl, S. Fahler, M. Kirschner, G. Hrkac, F. Dorfbauer, and J. Fidler, *Exchange spring media for perpendicular recording*, Appl. Phys. Lett. 87, 1 (2005).

[122] A. Singh, S. Gupta, M. Kuteifan, M. Lubarda, V. Lomakin, and O. Mryasov, *Effect of interlayer exchange coupling parameter on switching time and critical current density in composite free layer*, J. Appl. Phys. 115, 17 (2014).

[123] N. F. Supper, D. T. Margulies, A. Moser, A. Berger, H. Do, and E. E. Fullerton, *Writability enhancement using exchange spring media*, IEEE Trans. Magn. 41, 10 (2005).

[124] G. L. Miller and D. R. Sheehy, *A New Approach to Output-Sensitive Construction of Voronoi Diagrams and Delaunay Triangulations*, Discrete & Computational Geometry 52, 3 (2014).

[125] Y. Tomczak, T. Lin, J. Swerts, S. Couet, S. Mertens, E. L. Liu, W. Kim, K. Sankaran, G. Pourtois, D. Tsvetanova, L. Souriau, S. Van Elshocht, G. S. Kar, and

A. Furnemont, *Influence of the Reference Layer Composition on the Back-End-of-Line Compatibility of Co/Ni-Based Perpendicular Magnetic Tunnel Junction Stacks*, IEEE Trans. Magn. 52, 7 (2016).

[126] L. Fallarino, V. Sluka, B. Kardasz, M. Pinarbasi, A. Berger, and A. D. Kent, *Interlayer exchange coupling between layers with perpendicular and easy-plane magnetic anisotropies*, Appl. Phys. Lett. 109, 8 (2016).

[127] O. Hellwig, A. Berger, J. B. Kortright, and E. E. Fullerton, *Domain structure and magnetization reversal of antiferromagnetically coupled perpendicular anisotropy films*, J. Magn. Magn. Mater. 319, 1-2 (2007).

[128] O. Hellwig, A. Berger, and E. E. Fullerton, *Magnetic phase separation in artificial A-type antiferromagnetic films*, Phys. Rev. B 75, 13 (2007).

[129] D. J. Dunlop, *Magnetism in Rocks*, Journal of Geophysical Research-Solid Earth 100, B2 (1995).